Mobile Neutron Sources for Residual Stress Measurement

by

Michael A. Godin

Submitted to the Department of Nuclear Engineering
in partial fulfillment of the requirements for the degree of

Master of Science in Nuclear Engineering

at the

MASSACHUSETTS INSTITUTE OF TECHNOLOGY

February 1994

Author ....
Department of Nuclear Engineering
February 6, 1994

Certified by ....
Dr. Richard Lanza
Principal Scientist
Thesis Supervisor

Read by ....
Dr. Sow Hsin Chen
Professor of Nuclear Engineering
Thesis Reader

Accepted by ....
Dr. Allan Henery
Chairman, Committee on Graduate Students

Mobile Neutron Sources for Residual Stress Measurement

by

Michael A. Godin

Submitted to the Department of Nuclear Engineering
on February 6, 1994, in partial fulfillment of the
requirements for the degree of
Master of Science in Nuclear Engineering

Abstract

In this thesis, the requirements of a system for determining residual stresses in large objects using neutron diffraction are defined. The mathematics of determining stresses in polycrystalline materials with neutron diffraction are explored, and the process of design modeling and optimization is discussed. Using these optimization routines, a small, accelerator-based system for determining internal stresses is conceptually designed. The system is evaluated to determine how much time is required to make a stress measurement with uncertainty equal to 10% of the yield stress. It is predicted, that by using a polyethelene moderator and a position-sensitive time-of-flight detector, a measurement can be made in 8 hours; using a source with 100 times the intensity, the measurement time drops to 5 minutes.

Thesis Supervisor: Dr. Richard Lanza
Title: Principal Scientist

Acknowledgments

I would like to acknowlege the following people for their support and encouragement:

Dr. Richard Lanza, for adising me on this thesis.

Dr. Sow Hsin Chen, for reading this thesis.

Cloin Robertson, my former boss, for pushing me to attend his alma mater, MIT.

Dr. John Carprnter, for providing an excellent source of information on neutron sources.

Ercle Herbert, my contact at the Department of Energy, for putting up with me.

Vinh Dang, for support and encouragement.

Joe Patton, for support and encouragement.

Michelle Ryder, for especially empathatic support and encouragement.

Ray and Maureen Godin, my parents, thanks for everything.

Contents

List of Figures

List of Tables

Chapter 1

Introduction

In this chapter, the importance of and the measurement of residual stresses in materials is discussed. Methods of measuring residual stresses are presented, and the reasons for using neutron diffraction are given. The process of using neutron diffraction to determine internal stresses is explained briefly. Finally, areas in which this thesis aims to improve the use of neutron diffraction to determine internal stresses are discussed.

1.1 Residual Internal Stresses

Within a material there may be several sources of internal stress at any one time, such as external loads, thermal changes, and residual stresses. Theoretically, the stresses resulting from external loads and thermal changes can often be estimated, if the material in question is well understood and if the external load or temperature change can be measured. However, residual stresses are more difficult to estimate, as they exist independent of external, measurable properties. They are the result of all the processes that have affected the part throughout its existence. If one knew exactly all the processes that a part has gone through, one may be able to estimate the residual stresses theoretically, by evaluating the changes in the material throughout its lifetime, starting with each phase in the manufacturing process[1]. However, such an evaluation would be very approximate; some form of experimental verification becomes necessary.

Processes which induce residual stresses usually deform the material plastically during fabrication. Some examples are: hot and cold rolling; punching and pressing; forging and casting; welding, soldering, and brazing; uniform and non-uniform heat treatments; and surface machining. Over time, passive processes may induce residual stresses through mechanisms such as creep, corrosion, recrystallization, radiation damage, and phase changes.

Since residual stresses in a part are sometimes the unknown quantity leading to the failure of a device, one may consider them to be purely undesirable. However, residual stresses are not always undesirable; they are only undesirable if they act in the same direction as the stresses imparted by external loads; if they act in the opposite direction from external loads, they can actually be helpful.

In some materials, such as reinforced concrete, the residual stress on the concrete due to the rebar in the matrix actually helps to hold the concrete together, resisting failure. Another example is shot-peened surfaces. Shot peening the surface of a metallic part induces highly compressive residual stresses. These compressive surface stresses tend to resist cracking and pitting.

The undesirable aspect of residual stresses arises mainly because they are so difficult to measure. Therefore, they are often left unmeasured. Often, extra bulk must be added to a part because the magnitude and direction of residual stresses are unknown; the part is designed to withstand the highest estimate of combined internal and external stress. If this estimate is too low, the part may fail; in some cases this could lead to great material and human loss. If the estimate of maximum internal stress is too high, extra bulk is designed into the part, increasing not only the mass and cost of the part, but also requiring other parts of the system to accommodate the added weight; increasing their bulk, weight, and cost. The following are the three essential areas in which residual stress measurements become important: the research and design of a part, the manufacture of a part, and the

---

[1] Many examples are given in Noyan and Cohen [29]

long-term evaluation of a part.

1.1.1 Residual Stresses in Research and Design

Research and design, as they apply to the creation of a part or a device, consist of many steps, beginning with the identification of a need, and culminating with the production of the desired part. Residual stress measurements are both useful and important at two stages in the design process; materials research and prototype evaluation.

It is generally well understood how a given heat treatment or surface processing operation will affect a piece of carbon steel. This knowledge has been built up from many years of experience with steel; for example, what makes it break, what makes it tough, what makes it stiff. Today, the technology exists to create new materials with advantageous properties, such as high strength, low weight, or high chemical resistance; but the freedom does not exist to allow these new materials to stand "the test of time," in the way that steel has. Designs using the advantageous properties of new materials must anticipate how the formation of the materials and the degradation of the materials will affect lifelong performance. This information can be acquired if one has a methodology for measuring residual stresses.

In the materials research portion of the design process, an attempt is made to evaluate how various processes can affect the residual stress in a material. A process may be applied to a material; then the residual stress within the material evaluated through experimental techniques, to see how the behavior of the material differs from theoretical expectations. For example, shot peening the surface of a metal creates a compressive stress on the surface of the metal and a tensile stress inside the material. If traditional stress evaluation techniques are used to measure the applied surface stresses, the stress within the material can be determined theoretically. These theoretical values can then be compared to experimental values of internal residual stress. In the case of one material (UD 720 Nickel Superalloy), the theoretical internal stresses vary from the experimental results up to 50% of the magnitude of surface stress [37].

In prototype evaluation, the knowledge gained from materials research is combined with the identified need to create a part. A "first of a kind" part is created, then evaluated experimentally. The stresses in this part could be experimentally inspected to see that residual stresses in the part are equal to their expected values. If they are too high or low (accounting for changes that may occur during the life of the part), the part may need to be redesigned, to avoid failure or overdesign.

1.1.2 Residual Stresses and Manufacture

Once a part is designed, and ready to be produced in quantity, some consideration should be given to inspecting the finished product. One out of every N pieces may be inspected either destructively or non-destructively, to achieve a statistical assurance of product quality. Alternatively, every piece may be inspected non-destructively, to give a more certain assurance of product quality, limited only by the accuracy of the measurement process.

Residual stress measurements can be applied following a manufacturing process such as welding, to determine if there are stress concentrations within the weld. These tend to indicate flaws which can lead to cracks and catastrophic failure. The stress on rebar within a prestressed concrete matrix could be inspected to see that there is adequate prestressing present. Inadequate prestressing could lead to failure in this case. There are many more applications where residual stress measurements could be used advantageously to detect manufacturing flaws.

1.1.3 Residual Stresses and Long term evaluation

After some time in service, one may question the reliability of a part. Residual stresses may have built up due to damaging processes such as creep, corrosion, recrystallization, radiation damage, and/or phase changes. If the residual stress of the part in question can be measured, stress concentrations around flaws may be detected, or the loss of beneficial residual stresses may be determined. For example, airplane fuselages are seeing increasingly longer lifetimes. It is likely that some of these fuselages have internal flaws which will eventually lead to catastrophies. Some of these flaws may be detected through processes such as residual stress measurement[2], thereby avoiding some of these catastrophies.

An example of a system for which residual stress measurements could play an integral part would be a fluid handling system for toxic, radioactive waste. It is critical that failures in such a system be kept to a minimum; these failures can be minimized through a rigorous program of residual stress measurement. The system would most likely employ new materials, resistant to the toxic compounds in the waste stream, and also resistant to radiation damage. Such an advanced material would have to undergo tests, however, so that a better understanding may be gained of its reaction to different manufacturing processes. As parts of the system are designed and fabricated, they should then undergo the similar tests, to see that the materials react as expected to forming processes. Then the system can be inspected during its construction, to determine whether or not it contains manufacturing flaws. Finally, throughout its lifetime, the system will need to be tested, to see that stresses have not changed unacceptably due to radiation damage, corrosion, unexpected loads, unexpected temperature changes, and/or other processes.

1.1.4 Residual Stress Determination Techniques

There are both destructive and non-destructive methods available for determining internal residual stresses. The destructive processes for measuring internal stresses consist either of relieving the stress so that part deformation may be observed; or of making the internal stress an external stress, so that it may then be measured. In the latter r process, the part is usually destroyed. Non-destructive processes, on the other hand, rely on the determination of the internal stresses through external means only.

An example of the former destructive process for measuring residual stress in which internal stress is relieved is hole drilling. Several holes are drilled into a part, and the regions around each hole tend to deform in accordance with the relieved internal stress. Such surface deformations can be measured with either electrical or mechanical strain gauges, or by the fracture of brittle coatings. Unfortunately, the process of hole drilling itself can actually

---

[2] Or small angle neutron scattering (see [7])

impart unwanted internal stresses, therefore complicating results.

An example of the latter destructive process for measuring residual stress in which the internal stress is made an external stress is X-ray diffraction. X-ray diffraction measures average change in microstrain in a given direction. An advantage of X-ray analysis is that it can measure the stress in different phases independently, making it an ideal method for evaluating composites. Although X- ray diffraction is normally a surface-only technique of measuring stress, it can be used inside the volume of a part if the surface is peeled away in successive layers. Of course, this peeling process destroys the part, and may impart or relieve stresses.

An example of a non-destructive technique for measuring residual stress is ultrasound. Ultrasound relies on changes in the speed of sound in a material due to the state of stress in that material. Compressive stresses tend to increase wave velocities, while tensile stresses decrease wave velocities. However, the process works well only in simple geometries with homogeneous materials[29].

Another non-destructive technique relies on analyzing the rotation of magnetic domains within a ferromagnetic material rotate. The material is put within a magnetic field, causing microscopic magnetic domains within the material to rotate parallel to the external field. These rotations can be sensed by a coil of wire around the specimen, connected to an amplifier. Stresses help determine how easily the domains can rotate. Unfortunately, this method is limited to magnetic alloys which are small enough and accessible enough to put inside a coil. Also, the signal saturates at about 500 MPa, limiting its applicability as a measuring technique for large stresses[29].

Neutron diffraction is similar to X-ray diffraction, except that it can resolve stresses within materials at depths of a few centimeters, making it a non-destructive, rather than a destructive technique for measuring internal stresses. Like X-ray diffraction, neutron diffraction can be used to measure the stresses in different phases independently. However, its applicability is greatly reduced by the requirement of a large neutron source such as a reactor or spallation device. These items are inaccessible, too costly, and/or unacceptable in many instances.

1.1.5 Residual Stress Determination Requirements

It is important to note that many of the applications of residual stress determination are located in places such as factories and airports; generally out in the field, far from research institutions. Ideally, the residual stress determination system of choice would be:

1. Portable, so that it can be taken to the measurement site.
2. Maneuverable, so that it can be positioned in tight quarters, allowing for measurements at any location on a large object.
3. Safe, so that it does not endanger the health of its operators.
4. Surface penetrating, so that the stresses anywhere within an object can be determined.
5. Precise enough to resolve small changes in stress.
6. Applicable to many engineering materials.
7. Socially acceptable, so that those who stand to benefit from it will not be afraid of it.
8. Inexpensive if mass-produced.
9. Quick, so that measurements can be made within reasonable timeframes.

Given these nine criteria, neutron diffraction could be the method of choice, if it were not for the reactor or spallation source that is usually required with it. Granted, there are small neutron sources available, but today's portable sources do not have the flux to make diffraction measurements quickly or accurately. This thesis will investigate methods of supplying neutrons to perform residual stress measurements which meet all nine of the above criteria.

1.2 Stress Measurements with Neutron Diffraction

Neutron diffraction was first demonstrated in 1936 by Halban and Preiswerk, using a radium-beryllium source. These early measurements were inspired by the finding that the deBroglie wavelength of thermal neutrons was about 1.8 angstroms, comparable to the spacing of crystal planes in common materials. It was theorized, and later proven that these neutrons would undergo Bragg diffraction, revealing the structure of the scattering medium. However, meaningful measurements were not made with this technique until more powerful neutron sources were available in the mid 1940's.

The technique of using neutron diffraction to determine internal stresses was first developed at Harwell Laboratory in 1981.[31] A simple setup for neutron diffraction is shown in figure 1-1. The sampled volume is defined by the intersection of the two collimators. The desired quantity is the lattice spacing d. Changes in d represent elastic strains, which are due to stresses. In a sampled volume, if the value of d is determined, then the stress in that volume is given by:

$$\sigma = E\epsilon = \frac{E(d - d_0)}{d_0},$$

where σ is the stress normal to the measured planes, ϵ is the strain normal to the measured planes, and d_0 is the lattice spacing in a "stress free" portion of the material, or the average value of d for a given plane.

The fundamental equation involved in the diffraction measurement process is the Bragg equation,

$$n\lambda = 2d\sin(\theta),$$

where λ is the deBroglie wavelength of the scattered neutron, θ is the scattering angle, and n is an integer, usually 1. If one were to count neutrons of a particular wavelength λ scattering at various angles θ, one would find a peak in the number of neutrons at a certain angle. From the above equation, one could then determine the value of d. Alternately, one could select a value of θ, and then find the wavelength which causes the greatest number of neutrons to scatter at that angle. One possibility for determining d is to find the peak value of λ at several angles simultaneously with a position-sensitive detector; this would give several values of d which could be averaged.

The wavelength of a neutron can be determined from its time of flight over a distance, since $\lambda = h/mv$, where h is Planck's constant, m is the neutron mass, and v is the neutron

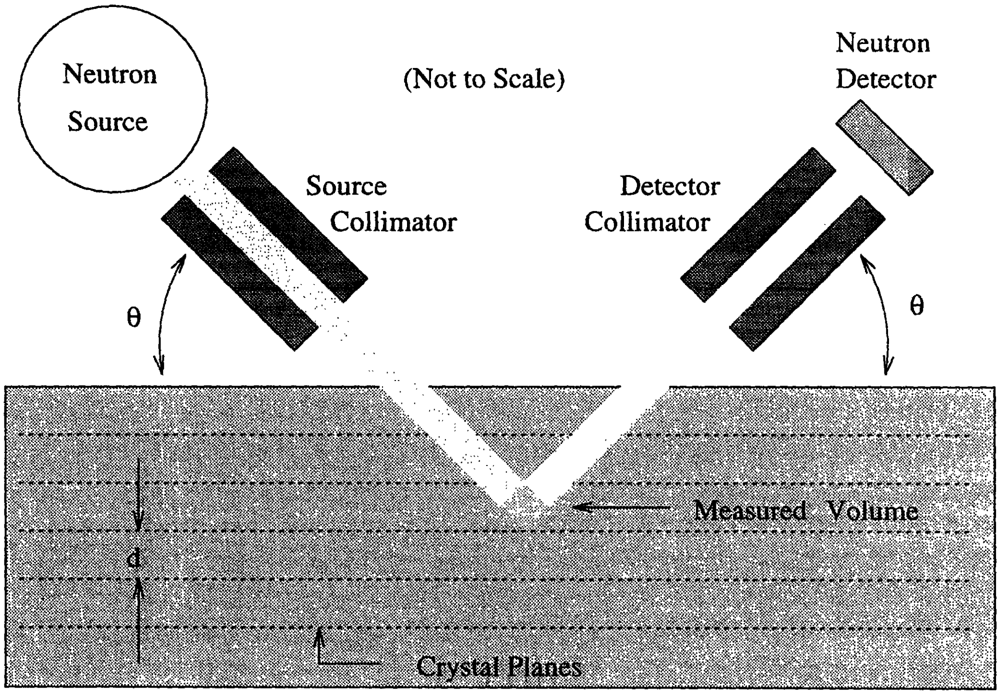

Figure 1-1: Neutron Diffraction

velocity. If the neutron's travel distance is set to a value s, then $\lambda = \mathbf{h}t/ms$, where t is the travel time of the neutron. The equation for d thus becomes:

$$d = \frac{n\mathbf{h}t}{2ms\sin(\theta)}$$

.

1.3 Methodology

A fundamental problem with performing neutron diffraction in the field is that portable neutron sources have relatively low neutron fluxes compared to the large reactors with which the technique was developed. This results in several limitations, including low measurement accuracy, long measurement times, and large measurement volumes. It is the aim of this thesis to optimize the design of a portable neutron source for internal stress measurements so that the aforementioned limitations can be minimized.

The theory and methodology of determining internal stresses with neutron diffraction will be explored first, so that systems which are designed can be properly evaluated. Also, it is intended that an in-depth understanding of the theory will lead to insights into more effective designs.

Neutron sources for neutron diffraction will be evaluated next. This evaluation includes both the development of sources for high-energy neutrons, as well as the development of moderators for making those neutrons usable. Some theoretical discussion will take place, but due to the tight, complicated geometry of a mobile neutron source, many theoretical assumptions do not apply, so most of the discussion will be of results from Monte Carlo simulations. Some methods of neutron production do not seem to have been explored as sources, and are also worthy of investigation; these will be investigated briefly. For example, production of a directional beam may be possible. This could be achieved if the neutrons are produced coherently from a crystal lattice.

Beam handling techniques will then be discussed, concentrating on the theory of collimators, and on the design of shielding. Increased shielding protects workers and lowers experimental noise, but at the cost of reduced neutron intensity for a given volume of sample. The emphasis of the shielding optimization will be to reduce the shield to as small a radius as possible, while still allowing an operator to operate the device at a distance of 3 meters from its surface.

Using the results from the previous chapters, a system will then be conceptually designed to provide optimum resolution for a given measuring volume and period. This section will determine if the neutrons are to be monochromated, or measured by time of flight; determining the optimum parameters in either case. Following this determination, the entire system will be evaluated to see how much time is required to measure stresses with an uncertainty equal to 10% of the yield stress. The intent is to design a system which meets the 9 requirements listed in Section 1.1.5.

The emphasis of this thesis will not be to design the most optimized system possible; the emphasis is to show how an optimum system can be designed given the constraints one may encounter. For example, if a different high-energy neutron source becomes available, with a different energy and flux distribution than the one considered here; the entire optimization would have to be repeated for that source. Perhaps the system may need to be optimized for a geometry different than the one considered here. In any case, the emphasis of this thesis is to show it how neutron-diffraction systems for residual stress determination can be optimized, and to carry out one such optimization.

Chapter 2

Determination of Internal Stresses with Neutron Diffraction

This chapter develops the theory governing the use of neutron diffraction to determine internal stresses in large objects. Using this theory, source-moderator-detector combinations can be optimized. The methodology of neutron scattering is also examined, to see if there are ways of improving performance through new techniques.

2.1 Theory of Determining Stresses with Diffraction

In this section, the theory of stress and strain, as examined in appendix A is applied to neutron diffraction, to show how strains can be detected by using this technique. The theory is used to determine all six strain components present in a three-dimensional object. Simpler, one dimensional stress determination is also mentioned.

2.1.1 One Dimensional Strain Determination

A common method of determining residual stresses in a material is to use a well-collimated source beam, and a single well-collimated detector; positioned such that principal stresses lie along the change in wavenumber vector κ. This is the configuration shown in figure 1-1.

To obtain additional principal stresses, the specimen must be rotated, or the source and detector configuration altered such that κ lies along that principal stress.

The goal of these techniques is to determine the value of d (the interplanar spacing) for a given scattering angle. If the material is experiencing a strain in the direction of κ, then then d will have a different value than it would in an unstressed material, d_0. The value of d_0 for a given (h, k, l) plane can be easily calculated if one knows the basic dimensions of the unit cell, recalling that

$$d_0 = \frac{1}{|R_{h,k,l}|}; \text{ in a cubic material, } d_0 = \frac{a}{h^2 + k^2 + l^2}, \tag{2.1}$$

where R is given in equation A.15. Given the values of d and d_0, the strain in the direction κ is simply given by:

$$\epsilon = \frac{d - d_0}{d_0}. \tag{2.2}$$

This is a simple and effective method for determining the one-dimensional stress in an object with neutron diffraction. However, it will not be investigated further in this study, as it has several limitations. For example, the technique relies on the assumption of essentially one-dimensional stress; a risky assumption deep in large objects. It also assumes knowledge of the direction of that one-dimensional stress; this knowledge could be incorrect.

2.1.2 The Ewald Construction

Three dimensional diffraction, and its relationship to material strains can be visualized and explained rather simply with the Ewald construction. The incoming wave is described in terms of its wave number k, which equals $2\pi/\lambda$. Assuming elastic scattering, the outgoing wave will also have the same wavenumber k, but with a different direction, thus $|\vec{k_{in}}| = |\vec{k_{out}}|$. The change in direction is represented by $\vec{\kappa}$, where $\vec{\kappa} = \vec{k_{out}} - \vec{k_{in}}$.

For diffraction to occur, the vector $2\pi\vec{R}$ must equal $\vec{\kappa}$. In the case of a powder-like material, $|2\pi\vec{R}|$ must equal $|\vec{\kappa}|$, as displayed in figure 2-1. Notice that $|\vec{\kappa}|$ equals $2k\sin(\theta)$; substituting $\lambda = \frac{2\pi}{k}$, and $d = \frac{1}{R}$, one obtains the familiar Bragg relation: $\lambda = 2d\sin(\theta)$.

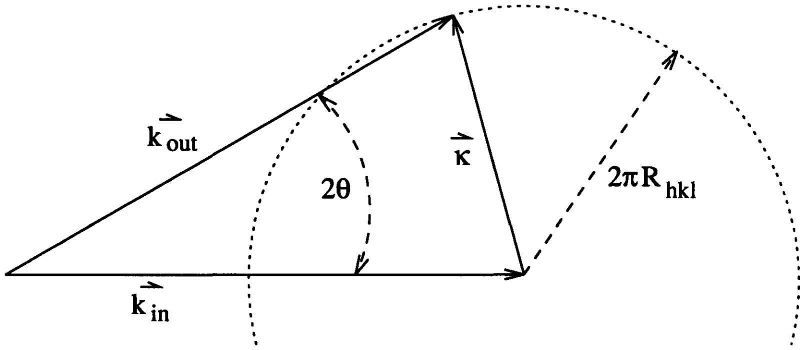

Figure 2-1: The Ewald Construction for Powder Diffraction

However, if a powder-like material is under a strain, then rotating the $\vec{R}$ vector through all the powder orientations does not yield a sphere; it yields an ellipsoid. This can be shown by starting with the relationship between an unstrained reciprocal vector $\vec{R}$ and a strained reciprocal vector $\vec{R^d}$, as shown in equation A.19:

$$|\vec{R}| = |\mathcal{E}\vec{R^d}|, \tag{from A.19}$$

where $\mathcal{E}$ is the strain tensor for the stained material, defined in equation A.7. Squaring both sides of equation A.19, then expanding $\mathcal{E}$ and $\vec{R^d}$ results in:

$$|\vec{R}|^2 = \left| \begin{bmatrix} 1+\epsilon_x & \frac{1}{2}\gamma_{xy} & \frac{1}{2}\gamma_{zx} \\ \frac{1}{2}\gamma_{xy} & 1+\epsilon_y & \frac{1}{2}\gamma_{yz} \\ \frac{1}{2}\gamma_{zx} & \frac{1}{2}\gamma_{yz} & 1+\epsilon_z \end{bmatrix} \begin{bmatrix} R_x^d \\ R_y^d \\ R_z^d \end{bmatrix} \right|^2, \tag{2.3}$$

where R_x^d, R_y^d, and R_z^d are the x, y, and z components of the $\vec{R^d}$ vector. Carrying out the matrix multiplication in equation 2.3 gives:

$$|\vec{R}|^2 = \left\{ \begin{array}{c} \left[(1+\epsilon_x)^2 + (\frac{1}{2}\gamma_{xy})^2 + (\frac{1}{2}\gamma_{zx})^2\right](R_x^d)^2 + \left[(\frac{1}{2}\gamma_{xy})^2 + (1+\epsilon_y)^2 + (\frac{1}{2}\gamma_{yz})^2\right](R_y^d)^2 + \\ \left[(\frac{1}{2}\gamma_{zx})^2 + (\frac{1}{2}\gamma_{yz})^2 + (1+\epsilon_z)^2\right](R_z^d)^2 + \left[(2+\epsilon_x+\epsilon_y)\gamma_{xy} + \frac{1}{2}\gamma_{yz}\gamma_{zx}\right]R_x^d R_y^d + \\ \left[(2+\epsilon_y+\epsilon_z)\gamma_{yz} + \frac{1}{2}\gamma_{zx}\gamma_{xy}\right]R_y^d R_z^d + \left[(2+\epsilon_z+\epsilon_x)\gamma_{zx} + \frac{1}{2}\gamma_{xy}\gamma_{yz}\right]R_z^d R_x^d \end{array} \right\} \tag{2.4}$$

The following substitutions simplify the equation for $|\vec{R}|^2$ considerably:

$$\begin{aligned} \eta_{xx} &= (1+\epsilon_x)^2 + (\tfrac{1}{2}\gamma_{xy})^2 + (\tfrac{1}{2}\gamma_{zx})^2, \quad \eta_{yy} = (\tfrac{1}{2}\gamma_{xy})^2 + (1+\epsilon_y)^2 + (\tfrac{1}{2}\gamma_{yz})^2, \\ \eta_{zz} &= (\tfrac{1}{2}\gamma_{zx})^2 + (\tfrac{1}{2}\gamma_{yz})^2 + (1+\epsilon_z)^2, \quad \eta_{xy} = (2+\epsilon_x+\epsilon_y)\gamma_{xy} + \tfrac{1}{2}\gamma_{yz}\gamma_{zx}, \\ \eta_{yz} &= (2+\epsilon_y+\epsilon_z)\gamma_{yz} + \tfrac{1}{2}\gamma_{zx}\gamma_{xy}, \quad \eta_{zx} = (2+\epsilon_z+\epsilon_x)\gamma_{zx} + \tfrac{1}{2}\gamma_{xy}\gamma_{yz}. \end{aligned} \tag{2.5}$$

Carrying out the substitutions results in the following simple equation for a general ellipsoid:

$$\eta_{xx}(R_x^d)^2 + \eta_{yy}(R_y^d)^2 + \eta_{zz}(R_z^d)^2 + \eta_{xy}R_x^dR_y^d + \eta_{yz}R_y^dR_z^d + \eta_{zx}R_z^dR_x^d = |\vec{R}|^2. \tag{2.6}$$

If several measurements of the radius of this ellipsoid are made, the magnitude of the η's can be computed. From these, the strain components can be determined.

2.1.3 3-Dimensional Determination of Strain Components

This section shows how several diffraction measurements and equation 2.4 can be manipulated to determine all six of the components of $\mathcal{E}$. First, equation 2.6 must be converted into units that are measured in a diffraction experiment, such as the scattering angle (θ), the azmuthal scattering angle (ϕ), and the wavelength of the scattered neutron (λ). In the simplest case, the coordinate system shown in figure 2-2 is imposed on the scattering experiment. Then the Z-axis lies along the axis of the neutron beam. The X axis is set at a convenient azmuthal location, with the Y-axis orthogonal to the X and Z axii. The azmuthal angle ϕ measures rotation about the Z-axis; its value is zero along the X-axis.

Since we know that $|\vec{R}| = |\kappa|$ when bragg scattering occurs, we can determine the values of R_x^d, R_y^d, and R_z^d geometrically using figure 2-2:

$$\begin{aligned} 2\pi R_x^d &= k\cos(\phi)\sin(2\theta), \\ 2\pi R_y^d &= k\sin(\phi)\sin(2\theta), \\ 2\pi R_z^d &= k[\cos(2\theta) - 1]. \end{aligned} \tag{2.7}$$

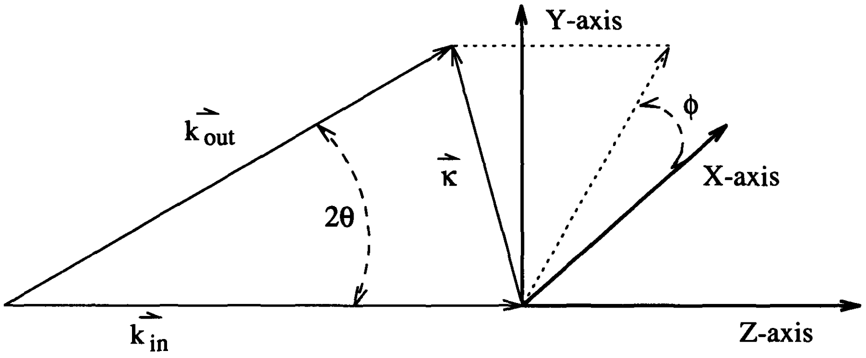

Figure 2-2: Simple Stain Determination Coordinate System

Now if the following substitutions are made;

$$\begin{aligned} x(\phi,\theta) &= \cos(\phi)\sin(2\theta), \\ y(\phi,\theta) &= \sin(\phi)\sin(2\theta), \\ z(\theta) &= \cos(2\theta)-1, \end{aligned} \tag{2.8}$$

equation 2.3 can be re-written as:

$$\left|\mathcal{E}\begin{bmatrix} x(\phi,\theta) \\ y(\phi,\theta) \\ z(\theta) \end{bmatrix}\right|^2 = \frac{|\vec{R}|^2}{k^2} = \frac{\lambda^2}{d_0^2}, \tag{2.9}$$

or

$$f(\phi,\theta,\mathcal{E}) = g(\lambda,d_0). \tag{2.10}$$

If one was to simulate the diffraction process through a strained material, it might be necessary to determine the value of θ for a given set of ϕ, $\mathcal{E}$, λ, and d_0 values. Such a determination could be done numerically; however this could be time-consuming if a large number of determinations must be made. Appendix B shows an analytical method for determining θ.

Least Squares Analysis

This section is a brief introduction to the method of least squares analysis. It is a method which can be used to solve for the strain components in equation 2.10. It is also useful because it can predict the uncertainty in the determined strain components. The topic is much more thoroughly explored in [8], which gives many examples of applications where the least squares method can be applied.

Say one would like to solve for the p values of a_k $(k = 1, 2, ..., p)$ in the following generalized equation of m independent variables x_j $(j = 1, 2, ..., m)$ with uncertainties σ_{x_j} and o dependent variables y_l $(l = 1, 2, ..., o)$ with uncertainties σ_{y_l}:

$$f(a_1, a_2, ..., a_p, x_1, x_2, ..., x_m) = g(y_1, y_2, ..., y_o) \tag{2.11}$$

Now say n sets of data are collected at each of the (x_{ij}, y_{il}) $(i = 1, 2, ..., n)$ data points. To solve for the a_k's and σ_{a_k} 's, one would start by defining the three matrices **R**, **A**, and **L** as follows, using approximate guess values for the a_k's:

$$R_i = g(y_{i1}, y_{i2}, ..., y_{io}) - f(a_1, a_2, ..., a_p, x_{i1}, x_{i2}, ..., x_{im}) \quad i = 1, 2, ..., n \tag{2.12}$$

$$A_{ik} = \frac{\partial F_i}{\partial a_k} \quad L_i = \sum_{j=1}^{m}\left(\frac{\partial F_i}{\partial x_{ij}}\sigma_{x_{ij}}\right)^2 + \sum_{l=1}^{o}\left(\frac{\partial F_i}{\partial y_{il}}\sigma_{y_{il}}\right)^2 \quad \begin{matrix} k = 1, 2, ..., p \\ i = 1, 2, ..., n \end{matrix} \tag{2.13}$$

With **R**, **A**, and **L** determined, the matrices **C** and **V** can be calculated:

$$C_{hk} = \sum_{i=1}^{n}\frac{A_{ih}A_{ik}}{L_i} \quad V_k = \sum_{i=1}^{n}\frac{A_{ik}R_i}{L_i} \quad \begin{matrix} h = 1, 2, ..., p \\ k = 1, 2, ..., p. \end{matrix} \tag{2.14}$$

Then, the a_k and σ_{a_k} values can be found:

$$a_k = a_{k\ guess} + \sum_{h=1}^{p}\mathbf{C}^{-1}{}_{kh}V_h \quad \sigma_{a_k} = \mathbf{C}^{-1}{}_{kk} \quad \begin{matrix} h = 1, 2, ..., p \\ k = 1, 2, ..., p \end{matrix} \tag{2.15}$$

If the initial guess values for the a_k's are significantly different from the calculated values, then equations 2.12 through 2.15 should be repeated, using the calculated a_k's as guess values in each iteration, until the input and output values of the a_k's are approximately equal.

Strain Determination by Least Squares Analysis

The method of Least squares can be easily applied to the job of determining strain components from neutron scattering data. It is especially useful, for it can be used to estimate the uncertainty in the determined values of the strain components. There are alternatives to the method of least squares, of course, but it is assumed that the errors in the calculated strain values will be approximately the same.

During a given diffraction experiment, measurements must be made at several values of θ and ϕ. Say n measurements are taken, each measurement i yielding a set of values for ϕ_i, θ_i, λ_i, d_i, and I_i; where I_i is the integrated intensity of the ith measurement. The method of least squares requires a set of guess values for the strain components; assuming that the strains are small, setting them all to zero initially does not change the output strain values significantly; further iterations are generally unnecessary. Using equations 2.10, A.15 and 2.13, the following assignments can be made:

$$R_i = g(\lambda_i, d0_i) - \lim_{\mathcal{E}\to\mathbf{I}} f(\phi_i, \theta_i), \qquad \mathbf{I} = \begin{bmatrix} 1 & 0 & 0 \\ 0 & 1 & 0 \\ 0 & 0 & 1 \end{bmatrix}, \tag{2.16}$$

$$A_{ij} = \lim_{\mathcal{E}\to\mathbf{I}} \begin{bmatrix} \frac{\partial f(\phi_i,\theta_i)}{\partial \epsilon_x} & \frac{\partial f(\phi_i,\theta_i)}{\partial \epsilon_y} & \frac{\partial f(\phi_i,\theta_i)}{\partial \epsilon_z} & \frac{\partial f(\phi_i,\theta_i)}{\partial \gamma_{xy}} & \frac{\partial f(\phi_i,\theta_i)}{\partial \gamma_{yz}} & \frac{\partial f(\phi_i,\theta_i)}{\partial \gamma_{zx}} \end{bmatrix}_j \quad j = 1, 2, ..., 6 \tag{2.17}$$

$$L_i = \lim_{\mathcal{E}\to\mathbf{I}} \left[(\frac{\partial g(\lambda_i, d0_i)}{\partial \lambda}\sigma_\lambda)^2 + (\frac{\partial g(\lambda_i, d0_i)}{\partial d0}\sigma_{d0})^2 + (\frac{\partial f(\phi_i, \theta_i)}{\partial \phi}\sigma\phi)^2 + (\frac{\partial f(\phi_i, \theta_i)}{\partial \theta}\sigma\theta)^2 \right] \tag{2.18}$$

Since $f(\phi, \theta)$ and $g(\lambda, d0)$ have already been defined in equations 2.9 and 2.10, these assignments can be simplified considerably:

$$A_{ij} = 2\begin{bmatrix} x(\phi_i,\theta_i)^2 & y(\phi_i,\theta_i)^2 & z(\theta_i)^2 & x(\phi_i,\theta_i)y(\phi_i,\theta_i) & y(\phi_i,\theta_i)z(\theta_i) & z(\theta_i)x(\phi_i,\theta_i) \end{bmatrix}_j \tag{2.19}$$

$$R_i = \frac{\lambda_i^2}{d_i^2} - (2\sin(\theta_i))^2 \tag{2.20}$$

$$L_i = \left\{ \frac{\lambda_i^4}{d_i^4}\left[(\frac{2}{\lambda_i}\sigma\lambda_i)^2 + (\frac{2}{d_i}\sigma d_i)^2 \right] + (4\sin(2\theta_i)\sigma\theta_i)^2 \right\} I_i^{-1} \tag{2.21}$$

Once equations 2.19 through 2.21 are calculated, the matrices **C** and **V** can be determined;

$$\mathbf{C} = \sum_i \frac{\mathbf{A}_i^T\mathbf{A}_i}{L_i} \qquad \mathbf{V} = \sum_i \frac{\mathbf{A}_i^T R_i}{L_i}, \tag{2.22}$$

leading to the results:

$$\begin{bmatrix} \epsilon_x \\ \epsilon_y \\ \epsilon_z \\ \gamma_{xy} \\ \gamma_{yz} \\ \gamma_{zx} \end{bmatrix} = \mathbf{C}^{-1}\mathbf{V}, \text{ and } \begin{bmatrix} \sigma_{\epsilon_x} & \cdot & \cdot & \cdot & \cdot & \cdot \\ \cdot & \sigma_{\epsilon_y} & \cdot & \cdot & \cdot & \cdot \\ \cdot & \cdot & \sigma_{\epsilon_z} & \cdot & \cdot & \cdot \\ \cdot & \cdot & \cdot & \sigma_{\gamma_{xy}} & \cdot & \cdot \\ \cdot & \cdot & \cdot & \cdot & \sigma_{\gamma_{yz}} & \cdot \\ \cdot & \cdot & \cdot & \cdot & \cdot & \sigma_{\gamma_{zx}} \end{bmatrix} = \mathbf{C}^{-1}. \tag{2.23}$$

2.2 Strain Detection Methodology

Equations 2.19 through 2.21 require values for d_0, σ_{d0}, θ, σ_θ, λ, σ_λ, ϕ, and I. These values can be determined in one of two ways; by setting the value of λ with a monochromator and determining the values of θ at several values of d_0, or by pulsing the neutron beam, and measuring the flight time of a given neutron arriving at a given θ; from the flight time and θ, the wavelength for a given value of d_0 can be determined.

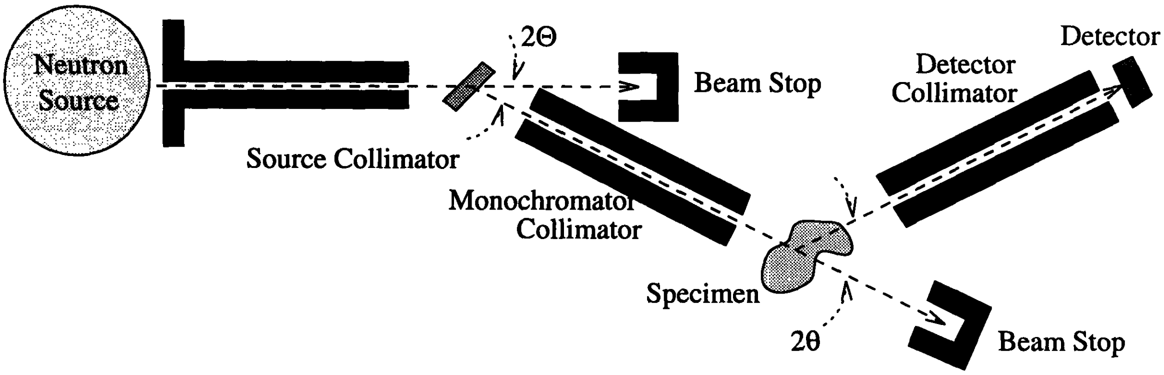

Figure 2-3: Diffraction with Monochromatic Beam

2.2.1 Strain Determination with a Monochromatic Beam

In this method, shown in figure 2-3, a monochomatic beam is obtained by diffracting the collimated source beam through a high-purity crystal with a high cross section for coherent scattering. At a given angle 2Θ, most of the scattering neutrons will have the same wavelength. This beam coming out of the monochromating crystal is collimated to remove neutrons scattered at other angles, then used for diffraction through the specimen. The direction of this monochromatic, collimated beam is used as a reference for $\theta = 0$ in scattering through the specimen.

For a given wavelength λ, obtained from the monochromator, and a given scattering plane with spacing d_0, one would expect a peak in detected neutrons near the value $2\theta_0$, where $\theta_0 = \sin^{-1}(\frac{\lambda}{2d_0})$. The detector scans through a small angular range around $2\theta_0$, and measures the intensity of the beam scattered off the specimen at each incremental value of 2θ. At some value of θ, there will be a peak in the intensity of the diffracted beam, at θ_{peak}. If a linear position-sensitive detector is used with this technique, some time can be saved, as the entire angular range around the peak can be scanned simultaneously.

With the values of d_0, θ, and λ, determined, their uncertainties may be determined. It is assumed here that σ_{d0} is essentially zero. The values θ and λ represent the mean values of a gaussian distributions. Their uncertainties, σ_θ and σ_λ represent the width of the gaussian distributions. For a given peak, the actual uncertainty in the means is given by $\frac{\sigma}{\sqrt{I}}$, where I is the the integrated number of bragg scattered neutrons in the peak. This uncertainty in the means is reflected by the I^{-1} term in equation 2.21.

The width of the angle distribution, σ_θ arises from uncertainties in the monochromization process and the detection process, meaning that σ_θ is composed of two components:

$$\sigma_\theta = \sqrt{\sigma_\theta(\Theta)^2 + \sigma_{\theta d}^2}. \tag{2.24}$$

The contribution to uncertainty from monochromization $(\sigma_\theta(\theta))$ has two components also; one component (σ_Θ) due to uncertainty in monochromization when the neutrons are detected in the "scattering plane", where the scattering plane contains the "parallel" and "anti-parallel" detector locations; and the other component $(\sigma_\Theta \perp)$ due to uncertainty in monochromization when the neutrons are detected perpendicular to the scattering plane. The uncertainty component in the scattering plane is given by [1],

$$\sigma_\Theta^2 = \frac{\alpha_0^2\eta_M^2 + \alpha_1^2\eta_M^2 + \alpha_0^2\alpha_1^2}{\alpha_0^2 + \alpha_1^2 + 4\eta_M^2}, \tag{2.25}$$

where α_0 and α_1 are measures of the collimation in the monochromator scattering plane, and η_M is a measure of the mosaic spread of the monochromating crystal. α_0 represents the collimation before the monochromator, while α_1 measures of the collimation after the monochromator. There also are two values, β_0 and β_1, which refer to collimation perpendicular to the monochromator scattering plane. The uncertainty perpendicular to the scattering plane $(\sigma_{\Theta\perp})$ can be determined from

$$\sigma_{\Theta\perp}^2 = \frac{\beta_0^2\eta_M^2 + \beta_1^2\eta_M^2 + \beta_0^2\beta_1^2}{\beta_0^2 + \beta_1^2 + 4\eta_M^2}, \tag{2.26}$$

Since longer wavelength neutrons tend to scatter at larger angles, there is some correlation between the uncertainty in wavelength and angle. It is well established that

---

[1] Adapted from Windsor[41, page 208]

detectors should be placed in the "parallel" position ($\phi = 0$ in our geometry); this generally results in a sharper peak. In the "anti-parallel" position, the peaks are much wider. This can be explained if we observe two beams of neutrons exiting the monochromator at angles $\pm\sigma_\Theta$. Assuming the centerline of the beams lies at an angle Θ_0 relative to the source beam, the neutrons scattering at $\Theta_0 + \sigma_\Theta$ will have a wavelength of $2d_m(\sin(\theta_0) + \cos(\Theta_0)\sigma_\Theta)$. The neutrons scattering at $\Theta_0 - \sigma_\Theta$ will have a wavelength of $2d_m(\sin(\theta_0) - \cos(\Theta_0)\sigma_\Theta)$. Now suppose there is a plane in the powder sample with a spacing of d_0. The neutrons originally scattered at $\Theta_0 + \sigma_\Theta$ will diffract at an angle of $\sin^{-1}(\frac{d_m}{d_0}(\sin(\theta_0) + \cos(\Theta_0)\sigma_\Theta)) - \cos(\phi)\sigma_\Theta$, while the neutrons originally scattered at $\Theta_0 - \sigma_\Theta$ will diffract at an angle of $\sin^{-1}(\frac{d_m}{d_0}(\sin(\theta_0) + \cos(\Theta_0)\sigma_\Theta)) + \cos(\phi)\sigma_\Theta$. If these two values are taken as the high and low values of a $\pm\sigma_\theta$ distribution, and some substitutions are made, then $\sigma_\theta(\Theta) \approx |\sigma_\Theta \tan(\theta) \cot(\Theta_0) - \cos\phi\sigma_\Theta|$.

In a similar manner, scattering perpendicular to the parallel/antiparallel plane can be modeled, yielding a total equation for $\sigma_\theta(\Theta)$:

$$\sigma_\theta(\Theta) = |\sigma_\Theta \tan(\theta) \cot(\Theta_0) - \cos\phi\sigma_\Theta| + \sin^2(\phi)\sigma_{\Theta\perp} \tag{2.27}$$

When $\alpha_0 = \beta_0$ and $\alpha_1 = \beta_1$, measurements can be made at several values of ϕ simultaneously, because the uncertainty in Θ is relatively equal same at all values of ϕ (although σ_θ is usually at a minimum when $\phi = 0$). When the β's much are greater than the α's, reliable measurements can only be made at $\phi = 0$ and $\phi = \pi$, but the intensity tends to be much higher, requiring a much shorter count time. One could conceivably make several consecutive measurements at different values of ϕ, rotating the collimator and detector after each measurement, in less time than is required for several simultaneous measurements when the α's equal the β_1's. Which scenario is faster in practice depends on the number of available detectors, and the available range of the β's.

Uncertainty in angle due to the detection process ($\sigma_{\theta d}$) arises from the fact that scattering takes place deep within the sample, and must be collimated before being detected.

The uncertainty in angle due to this process is given by

$$\sigma_{\theta d} = \frac{\alpha_2}{\sqrt{2\pi}}, \tag{2.28}$$

where α_2 is a measure of the divergence of the detector collimator in the scattering plane.

Since the wavelength is set by the monochromator, the uncertainty in λ is a function of only λ, Θ, and σ_Θ, as follows:

$$\sigma_\lambda = \lambda \cot(\Theta)\sigma_\Theta \tag{2.29}$$

Recalling that $\sigma_{d0} = 0$, equation 2.21 can be simplified to:

$$L_i = [64 \sin^4(\theta_i) \cot^2(\Theta)\sigma_\theta^2 + 16 \sin^2(2\theta_i)(\sigma_\theta^2 + \sigma_\theta^2)]I_i^{-1}. \tag{2.30}$$

If perfect monochromization is assumed ($\sigma_\theta(\Theta) = 0$), then

$$L_i = [16 \sin^2(2\theta_i)\sigma\theta_i^2]I_i^{-1}. \tag{2.31}$$

Monochromatic Backscattering Geometry

In general, whenever the value of the L's in equation 2.23 are reduced, the uncertainties in the strains are reduced also. In the case where near-perfect monochromization is assumed ($\sigma_\theta(\Theta) \ll \sigma_{\theta d}$), L varies with $\sin^2(2\theta)$, indicating that larger values of θ will tend to result in greater certainty in the the strains. The obvious conclusion would be to use backscattering; however, when using backscattering in the geometry of figure 2-3, the sampled volume is not well defined. One solution to this dilemma is to change the geometry to that of figure 2-4.

Figure 2-4 illustrates a geometry appropriate for making measurements via backscatter diffraction. Two beams are shown coming out of the source, converging at a point in the sample. For now, the two beams represent two possible locations of one rotatable beam. The beam makes an angle θ_b with respect to the axis of rotation of the beam. The rotation of the beam is measured by ϕ_b. It is assumed that the beam is attached to position sensitive

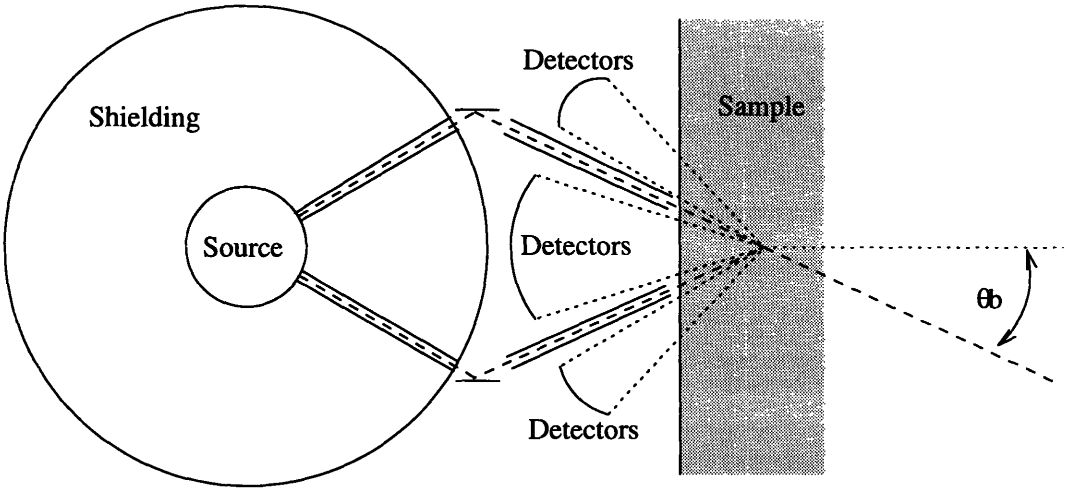

Figure 2-4: Geometry for Backscattering Strain Determination

detectors, which rotate with the beam, capable of measuring the θ and ϕ of neutrons relative to the beam.

It is helpful to image a coordinate system, (Xb, Yb, and Zb) rigidly attached to the beam and detector system, as shown in figure 2-5. The beam rotates around the Z axis, while neutrons enter the specimen along the Zb axis, scattering with an angle 2θ relative to that axis, at all angles of ϕ. It is assumed that the linear position detectors detect the scattering, and are able to detect a θ_{peak} at each value of ϕ.

With backscattering configuration, the first step would be to choose a value of θ_b such that neutrons diffract from the sample at an angle θ, where $\frac{\pi}{2} - 2\theta < \theta_b$. Then the beam and attached detectors would be rotated through the range of ϕ_b, stopping at incremental values of ϕ_b to make measurements of the peak θ values at some selected ϕ values relative to the beam.

Now, for each peak, there will be 4 values: θb, ϕ_b, θ, and ϕ. These can be evaluated using equations 2.19 through 2.23, if a few definitions are made. First, it is assumed that when $\phi_b = 0$, the Y-axis and Yb-axis are aligned; so the Xb axis and the Zb axis lie in the same plane as the X and Z axis, rotated around the Y axis by the angle θb. When ϕ_b

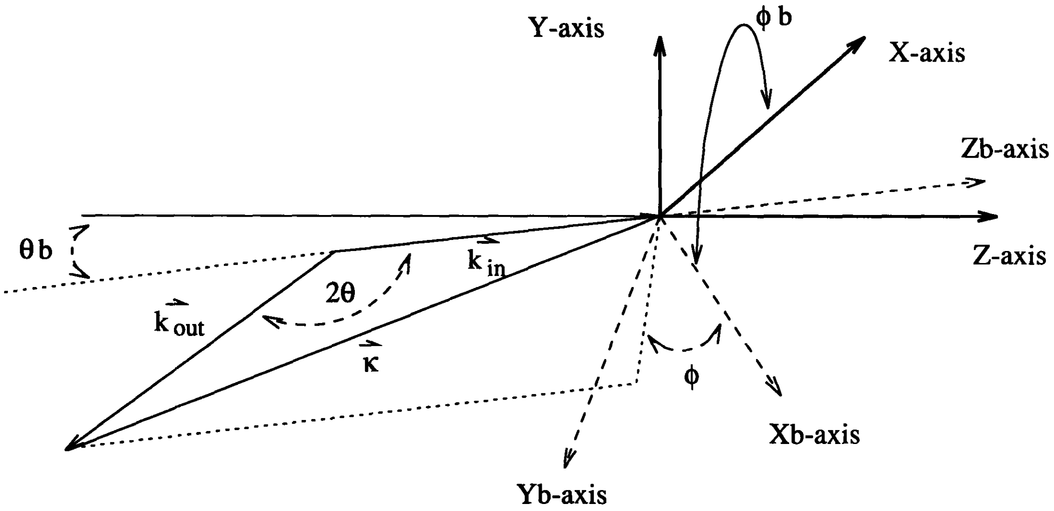

Figure 2-5: Coordinate System for Backscattering Strain Determination

is non-zero, the entire (Xb, Yb, Zb) coordinate system is rotated around the Z axis by an angle ϕ_b. Then the equations for x, y, and z in 2.8 can be re-written to account for the new geometry:

$$\begin{aligned} xb(\phi_b, \theta b, \phi, \theta) &= \{x(\phi,\theta)\cos(\theta b) - z(\theta)\sin(\theta b))\}\cos(\phi_b) - y(\phi,\theta)\sin(\phi_b) \\ yb(\phi_b, \theta b, \phi, \theta) &= \{x(\phi,\theta)\cos(\theta b) - z(\theta)\sin(\theta b))\}\sin(\phi_b) + y(\phi,\theta)\cos(\phi_b) \\ zb(\phi_b, \theta b, \theta) &= x(\phi,\theta)\sin(\theta b) + z(\theta)\cos(\theta b)) \end{aligned} \tag{2.32}$$

Now xb, yb, and zb can be substituted for x, y, and z in equations 2.19 through 2.21. Surprisingly, the values for L and R remain unchanged; the only difference is that A is now a function of xb, yb, and zb instead of x, y, and z.

There is an alternate configuration for performing strain measurements with backscattering. In the alternate configuration, multiple beams simultaneously converge on the sample volume, at many values of ϕ_b. Instead of rotating position sensitive detectors, fixed area-sensitive detectors are used. Because of interference, only two values of ϕ can be used: 0 and π. At each value of ϕ_b, a cone of neutrons intersects the detectors, creating an overlapping

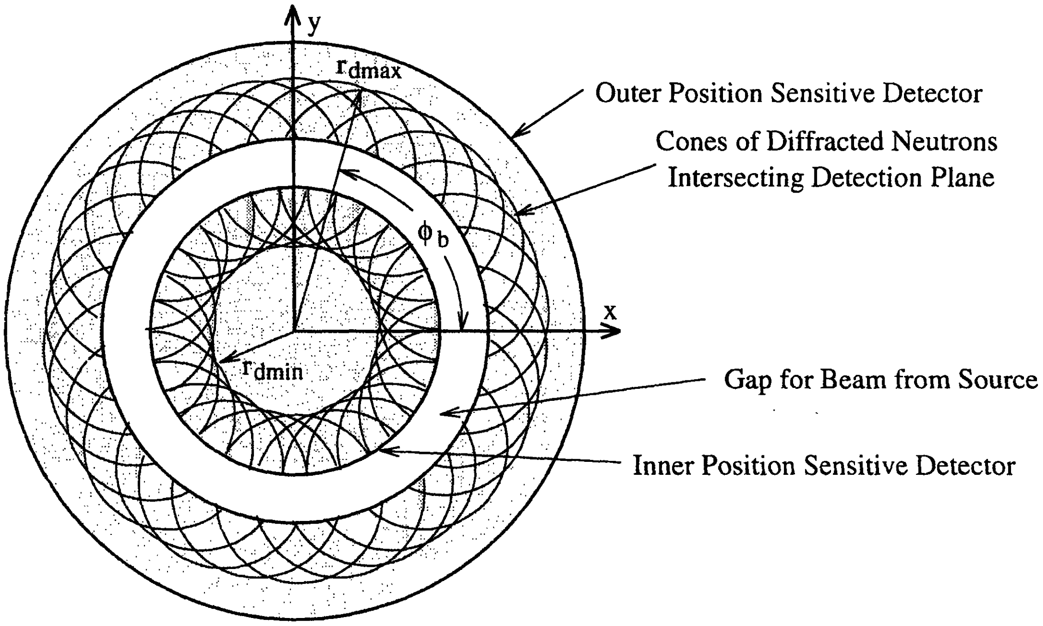

Figure 2-6: Pattern of Backscattered Neutrons on Area Detector

pair of rings on the detectors, resulting a pattern similar to that shown on figure 2-6.

The neutron intensity per unit ϕ_b will tend to peak at rd_{max} and rd_{min} on the detectors, corresponding to diffraction at $\phi = 0$ and $\phi = \pi$. If $\frac{\pi}{2} - 2\theta < \theta b$, then rd_{min} will always be on the inner detector, while rd_{max} will always be on the outer detector. An example of the intensity distribution one might expect is shown in figure 2-7. From the values rd_{min} and rd_{max}, and the distance from the center of the detectors to the sampled volume (Z), values for theta can be obtained, since:

$$\tan[\theta b + (\pi - 2\theta)] = \frac{rd_{max}}{Z} \quad @ \quad \phi = 0 \tag{2.33}$$

$$\tan[\theta b - (\pi - 2\theta)] = \frac{rd_{min}}{Z} \quad @ \quad \phi = \pi \tag{2.34}$$

In addition to the advantage of gaining accuracy because of the use of backscattered neutrons, this technique allows one to make several measurements simultaneously, despite the fact that β_1 may be much larger than α_1, since ϕ is always measured at 0 and π. A major disadvantage of this technique are that it requires several well aimed monochromators,

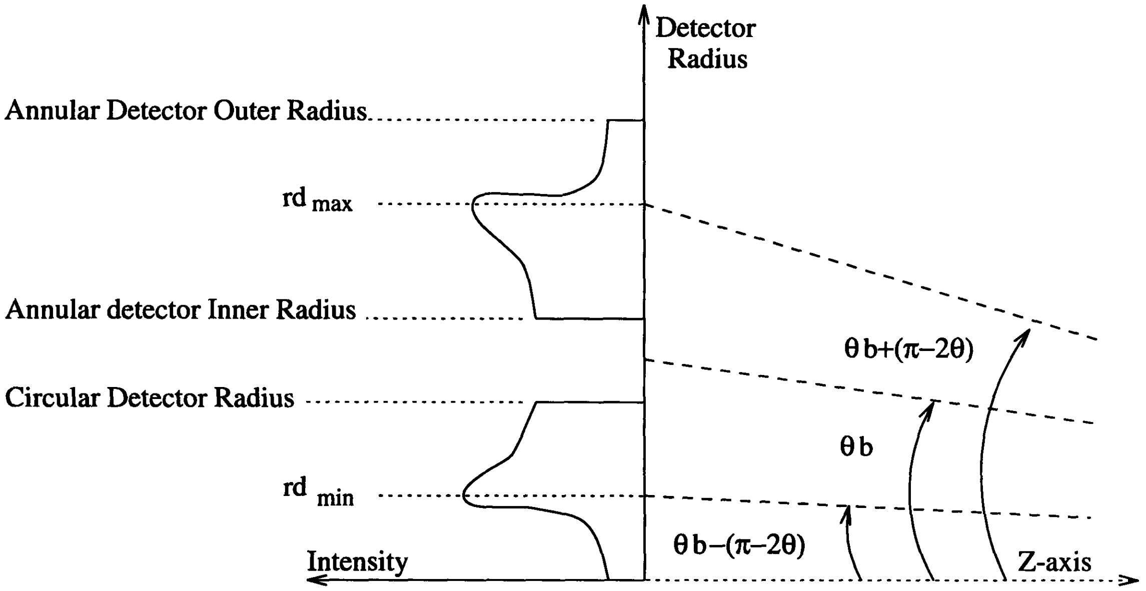

Figure 2-7: Intensity of Backscattered Neutrons on Area Detector

which could be costly and difficult to set up. It also requires concentric focusing collimators on the detectors, which may be difficult to fabricate. In addition, it may be difficult to use with more than one backscattering cone. Finally, it may be difficult to determine the values of rd_{min} and rd_{max}, because they represent the peaks of the unusual function shown in figure 2-7.

2.2.2 Intensity from Monochromatic measurements

To calculate the intensity of a measurement when considering monochromatic neutron diffraction, several factors must be considered. The source distribution of neutrons must be modeled and characterized; all three sets of collimators must be considered; the scattering by the monochromator and the sample must be considered; and losses due to attenuation by the sample and detector inefficiencies must all be accounted.

Steady-State Source Characterization

Assuming that the neutrons coming from a source are at equilibrium at a temperature T, the flux of neutrons emerging per unit wavelength at λ is given by the Maxwellian curve

$$\frac{\partial\Phi}{\partial\lambda} = \frac{2\Phi_0}{\lambda}\left(\frac{E}{kT}\right)e^{-E/\mathbf{k}T}, \tag{2.35}$$

where $\mathbf{k}$ is Boltzmann's constant, E is the neutron energy, and Φ_0 is the total thermal flux, integrated over all λ [21, page 3]. This equation can be re-written in terms of λ, to eliminate E;

$$\frac{\partial\Phi}{\partial\lambda} = \frac{\Phi_0}{2}\frac{\mathbf{h}^4}{m^2\mathbf{k}^2T^2\lambda^5}\exp\left(-\frac{2m\mathbf{k}T\lambda^2}{\mathbf{h}^2}\right). \tag{2.36}$$

In a real source, with a non-infinite moderator, the temperature of the neutron distribution is always hotter than the temperature of the moderator. Figure 2-8 shows the relationship between moderator temperature and neutron temperature, for a beams emerging from a 20 cm high by 20 cm diameter moderators of CH_4, C_2H_6, and H_2O[2]. Smaller moderators would have resulted in higher neutron spectral temperatures; bigger moderators would have resulted in lower spectral temperatures.

Also, in a real source, there is a short wavelength, non-Maxwellian component to the spectrum. The short wavelength component is usually a function of the moderator geometry. In the case of a small, spherical moderator with the beam sampled close to the neutron source, the high energy portion of the distribution falls of as $1/\lambda$, disappearing within the Maxwellian. Figure 2-9 shows the results of a monte carlo simulation of the distribution of neutrons from 6 cm radius moderators of H_2O and CH_4, sampled at 2 cm from the neutron source. The curves shown fitting the points are of the form

$$\frac{\partial\Phi}{\partial\lambda} = \frac{\Phi_0}{2}\frac{\mathbf{h}^4}{m^2\mathbf{k}^2T^2\lambda^5}\exp\left(-\frac{\mathbf{h}^2}{2m\mathbf{k}T\lambda^2}\right) + \frac{\Phi_1}{\lambda}\exp\left(-\frac{2m\mathbf{k}T\lambda^2}{\mathbf{h}^2}\right), \tag{2.37}$$

where Φ_1 is simply an empirical value required to fit the high-energy end of the function.

---

[2] Data adapted from Carpenter [40, page 173]

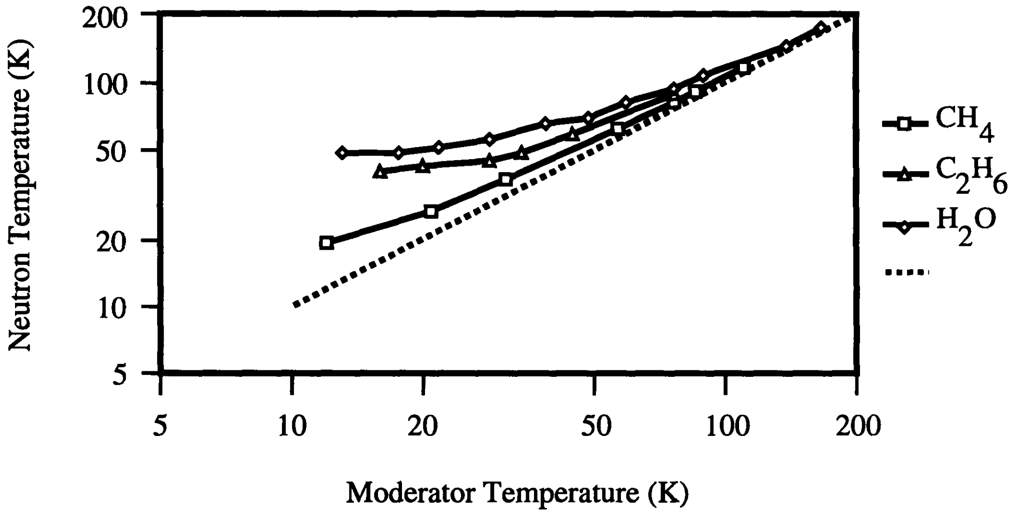

Figure 2-8: Dependence of Neutron Spectral Temperature on Moderator Temperature

The simulation resulted in a spectral temperatures of 25.8K for the CH_4 at 4K, and 307K for the H_2O at 300K. These results are consistent with Carpenter's results shown in figure 2-8. At high temperatures, the spectral temperature approaches the moderator temperature; at low temperatures, the spectral temperature remains much higher.

Calculation of Intensity Reaching Sample

The amount of neutron flux at a particular wavelength scattered by a particular reflection of a monochromating crystal is determined primarily by the Q value , which is given by

$$Q = \frac{\lambda^3 N_c^2}{\sin(2\theta)} F^2, \tag{2.38}$$

where Nc is the number of unit cells per unit volume, and F^2 is the scattering factor for the reflection in question. Assuming a regular crystalline lattice, the structure factor can

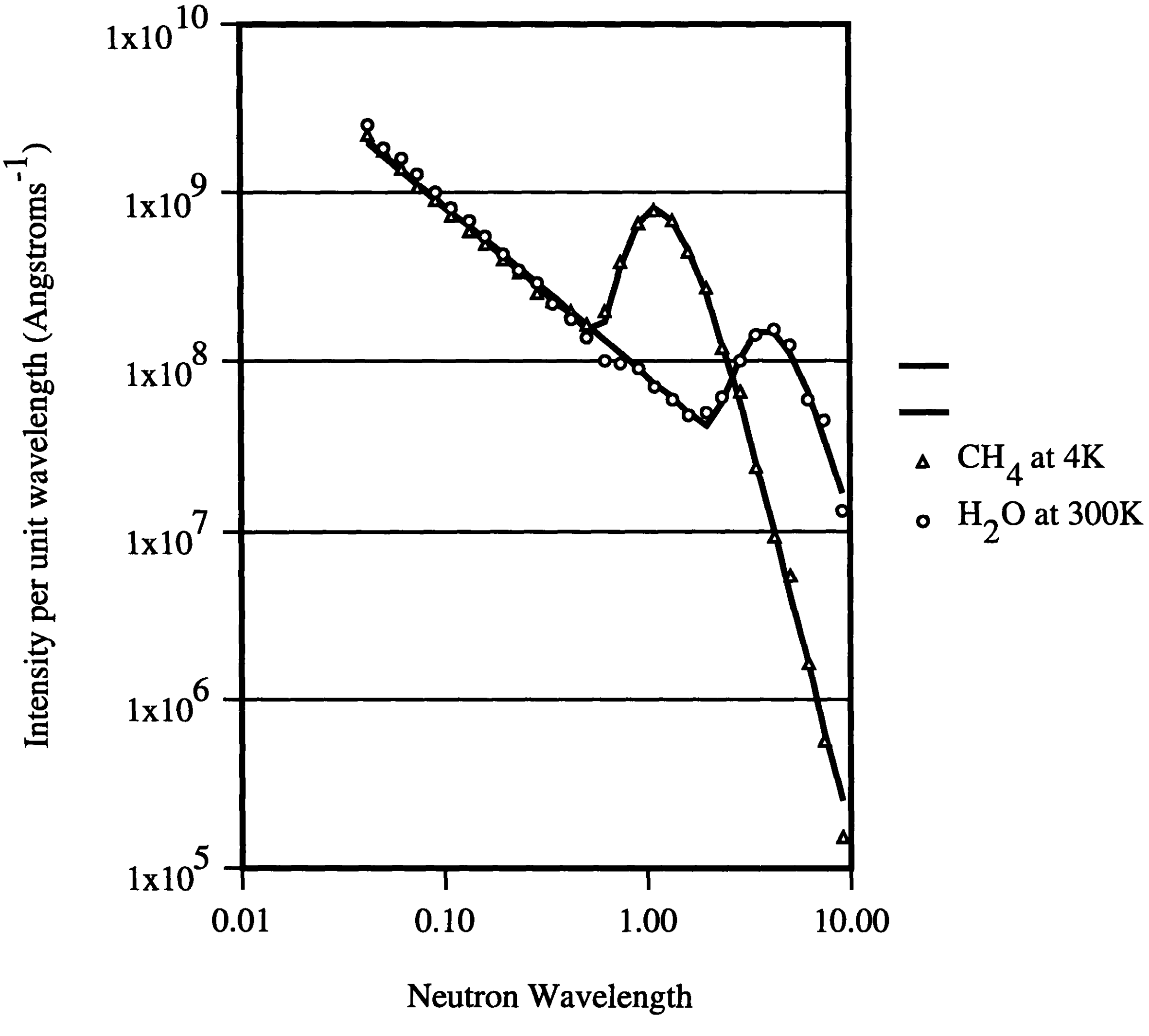

Figure 2-9: Two Example Spectra Calculated with Monte Carlo Code

be calculated from the formula

$$F^2 = \sum_j b_j \exp(2\pi i \vec{p}_j \vec{r}_j) \quad (j = 1..n), \tag{2.39}$$

where b_j is the scattering length of the jth atom in the unit cell, $\vec{r}_j$ is a vector representing the fractional position of the jth atom in the unit cell, $\vec{p}$ is a vector of the indices of the reflection in question, and n is the number of atoms in the unit cell. For example, if the monochromator material is crystalline copper, the structure of the unit cell will be face centered cubic (FCC). Thus

$$\begin{array}{l} j = 1..4, \\ b_j = b_{Cu}, \end{array} \quad \vec{p}_1 = \begin{bmatrix} 0 \\ 0 \\ 0 \end{bmatrix}, \ \vec{p}_2 = \begin{bmatrix} 0.5 \\ 0.5 \\ 0 \end{bmatrix}, \ \vec{p}_3 = \begin{bmatrix} 0.5 \\ 0 \\ 0.5 \end{bmatrix}, \ \vec{p}_4 = \begin{bmatrix} 0 \\ 0.5 \\ 0.5 \end{bmatrix}, \ \vec{r} = \begin{bmatrix} h \\ k \\ l \end{bmatrix}, \tag{2.40}$$

where (h, k, l) are the indices of the reflection. Using these values, when the (h, k, l) are all even or all odd, $F^2 = 16 b_{Cu}^2$; when they are mixed even and odd, $F^2 = 0$.

There is a thermal term which can be added to equation 2.38, which accounts for the reduction in intensity at a particular wavelength due to inelastic scattering. This reduction is given by the Debye factor (e^{-W}), where

$$W = \frac{6\mathbf{h}}{m_a \mathbf{k} \Theta_d^2} \frac{T}{4 d_0^2} \left[\phi(\frac{\Theta_d}{T}) + \frac{1}{4} \frac{\Theta_d}{T} \right], \text{ and} \tag{2.41}$$

$$\phi(x) = \frac{1}{x} \int_0^x \frac{\xi}{e^{\xi} - 1} d\xi, \text{ so} \tag{2.42}$$

$$W \simeq \frac{6\mathbf{h}}{m_a \mathbf{k} \Theta_d^2} \frac{T}{4 d_0^2} \left[1 + \frac{1}{36} \frac{\Theta_d^2}{T^2} + \frac{1}{3600} \frac{\Theta_d^4}{T^4} \right]. \tag{2.43}$$

T is the real temperature of the crystal, Θ_d is the Debye temperature of the crystal, and m_a is the atomic mass of the atoms in the crystal. The plane spacing of the material is given by d_0, where $d_0 = \frac{a}{\sqrt{h^2+k^2+l^2}}$. Table 2.1 gives the Debye temperature for several common materials, along with values for the unit cell size a, and the scattering length b.

Table 2.1: **Crystallographic Parameters for Several Common Materials**
Debye temperatures from [12], Lattice constants from [10], Coherent Scattering Lengths from [13].

Element	Structure Type	Atomic Weight	Debye Temperature K, Range in Literature	Lattice Constants Å	Coherent Scattering Length 10^{-12} cm
C	Diamond	12.0	1800 to 2242	a=3.5565	0.6646
C	Hexagonal	12.0	not found	a=2.4612, c=6.7079	0.6646
Cu	F.C.C.	63.5	304 to 342	a=3.6150	0.7718
Fe	B.C.C.	55.9	355 to 467	a=2.8663	0.9546
Ge	Diamond	72.6	211 to 400	a=5.6575	0.8193
Ni	F.C.C.	58.7	375 to 476	a=3.5241	1.031
Pb	F.C.C.	207.2	78 to 105	a=4.9505	0.9405
Si	Diamond	28.1	505 to 658	a=5.4305	0.4149
W	B.C.C.	183.9	270 to 384	a=3.1652	0.4775

For a material such as graphite, whose Debye Temperature could not be found in the literature, there is a simple relation for approximating the Debye temperature from the specific heat of the material. This relationship is:

$$C_v = 9N_A nk \left(\frac{T}{\Theta_d}\right)^3 \int_0^{\frac{\Theta_d}{T}} \frac{e^\xi}{(e^\xi - 1)^2}\xi^4 \, d\xi, \tag{2.44}$$

where C_v is constant-volume specific heat, and N_A is Avogadro's Number [11]. For graphite, using the values $C_v = 2.08\frac{cal}{K\,mole}$ at $300\,K$, we find $\Theta_d = 72.5\,K$.

With Q determined, the reflectivity of the monochromating crystal can be estimated. Assuming the geometry shown in 2-10, the reflectivity R for a crystal is given by

$$R = \int_{-\infty}^{\infty} \frac{A(Q,\mu,\eta,\Delta)}{[1 + A(Q,\mu,\eta,\Delta)] + \sqrt{1 + 2A(Q,\mu,\eta,\Delta)}\coth[\frac{\mu t}{\sin(\Theta)}\sqrt{1 + 2A(Q,\mu,\eta,\Delta)}]} d\Delta, \tag{2.45}$$

$$A(Q,\mu,\eta,\Delta) = \frac{Q}{\mu}\left[\frac{1}{\eta\sqrt{2\pi}}\exp(-\frac{\Delta^2}{2\eta^2})\right], \tag{2.46}$$

where η is the mosaic spread of the crystal, μ is the total linear attenuation factor of the crystal, and t is the crystal thickness [21]. The linear attenuation coefficient can be

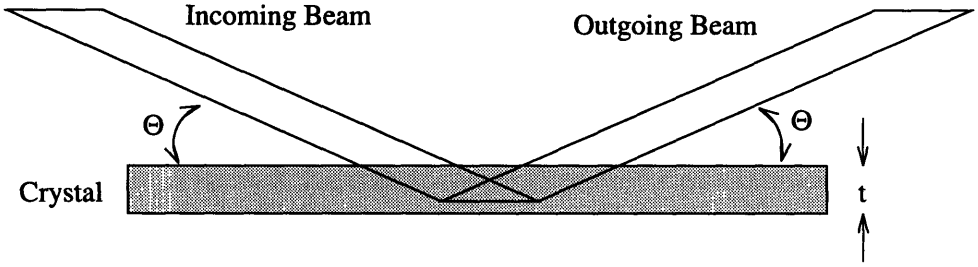

Figure 2-10: Monochromator Geometry

calculated from

$$\mu = (4\pi b^2 + \sigma_i + \sigma_a) N_c n, \tag{2.47}$$

where σ_i is the incoherent scattering cross section and σ_a is the absorption cross section.

By considering the first two monochromators, the differential intensity reaching the sample can be estimated:

$$\frac{\partial I}{\partial t} = \frac{\partial \Phi}{\partial \lambda} \frac{\lambda \cot(\Theta)}{4\pi} R \frac{\alpha_0 \alpha_1 \eta}{\sqrt{\alpha_0^2 + \alpha_1^2 + 4\eta^2}} \frac{\beta_0 \beta_1 \eta}{\sqrt{\beta_0^2 + \beta_1^2 + 4\sin^2(\Theta)\eta^2}} e^{-\mu \tau_{in}} \tag{2.48}$$

where $\frac{\partial \Phi}{\partial \lambda}$ was defined in equation 2.36 [41, page 211], μ is the total linear attenuation factor for the sample, as given in equation 2.47, and τ_{in} is the thickness of the sample traversed by the beam on its way to the region of interest.

Calculation of Intensity Measured at Detector

Equation 2.48 gives the intensity of neutrons at the center of the scattering volume. The intensity entering the detectors can be estimated by first examining the Debye-Scherrer equation for the intensity reflected by a set of planes in powder diffraction:

$$\frac{\partial I}{\partial t}\Big|_{diffracted} = \frac{\partial I}{\partial t} \frac{1}{2} m F^2 N_c^2 V \lambda^2 d_0, \tag{2.49}$$

where F^2 is the structure factor for the sample, N_c is the unit cell density, V is the volume of the sample defined by the collimators, and m is the multiplicity of the set of planes. The structure factor for the sample is calculated identically to that of the monochromator, including the e^-W term, except that the sample material is considered instead of the monochromator material. The multiplicity for a given family of planes is the number of planes contained in that family. For example, in a cubic material, the $\{100\}$ planes have a multiplicity of 6, since

$$\{100\} = (100), (010), (001), (\bar{1}00), (0\bar{1}0), (00\bar{1}).$$

The following boolean expression is useful for determining the multiplicity of a family of planes in a cubic material with indices $\{hkl\}$:

$$m = 48\{2^{[(h=k)+(k=l)+(k=0)+(l=0)]+2(h=0)}\}^{-1}. \tag{2.50}$$

Since powder diffraction from a given family of planes scatters neutrons into a cone, the intensity diffracted is really solid angle flux. The intensity reaching the detectors is then just a function of the attenuation in the beam leaving the sample, and the loss in intensity due to collimation. The attenuation in the beam leaving the sample is simply $\exp(-\mu\tau_{out})$ The detectors are assumed to be in an array, located at several angles ϕ, separated by an angle $d\phi$, and evenly spaced along θ, separated by an angle $\delta\theta$. Each detector is assumed to have a collimation of α_2 in the scattering plane. The intensity per unit time reaching such a linear array of detectors is given by

$$\frac{\partial I}{\partial t}\Big|_{detectors} = \frac{\partial I}{\partial t}\Big|_{diffracted} \frac{\alpha_2}{\delta\theta}\frac{d\phi}{2\pi}e^{-\mu\tau_{out}} \tag{2.51}$$

where τ_{out} is the thickness of the sample traversed by neutrons scattering from the region of interest towards the detectors.

Finally, taking into account the duration of the experiment (t), and the efficiency of the detectors (η_d), the intensity for a peak can be evaluated:

$$I_{detected} = \frac{\partial I}{\partial t}\Big|_{detectors}\, \eta_d t \tag{2.52}$$

Incoherent Background

The incoherent background reaching each detector is given simply by

$$I_{incoherent} = \frac{\partial I}{\partial t}\sigma_i N_c n \frac{A_1 V}{A_s}\frac{\alpha_2 d\phi}{2\pi} e^{-\mu\tau_{out}}\eta_d t \tag{2.53}$$

where A_1 is the cross sectional area of the collimator between the monochromator and the sample, $\frac{\partial I}{\partial t}$ is given in equation 2.48, and A_s is the area of the beam at the sample volume;

$$A_s = (w_\alpha + d_{in}\sqrt{2\pi}\sigma_\Theta)(w_\beta + d_{in}\sqrt{2\pi}\sigma_\Theta), \tag{2.54}$$

where w_α is the width of the collimator in the scattering plane, w_β is the width of the collimator perpendicular to the scattering plane, and d_{in} is the distance from the end of the collimators to the region of interest.

The effect of the incoherent background on the value of L is to replace the I^{-1} term in equation 2.21 with

$$\frac{I + 7.5 I_{incoherent}}{I^2}, \tag{2.55}$$

which increases the value of L, increasing overall uncertainty.

2.2.3 Strain Determination by Time-of-Flight

Residual stress determination with the time-of-flight (TOF) method is similar to the determination with a monochromatic beam, except that a "white," beam containing many different wavelengths is employed. A beam chopper and TOF detector are is used so that the flight time of a neutron from the source to the detector can be determined. In the case of a pulsed source, the chopper may also do some wavelength selection of neutrons, as longer wavelength neutrons tend to emerge from pulsed source moderators at later times.

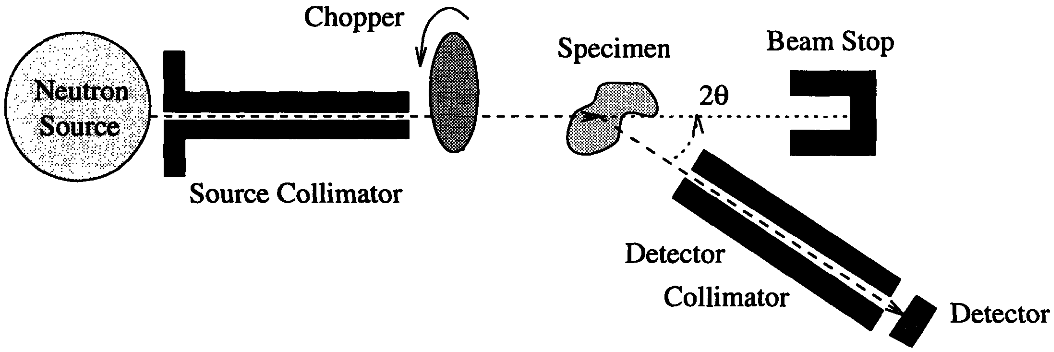

Figure 2-11: Diffraction by Time-of-Flight Measurement

A basic setup for TOF measurements is shown in figure 2-11 The illustration shows the detectors at a single fixed angle; however, there are position sensitive TOF detectors capable of detecting at several angles simultaneously [34, 28].

As was mentioned in the introduction, neutron diffraction by the TOF method relies on the DeBroglie definition of the wavelength of a neutron: $\lambda = \frac{\mathbf{h}}{p}$, where h is Planck's constant and p is the neutron's momentum. Since thermal neutrons are non-relativistic, $p = mv$, where m is the neutron mass and v is the neutron velocity. If the path between the chopper and the detector is a well defined distance s, then $v = \frac{s}{t}$, where t is the travel time of the neutron. Combining equations gives $\lambda = \frac{\mathbf{h}}{ms}t$. In pulsed sources, where longer wavelength neutrons emerge at later times, t may be replaced by $(t - f(\lambda))$; a first order approximation would be to assume that $f(\lambda)$ is equal to $C_0\lambda + t_0$, where C_0 is a constant. Combining everything, a simple relation emerges,

$$\lambda = \frac{t - t0}{C} \quad C = \frac{ms}{h} + C_0. \tag{2.56}$$

In a steady-state source, the C_0 term would simply be zero.

For each detector at an angle θ_d, neutrons diffracting from several planes are detected, each plane having its characteristic spacing d_0. For each value of d_0, one would expect peaks in the detected λ values near λ_{peak}, where $\lambda_{peak} = 2d_0 \sin(\theta_d)$.

As with the monochromator case, σ_{d0} is assumed to be zero. In the TOF case, σ_θ can be calculated by assuming that the sample acts as a monochromator with a very large mosaic spread, taking the limit of equation 2.25 as η approaches infinity (compared to the α's) we find:

$$\sigma_\theta^2 = \frac{1}{4}(\alpha_0^2 + \alpha_1^2), \tag{2.57}$$

where α_0 is a measure of the collimation between the source and the sample, and α_1 is a measure of the collimation between the sample and the detector.

The derivation of the value σ_λ will be discussed later, in the section on detected intensity. It is dependent on the uncertainty in θ, and the uncertainty in the time width of a pulse at a particular wavelength:

$$\sigma_\lambda = \sqrt{\sigma_\lambda(\theta)^2 + \frac{\sigma_t^2}{C^2}}, \qquad \sigma_\lambda(\theta) = \lambda \cot(\theta)\sigma_\theta, \tag{2.58}$$

where C is given in equation 2.56. The uncertainty in the time width of a pulse is a somewhat complicated function of the width of the pulse coming out of the chopper combined with the moderation time and flight time of the neutrons. It can be approximated by:

$$\sigma_t \approx \begin{cases} \frac{\delta_t}{\sqrt{2\pi}} & \text{for} \lambda \leq \lambda_c \\ (\frac{\lambda_c}{\lambda})^2 \frac{\delta_t}{\sqrt{2\pi}} & \text{for} \lambda > \lambda_c \end{cases} \tag{2.59}$$

where δ_t is the full width at half maximum (FWHM) of the pulse from the chopper, and λ_c in an empirical value, best fit to the actual spectrum of neutrons.

Using equations 2.57 and 2.59 Equation 2.21 can be simplified to:

$$L_i = 64[\sin^4(\theta) C^2 \frac{\sigma_t^2}{\lambda^2} + 32 \sin^2(2\theta_i)(\sigma_\Theta^2 + \sigma\theta_i^2)] I_i^{-1}, \tag{2.60}$$

where σ_t, like the other σ's, is equal to $\sigma_t/\sqrt{I}$. If instantaneous pulses are assumed ($\sigma_t \approx 0$),

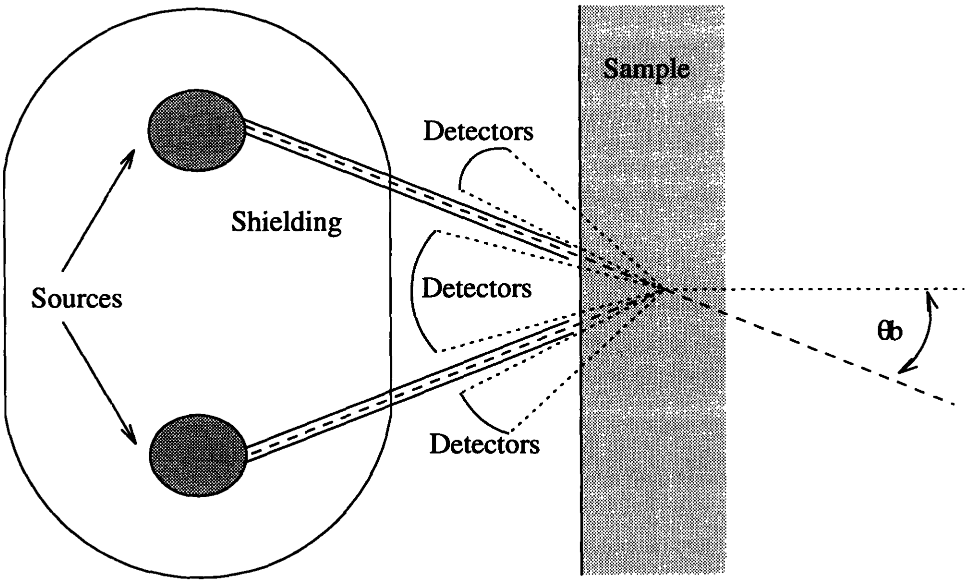

Figure 2-12: Geometry for Time of Flight Backscattering

then

$$L_i = [32 \sin^2(2\theta_i)(\sigma\theta_i^2)]^{-1}. \tag{2.61}$$

Time of Flight Backscattering Geometry

With the assumption of very short pulses, equation 2.61 indicates that backscattering may be an option worth considering in the TOF scenario. Figure 2-12 illustrates a cross section of a possible setup for performing strain measurements with TOF backscattering. The source needs to be distributed in this case, as the neutrons must travel in straight lines from the source(s) to the sample. Several such sources are arranged in a toroid, each with a collimator pointing towards the sample volume. For each combination of wavelength and plane spacing that causes a backscattering cone with $\frac{\pi}{2} - 2\theta < \theta b$, there will be a pattern of neutrons on the detectors like the one shown in figure 2-6, with a distribution per unit ϕ_b like the one shown in figure 2-7.

In this scenario, a given detecting element at ϕ_b and r_d on the detector (see Figure 2-5) should detect peaks in the wavelength distribution whenever

$$\lambda = 2d_0 \sin(\frac{1}{2}(\theta_b - \tan^{-1}(\frac{r_d min}{Z}))) \tag{2.62}$$

for the inner detector or whenever

$$\lambda = 2d_0 \sin(\frac{1}{2}(\tan^{-1}(\frac{r_d max}{Z}) - \theta_b)) \tag{2.63}$$

for the outer detector. Once again, Z is the distance from the detectors to the sampled volume, and d_0 is the plane spacing for a given plane.

The major disadvantage of this technique is the need for a distributed source, so an alternate configuration to figure 2-12 was considered, using a central source and bent neutron guide tubes employing total external reflection. Total external reflection occurs on a material when a neutron strikes the surface of the material at an angle less than the critical angle, $\theta_c = \lambda\gamma_c$, where $\gamma_c = \sqrt{Nb/\pi}$, N is the atomic number density of the material, and b is the average bound coherent scattering length of the material. Typical values of γ_c range from 1.53 mrad $\AA^{-1}$ on silicon-nickel interfaces to 1.1 mrad $\AA^{-1}$ on lead-silica glass capillary guide tubes[15, page 8]. Assuming a round guide tube, if R_c is the radius of curvature of the guide tube, then the radius of the guide tube itself, r_g given by:

$$r_g = R_c \frac{1 - \cos(\theta_c)}{1 + \cos(\theta_c)}. \tag{2.64}$$

Assuming lead-silica glass capillaries with a radius of curvature of 1 meter, and a minimum wavelength of $3\AA$, the guide tube radius would have to be 3 microns, identical to the polycapillary tubes investigated at NIST. These tubes were shown to have a transmission, T, given by $T = R^{L(\lambda\gamma_c/2r_g)}$, where R is the reflectivity of the material, 0.993 ± 0.001 [15, page 8]. Using these values and an estimated travel distance of 3 meters, the transmission should be 10^{-5}, too low a value to be useful, especially considering that the acceptance angle of the capillaries is only 3.3 mrad.

Intensity from Time of Flight Measurements

In many respects, calculation of intensity when considering neutron diffraction by time of flight is very similar to the calculation in the monochromatic case. However, there are several ways in which the calculations are different. In the TOF case, modeling and characterization of the source neutrons must take into consideration the dependence of flux on both wavelength and time; a chopper must be modeled instead of a monochromator, and only two sets collimators must be considered.

Time and Wavelength Dependent Source Characterization

Carpenter and Yelon [40, page 187] go into great depth describing the time and wavelength dependent intensity functions ($i(\lambda, t)$) for pulsed neutron sources. At the low energies considered for neutron diffraction, they describe three semi-empirical formulas which can be used to describe the $i(\lambda, t)$ function at a given distance from the source. All three of the formulas describe the distribution as the sum of a slowing down term and a storage term. The slowing down term accounts for the neutrons that downscatter from higher energies, while the Maxwellian-like storage term accounts for neutrons that have reached thermal equilibrium, but have not yet escaped from the moderator.

Since these formulas are both approximate and empirical; and too complex to be manipulated mathematically, they will not be discussed further. A suitable function for $i(\lambda, t)$ could be interpolated from a lookup table constructed from experimental or simulated data.

Figure 2-13 shows the $\frac{\partial^2 \Phi}{\partial \lambda \partial t}$ distribution (per high-energy neutron from the source) for a 6 cm radius CH_4 moderator at $4\,K$, sampled 2 cm from the high-energy source, as modeled by a monte-carlo simulation. As can be seen on the graph, high energy neutrons appear at a high flux for the duration of the source pulse (6 μsec); after the end of the pulse, they quickly disappear. The differential flux of lower energy neutrons ($\approx 3\mathring{A}$) does not reach a maximum until about 30 μsec after the source pulse starts.

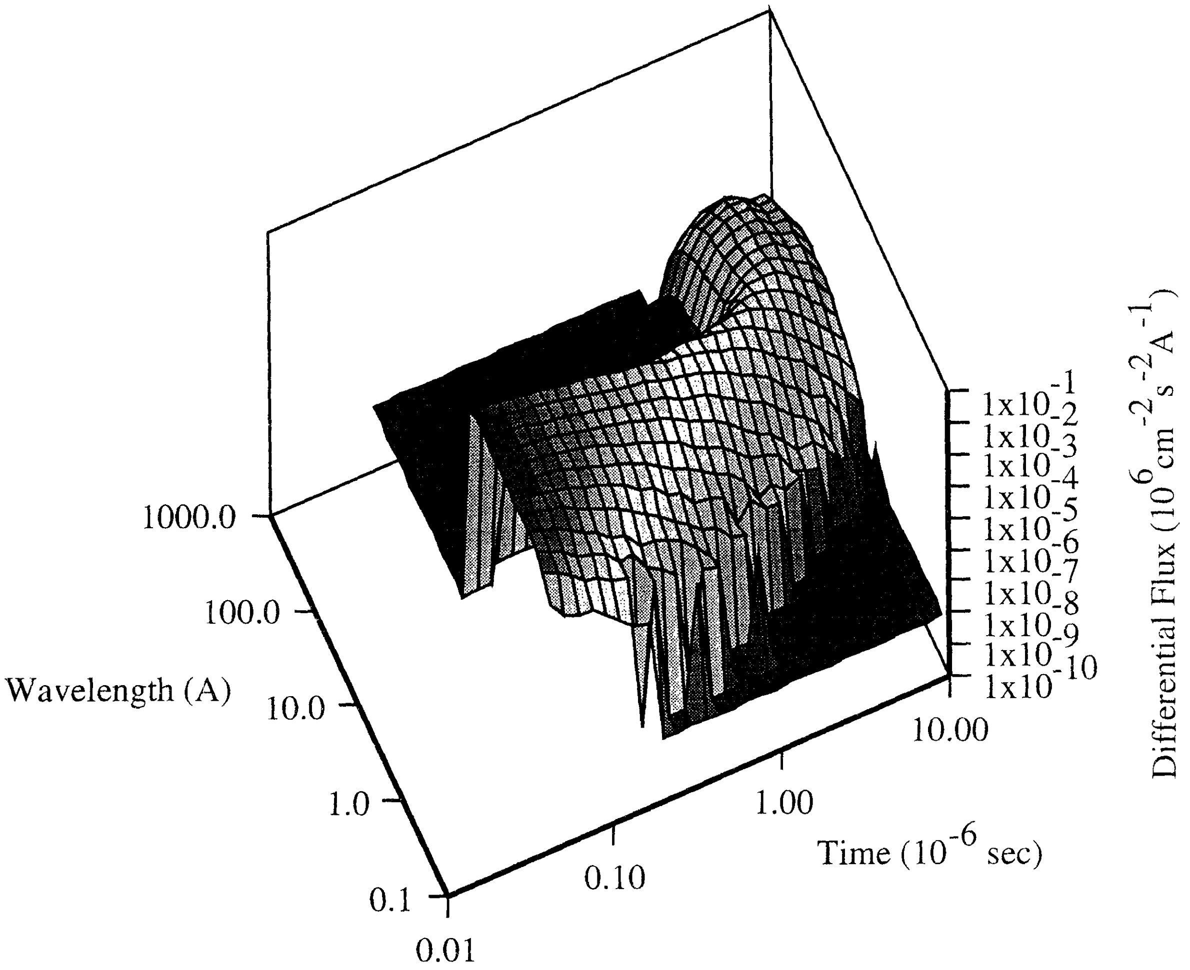

Figure 2-13: $i(\lambda, t)$ distribution from a CH_4 source.

Time dependent changes to Intensity

In the process of traveling from the source, through the sample, and into the detector, the neutrons travel a path length of L_p. The effect on figure 2-13 is to shift the low wavelength neutrons slightly up in time, while shifting the long wavelength neutrons greatly up in time. The time and wavelength dependent differential flux at the source ($\frac{\partial^2}{\partial\lambda\,\partial t}\Phi(\lambda,t)$) becomes $\frac{\partial^2}{\partial\lambda\,\partial t}\Phi(\lambda, t-\frac{Lp}{v(\lambda)})$ at the detector, where $v(\lambda)=\frac{\mathrm{h}^2}{m_n\lambda}$.

It is assumed that the time width of the low energy neutrons pulses is too wide, and their flight path too short to be useful without "chopping" the beam. Chopping refers to the process of letting just a small burst of neutrons through a rapidly spinning absorber; the time width of the burst is dependent on the rotational speed, radius, and slit width of the chopper. The effect of the chopper on the spectrum is modeled as a normal distribution about t_0, with a width of σ_{t0}, applied to the distribution at a distance L_c from the source. The combined effect on differential flux from the flight path and the chopping is:

$$\left.\frac{\partial^2}{\partial\lambda\,\partial t}\Phi(\lambda,t)\right|_{timeshifted} = \frac{\partial^2}{\partial\lambda\,\partial t}\Phi\left[\lambda, t-\frac{Lp}{v(\lambda)}\right]\exp\left\{-\frac{\left[t-\frac{L_p-L_c}{v(\lambda)}-t_0\right]^2}{2\sigma_{t0}^2}\right\}, \quad v(\lambda)=\frac{\mathrm{h}}{\mathrm{m}\lambda}. \tag{2.65}$$

It is assumed that after the chopping, the time and wavelength dependent differential flux can be modeled as a simple product of normal distributions:

$$\left.\frac{\partial^2}{\partial\lambda\,\partial t}\Phi(\lambda,t)\right|_{timeshifted} = \Phi_0\frac{1}{\sqrt{2\pi}\sigma_\Lambda}\exp\left[-\frac{(\lambda-\Lambda)^2}{2\sigma_\Lambda}\right]\exp\left[-\frac{(t-t_0(\lambda))^2}{2\sigma_t(\lambda)}\right]; \tag{2.66}$$

where Φ_0 represents equation 2.65 integrated over all wavelengths and time; Λ_0 and σ_Λ represent the mean value and width of a wavelength dependent peak intensity function; $t_0(\lambda)$ is $C\lambda+t_0$, from equation 2.56; and $\sigma_t(\lambda)$ is the same as σ_t in equation 2.59.

Time-Independent Changes to intensity

In a manner analogous to the monochromatic case, the differential flux at the sample volume is determined. Assuming a single collimator with angular divergence α_0 along $\phi=0$ and

β_0 along $\phi = \frac{\pi}{2}$, the source flux is decreased by a factor of $\frac{\alpha_0\beta_0}{4\pi}$. Assuming that they travel a distance τ_{in} through the sample before reaching the region of interest, they will be attenuated by the factor $\exp(-\mu\tau_{in})$, where μ is the total linear attenuation factor for the sample, as given in equation 2.47. Thus, the differential intensity at the sample is

$$\frac{\partial^3}{\partial\lambda\,\partial^2 t}I(\lambda,t) = \frac{\partial^2}{\partial\lambda\,\partial t}\Phi(\lambda,t)\frac{\alpha_0\beta_0}{4\pi}e^{-\mu\tau_{in}}. \tag{2.67}$$

In [9], Buras describes a method of determining the diffracted intensity given a wavelength dependent intensity function $\frac{\partial I}{\partial\lambda}$, assuming that uncertainty due to time is negligible. This analysis can be easily extended, to include the effects of time uncertainty. It starts with the Debye-Scherrer equation for the intensity reflected by a set of planes in powder diffraction:

$$\left.\frac{\partial^3}{\partial\lambda\,\partial^2 t}I(\lambda,t)\right|_{diffracted} = \frac{\partial^3}{\partial\lambda\,\partial^2 t}I(\lambda,t)mF^2N_c^2V\frac{\lambda^3}{4\sin(\theta)}. \tag{2.68}$$

Assuming that $\frac{\partial^3}{\partial\lambda\,\partial^2 t}I(\lambda,t)$ is of the form given in equation 2.66, then for a given value of θ, a plot the differential intensity times λ^3 vs time and wavelength would resemble the contour plot shown in figure 2-14. At several values of d_0, the value of λ will equal $2d_0\sin(\theta)$. Six such values of λ $(\lambda_1, \lambda_2, ..., \lambda_6)$ are shown on figure 2-14. At each value of λ_n, neutrons will diffract from the $\lambda^3\frac{\partial^3}{\partial\lambda\,\partial^2 t}I(\lambda,t)$ distribution. In addition, neutrons with wavelengths near λ_n will also tend to diffract with a probability given by

$$p(\lambda)_{diff} = \exp\left[-\frac{(\lambda-\lambda_n)^2}{2\sigma_\lambda(\theta)^2}\right], \tag{2.69}$$

where $\sigma_\lambda(\theta)$ is simply $2d\cos(\theta)\sigma_\theta$; σ_θ is given in equation 2.57.

The intensity per unit time diffracted for a given θ and d_0 is the same as the integral under one of the small peaks on figure 2-14. This integral is

$$\frac{\partial I}{\partial t} = \int_{-\infty}^{\infty}\int_{-\infty}^{\infty} p(\lambda)\lambda^3\frac{\partial^3}{\partial\lambda\,\partial^2 t}I(\lambda,t)_{diffracted}\,d\lambda\,d\theta. \tag{2.70}$$

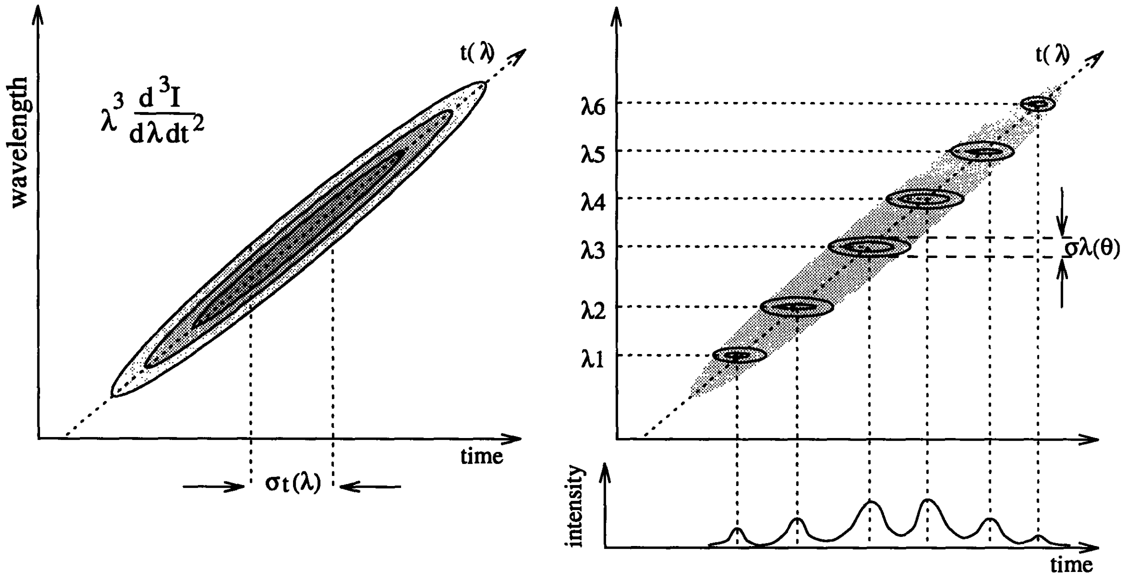

Figure 2-14: Derivation of intensity vs. time

Assuming that $\sigma_t(\lambda)$ varies slowly with respect to λ, the integral can be evaluated:

$$\frac{\partial I}{\partial t} = mF^2N_c^2V\frac{\lambda_n^3}{4\sin(\theta)}2\pi\sigma_t(\lambda_n)\sigma_\lambda(\theta)\frac{\Phi_0\Sigma}{\sqrt{\sigma\lambda^2+\Sigma^2}}\exp(-\frac{(\Lambda-\lambda_n)^2}{2(\sigma_\lambda^2+\Sigma^2)})f[\Sigma,\Lambda,\lambda_n,\sigma_\lambda(\theta)],$$

$$f(\Sigma,\Lambda,\lambda_n,\sigma_{lambda}) = \begin{bmatrix} \Sigma^6\lambda_n^3 + 3\sigma_\lambda^2\Lambda\Sigma^4\lambda_n^2 + \\ 3\sigma_\lambda^2\Sigma^2(\Sigma^4+(\Sigma^2+\Lambda^2)\sigma_\lambda^2)\lambda_n + \\ \sigma_\lambda^4\Lambda(3\Sigma^4+(3\Sigma^2+\Lambda^2)\sigma_\lambda^2) \end{bmatrix} \lambda_n^{-3}(\sigma\lambda^2+\Sigma^2)^{-3}, \qquad (2.71)$$

$$f(\Sigma,\Lambda,\lambda_n,\sigma_{lambda}) \approx 1.$$

From this result, and the assumption that $\sigma_\lambda \ll \Sigma$, it can be seen that λ^3 term in equation 2.68 and the left hand side of equation 2.66 pass through the integral unchanged, for the most part. Equation 2.70 can then be re-evaluated, assuming these terms to be constant; if the integration is only carried out with respect to λ, a function of intensity vs time is obtained:

$$\frac{\partial I(t)}{\partial t} = Constants \frac{1}{\sqrt{C^2\sigma_\lambda(\theta)^2 + \sigma_t(\lambda_n)^2}} \exp\left\{ -\frac{[t-(C\lambda_n + t0)]^2}{2[C^2\sigma_\lambda(\theta)^2 + \sigma_t(\lambda_n)^2]} \right\}, \qquad (2.72)$$

which is a gaussian distribution with mean $C\lambda_n + t0$ and width $\sqrt{C^2\sigma_\lambda(\theta)^2 + \sigma_t(\lambda_n)^2}$. If the values of and wavelength are switched with equation 2.56, then the value given for σ_t in section 2.2.3 is obtained:

$$\sigma_\lambda = \frac{\sqrt{C^2\sigma_\lambda(\theta)^2 + \sigma_t(\lambda_n)^2}}{C} = \sqrt{\lambda^2 \cot^2(\theta)\sigma_\theta^2 + \frac{\sigma_t^2}{C^2}} \qquad (2.73)$$

Equation 2.71 gives the intensity per unit time scattered by the sample volume. The fraction of this intensity reaching a detector of width $d\phi$ is $\frac{d\phi}{2\pi}\exp(-\mu\tau_{out})$, where μ is the total attenuation of the sample material, and τ_{out} is the thickness of material traversed by the beam on its way out of the specimen. Thus, after a period of time (t), the intensity detected will be

$$I = \frac{\partial I}{\partial t}\frac{d\phi}{2\pi}\partial t e^{-\mu\tau_{out}}\eta_d t \qquad (2.74)$$

where η_d is the detector efficiency.

Incoherent Background

The incoherent background reaching each detector is given simply by

$$I_{incoherent} = \frac{\partial I}{\partial t}\sigma_i N_c n \frac{A_0 V}{A_s}\frac{d\phi}{2\pi} e^{-\mu\tau_{out}}\eta_d t \qquad (2.75)$$

where A_0 is the cross sectional area of the collimator between the source and the sample, $\frac{\partial I}{\partial t}$ is given in equation 2.67, and A_s is the area of the beam at the sample volume;

$$A_s = (w_\alpha + d_{in}\alpha_0)(w_\beta + d_{in}\beta_0), \qquad (2.76)$$

where w_α is the width of the collimator in the scattering plane, w_β is the width of the collimator perpendicular to the scattering plane, and d_{in} is the distance from the end of the collimators to the region of interest.

The effect of the incoherent background on the value of L is to replace the I^{-1} term in equation 2.21 with

$$\frac{I + 7.5 I_{incoherent}}{I^2}, \tag{2.77}$$

which increases the value of L, increasing overall uncertainty.

2.2.4 Evaluation of Least Squares Determination of Strain Components

If a few assumptions are made, the uncertainty in strain components can be divided into two independent quantities; the uncertainty in angle, and the uncertainty due to the number of angle and azmuthal angle measurements. For a given scattering experiment, assuming that the intensity measurements (I) are relatively constant at all locations of θ and ϕ; and assuming that perfect monochromization or perfect chopping occurs, then L will be defined by either equation 2.31 or equation 2.61. Generalizing these equations results in

$$\mathbf{L}_i = 32K^{-1}\sin^2(2\theta_i)\sigma\theta_i^2, \tag{2.78}$$

where K is a constant representing either the average intensity in the TOF case, or double the average intensity in the monochromatic case.

To simplify matters further, the uncertainty of each strain component will not be considered; only the uncertainty of the sum of the strain components will be considered. This quantity, σ_s, is given by the square root of the trace of the matrix C:

$$\sigma_s^2 = \mathrm{trace}(\mathbf{C}^{-1}),$$

or

$$\sigma_s^2 = \mathrm{trace}\left\{\left[\sum_i \frac{A_i^T A_i}{32\sin^2(2\theta_i)}\right]^{-1}\right\}\sigma_\theta^2 \tag{2.79}$$

Now, assuming that uncertainty in θ is relatively constant, σ_s can be estimated from the number of values of θ and ϕ alone. A simple analysis was performed, to see how the value of $(\sigma_s/\sigma_\theta)^2$ varies with the number of sampled points.

It was assumed that detectors were placed in an array, with n_θ values of θ measured and and n_ϕ values of ϕ measured, resulting in $N = n_\theta n_\phi$ measurement points. As N approaches infinity, one would expect that the overall uncertainty value would approximate:

$$(\sigma_s/\sigma_\theta)^2 \approx \text{trace}\left\{\left[N\int_{\theta_{min}}^{\theta_{max}}\int_{\phi_{min}}^{\phi_{max}} \frac{A(\phi,\theta)^T A(\phi,\theta)}{32\sin^2(2\theta_i)} d\phi\, d\theta\right]^{-1}\right\}, \tag{2.80}$$

where

$$A(\phi,\theta) = 2\left[\begin{array}{cccccc} x(\phi,\theta)^2 & y(\phi,\theta)^2 & z(\theta)^2 & x(\phi,\theta)y(\phi,\theta) & y(\phi,\theta)z(\theta) & z(\theta)x(\phi,\theta) \end{array}\right]. \tag{2.81}$$

Now, to evaluate this equation, some geometrical assumptions concerning the range of θ and ϕ are required. The geometry shown in figure 2-15 was assumed to apply in this case, resulting in the following assumptions about the measurable ranges:

$$\begin{aligned} \theta_{min} &= \tfrac{\pi}{8}, & \theta_{max} &= \tfrac{3\pi}{8}, \\ \phi_{min} &= \tfrac{\pi}{2}, & \phi_{max} &= \tfrac{3\pi}{2}. \end{aligned} \tag{2.82}$$

Using these assumptions, we get

$$(\sigma_s/\sigma_\theta)^2 \approx \frac{1396.5}{NK} = \frac{1396.5}{n_\phi n_\theta K}. \tag{2.83}$$

However, this equation should only apply to very large values of N. To evaluate the behavior of equation 2.79 for small values of N, a computer simulation was performed. Equation 2.79 was evaluated using $n_\phi = [3\ ,4,5,10,20,50,\ 100]$, and $n_\theta = [2,\ 3,4,5,10,20,50,\ 100]$[3]. For each set of n_ϕ and n_θ values, sets of ϕ_i $(i = 1..n_\phi)$ and θ_j $(j = 1..n_\theta)$ were randomly

---

[3] Equation 2.79 approaches infinity for $n_\phi \leq 2$ or $n_\theta \leq 1$

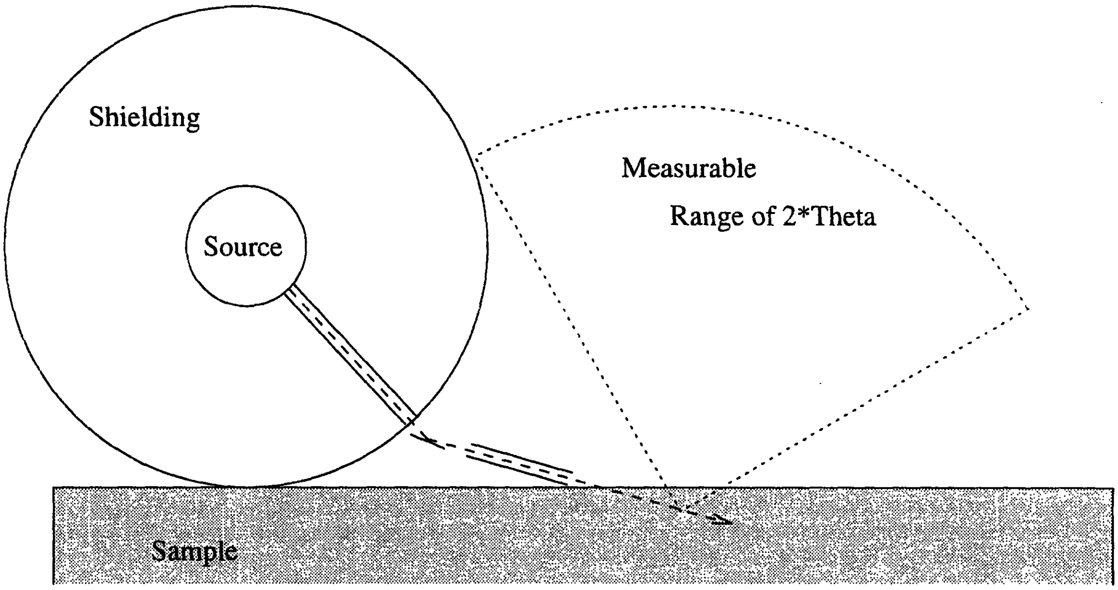

Figure 2-15: Basic Scattering Geometry

selected within the ranges specified in equation 2.82 [4]. Equation 2.79 was then evaluated, and re-evaluated several times using new random sets of ϕ_i and θ_j values. After several evaluations, the minimum value of $(\sigma_s/\sigma_\theta)^2$ for each set of n_ϕ and n_θ was selected. These values are shown in table 2.2. At low values of N, the data did not fit the expected relationship given in equation 2.83; it fit the following equation much better:

$$(\sigma_s/\sigma_\theta)^2 \approx \frac{1453}{(n_\phi - 2)^{0.86} n_\theta K}. \tag{2.84}$$

Now, equation 2.84 can be evaluated, to see what the optimum values of n_ϕ and n_θ are for a given set of N detectors. If $n_\theta = N/n_\phi$ is substituted into equation 2.84, and the equation minimized, one finds the surprising results:

$$n_\phi = 14, \quad n_\theta = \frac{N}{14}. \tag{2.85}$$

---

[4] Evenly spaces values of ϕ_i and θ_j tended to yield larger values of $(\sigma_s/\sigma_\theta)^2$

Table 2.2: Values of $(\sigma_s/\sigma_\theta)^2K$ for given n_ϕ and n_θ values.

		$n_\theta =$							
		2	3	4	5	10	20	50	100
$n_\phi =$	3	721	467	356	300	144	88.1	36.9	20.9
	4	320	212	137	132	78.0	35.6	20.0	9.25
	5	256	156	110	109	53.6	26.8	10.0	7.52
	10	126	83,2	64.1	49.0	25.5	13.2	5.51	2.71
	20	56.9	40.4	28.6	26.0	12.4	6.71	2.85	1.42
	50	23.8	18.1	12.7	10.3	5.31	2.56	1.20	0.60
	100	12.5	8.07	6.81	5.67	2.63	1.46	0.60	0.31

What this means is that if one is limited to using N detectors to cover an array of ϕ and θ values, they should be divided up such that a number close to 14 of them cover ϕ values, and a number close to $N/14$ of them cover θ values. For example, if one wished to place 36 detectors in array, the most effective combination would be to measure 12 (close to 14) values of ϕ and 3 values of θ.

2.3 Chapter Summary

In this chapter, a method for determining three-dimensional internal stresses with neutron diffraction is presented. Also, a set of equations for evaluating the accuracy of the method were explained. Given the description of a neutron diffraction system, these equations should predict how accurately the system can determine residual stresses in a given period of time. The next few chapters will concentrate on how various parts of a diffraction system can be optimized; the equations in this chapter can then be used to evaluate the entire system.

Chapter 3

Neutron Sources

3.1 introduction

This chapter addresses the supply of neutrons to the diffraction system, first by examining possible neutron sources, then by examining ways of moderating these neutrons down to usable energies. The shielding of these neutrons is examined next, followed by the handling of the neutrons.

3.2 High Energy Neutron Sources

While there are perhaps hundreds of reactions which can create neutrons, they can be summed up into a few categories. The reaction used most often today is fission in a nuclear reactor, which occurs when a neutron is captured by a nucleus which splits into several fragments, including more neutrons. Some of these neutrons leak out of the reactor, and can be used for diffraction, while others are required to keep the chain reaction going. In some cases, such as Cf-252 sources, the fission is spontaneous, and does not require neutrons. A similar reaction is spallation, when an ion is accelerated up to high velocity, and slammed into a large nucleus. The nucleus goes into a very excited state from which it de-excites by "boiling" off neutrons and other particles. Another common reaction involves the absorption of a light particle (proton, deuteron, or alpha particle) by a light nucleus such as lithium or beryllium, resulting in the emission of a neutron. Similarly, two very light nuclei (deuterons and/or tritons) can fuse, resulting in the emission of neutrons.

A desirable characteristics in a neutron source for diffraction is a large flux with some directionality. The large flux is required because the neutrons are usually collimated down to thin beams of low angular spread. Additionally, the cross section for diffraction is typically quite small, requiring a large number of neutrons to resolve a diffraction peak. If some directionality is evident in the thermal neutron spectrum, then neutrons can be sampled along that preferred direction, increasing the flux in the sampled beam.

Another desirable characteristic in a neutron source is low initial neutron energy. This reduces the amount of moderation required and the biological shielding, reducing the size and weight of the neutron-producing assembly. The ideal source would supply epithermal, or even thermal neutrons, as very little moderation would be required.

Current sources of neutrons for residual stress determinations are nuclear reactors and spallation devices. Typically, the reactor sources are quite large, and require extensive safety systems to prevent the release of their radioactive inventory. Additionally, nuclear reactors are not very acceptable in our culture due to their perceived risk, and the unacceptability of their waste. The spallation sources require long accelerators, and megawatts of energy to keep them running. However, these sources are capable of supplying thermal neutron fluxes of up to $10^{15} n/cm^2 sec$. Nevertheless, these neutron sources will not be examined further in this analysis.

Radioisotopes are a simple way of producing neutrons; generally, they just require a biological shield and moderator. However, they might not be acceptable in many places in our society because they are inherently radioactive, and therefore unacceptable. Thus, radioisotopes will not not be explored further.

3.2.1 Accelerator Sources of Neurons

Commonly available neutron sources involving MeV order reactions of deuterons or protons and light nuclei are not used for residual stress determinations because of their low flux. However, they should be capable of performing these measurements, although slowly. De-

Table 3.1: Reactions Commonly used with Accelerator Neutron Production

$${}^{2}_{1}\mathrm{D}+{}^{2}_{1}\mathrm{D}\rightarrow{}^{3}_{2}\mathrm{He}+{}^{1}_{0}\mathrm{n}+3.28\ \mathrm{Mev}$$

$${}^{3}_{1}\mathrm{T}+{}^{2}_{1}\mathrm{D}\rightarrow{}^{4}_{2}\mathrm{He}+{}^{1}_{0}\mathrm{n}+17.6\ \mathrm{Mev}$$

$${}^{9}_{4}\mathrm{Be}+\gamma\rightarrow 2{}^{4}_{2}\mathrm{He}+{}^{1}_{0}\mathrm{n}-1.67\ \mathrm{Mev}$$

$${}^{9}_{4}\mathrm{Be}+{}^{1}_{1}\mathrm{H}\rightarrow{}^{9}_{5}\mathrm{B}+{}^{1}_{0}\mathrm{n}+1.85\ \mathrm{Mev}$$

$${}^{9}_{4}\mathrm{Be}+{}^{2}_{1}\mathrm{D}\rightarrow{}^{10}_{5}\mathrm{B}+{}^{1}_{0}\mathrm{n}+4.35\ \mathrm{Mev}$$

$${}^{7}_{3}\mathrm{Li}+{}^{1}_{1}\mathrm{H}\rightarrow{}^{7}_{3}\mathrm{Li}+{}^{1}_{0}\mathrm{n}-1.64\ \mathrm{Mev}$$

$${}^{7}_{3}\mathrm{Li}+{}^{2}_{1}\mathrm{D}\rightarrow 2{}^{4}_{2}\mathrm{He}+{}^{1}_{0}\mathrm{n}+15.03\ \mathrm{Mev}$$

signers of these machines indicate that their flux could be increased greatly, to speed up resolving time. The reactions used in these devices can be summed up in table 3.1

Some of the reactions in table 3.1 are exothermic, so the ejected neutron has less energy than the incoming projectile. This can be an advantage, because it is easier to moderate lower energy neutrons; this leads to a smaller moderator and a higher flux for the same number of source neutrons.

One reaction that was noticed in 1954 by Bonner and Cook [47] was the creation of "slow" neutrons (Q=-420 kev) from the Be(d,n)B reaction. They found a large cross section for transitions to the 4.78 Mev excited state in ^{10}B when the deuterons have an energy of 920 kev. There does not seem to be any followup of this work, although the results are still used in references on ^{10}B energy levels [35].

To show the effect of source neutron energy on moderator output, three monte carlo simulations were performed; the first using neutrons of incident energy 14 Mev, the second using neutrons at 3 Mev, and the third using neutrons at 420 kev. In each case, 6 cm sphere of water surrounded by a beryllium reflector was modeled as the moderator, with a detector located in the moderator, at a distance of 2 cm from the source. The results show that the 4π thermal fluxes from the three sources, per source neutron are 0.004, 0.009, and 0.024 n/cm^2sec respectively.

In addition, a low energy source would require considerably less shielding. For a given sample volume, this means that the L/D ratio can be decreased, increasing the beam flux in that volume. Also, by requiring less shielding, the weight and cost of the assembly could be considerably reduced.

3.3 Characterization of 900 kev Deuterium on Beryllium Source

The $Be^9(d,n)B^{10}$ reaction is much more complicated than it appears. Two processes are at work in the reaction; stripping and compound nucleus formation. Also, the B^{10} can be left in the ground state, imparting 4.35 Mev of energy to the neutron; or the B^{10} can be left in one of its excited states. Finally, since the kinetic energy of deuteron is shared between the B^{10} atom and the neutron, the neutron energy is angularly dependent.

In the stripping process, the neutron is literally knocked out of the Be nucleus as the deuteron enters, resulting in an angularly dependent cross section. The cross section for stripping increases with increasing deuteron energy, although it is evident even at low energies [18].

In compound nucleus formation, the Be^9 and deuteron form an excited atom of B^{11}, which quickly decays to B^{10}, ejecting a neutron. The cross section for this reaction is independent of the angle of the emitted neutron.

The angular energy dependence of the ejected neutron can easily be computed with classical mechanics. In general, assuming that a projectile of energy E_p and mass M_p strikes a target of mass M_t at rest, ejecting a neutron of mass M_n and excess energy (Q), the energy of the neutron is given by

$$\begin{gathered} E_n(Q,\theta) = \left(\rho(\theta) + \sqrt{\rho(\theta)^2 + \omega(Q)}\right)^2, \text{ where} \\ \rho(\theta) = \frac{\sqrt{M_n M_p E_p}}{M_t + M_n}\cos(\theta), \quad \text{and} \quad \omega(Q) = \frac{M_t Q + E_p(M_t - M_p)}{M_t + M_n}. \end{gathered} \tag{3.1}$$

For a deuteron energy of 900 kev, possible excited states for the B^{10} are 0.72, 1.74, 2.15, and 3.59 Mev[1], corresponding to Q's of 3.64, 2.62, 2.21, and 0.78 Mev. For higher energy deuterons, excited states at 4.77, 5.15, and 6 Mev also become important. In any case, if the B^{10} is left in an excited state, the neutron will have less energy.

An attempt was made to characterize the angular and energy dependent cross section for the $Be^9(d,n)B^{10}$ reaction at low energies, interpolating from cross sections given in the literature. Unfortunately, for deuterons near 900 kev, there is very little data published on the angular and energy dependent cross section for neutron production. The nearest data that could be found was for 600 kev deuterons [45] and 1100 kev deuterons [18]. In both cases, the intent was to study the energy levels of B^{10}. Nevertheless, the data can be used to estimate the $Be^9(d,n)B^{10}$ cross section.

In [45], for 600 kev deuterons, the energy dependent neutron spectra was measured at 0°, 30°, 60°, 90°, 120°, and 150°. These spectra included peaks at each of the aforementioned Q values. The relative magnitude of each peak was measured and normalized, at each of the relative angular and Q dependent cross sections. Using data from [18], relative angular cross sections for deuterons at 1100 kev, 1540 kev, and 1950 kev were obtained. Using the four deuteron energy values, and a third order set of fitting functions, the normalized energy spectrum at 900 kev was deduced. This was then stretched to account for all angular values an renormalized. Finally, equation 3.1 was applied to determine the angular dependence of deuteron energy.

The normalized energy and angle dependent cross section and energy data was then converted into a source description for the MCNP code[2]. The procedure was then repeated, in case the accelerator is upgraded to supply 1.5 Mev neutrons. These source descriptions are listed in Appendix C, along with the worksheet used to obtain them.

---

[1] Some may argue that there is another excited state at 2.9 Mev, while others argue that there are two other excited states at 2.7 and 3.1 Mev [45]

[2] Monte Carlo Neutron-Photon Transport code from Los Alamos National Labs.

3.4 Moderation of Neutrons

The moderator design is an important aspect of the overall design of a source, as it dictates the form of the neutron spectrography, whether it is to be by time of flight or crystal diffraction. It also significantly affects the design of the shielding, and other parts of the system, such as the cooling system that would be required with a cold source.

The effort of this section is to design a set of optimum moderators, keeping open the possibility of either time-of flight measurements or monochromated neutron measurements. In either case, two temperature scenarios will be investigated, thermal (approximately 300 K), and cold (below 20 K). Many aspects of moderation will be investigated, to maximize the desired output of the beam while minimizing the undesirable output of fast neutrons.

3.4.1 Reflector Materials

One way to increase the flux in a small moderated region is to use a reflector. A reflector, as its name implies, reflects some of the escaping neutrons back into the moderator, increasing the average flux. A reflector may also increase the flux through reactions such as fission or $(n, 2n)$ reactions.

The effectiveness of a reflector for a deuterium-beryllium source is largely due to its scattering cross section in the 1–5 Mev range. These are the neutrons most likely to escape from the moderator without a single collision; therefore it is important that they be scattered back into the moderator so that they can be thermalized, and possibly enter the beam. Table 3.2 lists the approximate scattering cross section for several materials in the 1–5 Mev range. The number density of the materials is also given, so that a linear attenuation factor could be computed.

Materials selected from table 3.2 for further study included light water, heavy water, beryllium, boron, graphite, copper, chrome, nickel, tungsten, and lead. Platinum and Rhenium, which had very high probabilities of interaction per unit length were rejected due to their price.

Another desirable characteristic in a reflector is a large cross section for neutron mul-

Table 3.2: Materials with Large Mev-range Scattering Cross Sections

Element	Scattering Cross Section (barns)	Number Density (Atoms/$\mathring{A}^3$)	Linear Probability $(cm^{-}1)$
H_2O	2.6	0.03343	**0.09**
D_2O	1.9	0.03323	**0.06**
Be	2	0.1236	**0.25**
B	1.8	0.1281	**0.23**
C	2	0.0823	**0.16**
Na	1.4	0.02541	0.04
Al	2	0.06024	0.12
Si	3	0.04996	0.15
P	1.8	0.03539	0.06
S	2.5	0.03888	0.10
K	2.5	0.01325	0.03
Ca	2.6	0.02329	0.06
Ti	2.4	0.0567	0.14
V	2.7	0.07212	0.19
Cr	2.5	0.08328	**0.21**
Ni	2.3	0.0913	**0.21**
Cu	2.3	0.08493	**0.20**
Sr	4.0	0.01787	0.07
In	3.0	0.03834	0.12
I	3.8	0.0234	0.09
Ba	4.6	0.01535	0.07
Sm	5	0.02776	0.14
Ta	3.5	0.05525	0.19
W	3.5	0.06289	**0.22**
Re	4.5	0.06596	**0.30**
Pt	4	0.06622	**0.26**
Hg	4	0.04068	0.16
Pb	5	0.03296	0.16
Bi	5.6	0.02824	0.16

Table 3.3: Materials with Large $(n, 2n)$ Cross sections in the 1–5 Mev range.

Element	$(n, 2n)$ Cross Section (barns)	Number Density (Atoms/$\AA^3$)	Linear Probability $(cm^{-}1)$
Be	2	0.1236	**0.25**
In	1.4	0.03834	0.05
Cs	1.2	0.00861	0.01
Ce	1.3	0.02914	0.04
Ho	1	0.03199	0.03
Ta	1.3	0.05525	0.07
W	1.8	0.06289	**0.11**
Os	2	0.07124	0.14
Pt	1.7	0.06622	0.11
Pb	1.7	0.03296	0.06
Bi	2	0.02824	0.06
Th	2	0.03039	0.06

tiplying reactions such as the $(n, 2n)$ reaction or fission. Table 3.3 lists several materials, along with their approximate $(n, 2n)$ cross sections in the 1–5 Mev range. From this analysis, beryllium, tungsten, and lead were selected for study as reflectors due to their high probability of reaction per unit length, and due to their availability. Among fissionable materials, thermally-fissionable materials were not selected, in an attempt to avoid any handling of special nuclear materials. Among fast-fissionable materials, depleted uranium was selected due to its availability.

All the materials mentioned in the preceding paragraphs were evaluated with monte-carlo simulations. A 6 cm radius sphere of water with a 3 Mev neutron source as assumed in each case, with a 6 cm layer of the reflector surrounding the water moderator. It was assumed that the choice of moderator would not have a significant effect on the relative performance of different reflecting materials. The energy spectrums obtained by using each reflector were fit to the modified Maxwellian function given by equation 2.37. The results are shown in table 3.4

The results from table 3.4 clearly indicate that Beryllium is the best reflector for the Be(n, p)B source in this investigation. All calculations following the next section will assume

Table 3.4: Results from Reflector Evaluation

Reflector Material	Integrated Thermal flux n/cm^2sec
Boron	2.08 $\times 10^7$
Beryllium	**4.16** $\times 10^7$
Graphite	3.36 $\times 10^7$
Chrome	2.75 $\times 10^7$
Copper	3.16 $\times 10^7$
Heavy Water	2.82 $\times 10^7$
Light Water	**3.06** $\times 10^7$
Nickel	**3.60** $\times 10^7$
Lead	2.61 $\times 10^7$
Uranium-238	3.20 $\times 10^7$
Tungsten	3.28 $\times 10^7$

a beryllium reflector, unless otherwise noted.

In the case of the thermal moderator, it was noted that the Maxwellian portion of the spectrum always met the $1/\lambda$ portion of the spectrum at about 0.5 Å(0.33 ev), which defined for the rest of these evaluations, the breakpoint value between thermal and non-thermal neutrons. In the case of the cold source, the Maxwellian spectrum met the $1/\lambda$ at 2 Å(20 mev).

3.4.2 Time Effects of Reflected Moderator

One potential disadvantage of a reflected moderator is that the time width of moderated neutron pulses is increased. This can be a problem if one wishes to take advantage of the naturally short pulses from a cold CH_4 source. A pair of monte-carlo simulations were carried out to see how the pulse widths are affected. Each simulation assumed a 6 cm radius sphere of CH_4, with a source of 3 Mev neutrons at the center. One simulation assumed that a 6 cm thick beryllium reflector surrounded the moderator, while the other simulation assumed no such moderator. Time and wavelength dependent spectra were recorded, and the time width at 10% intensity for each wavelength was measured from the data. The results are shown in figure 3-1. The accelerator pulse width was assumed to be 50 μsec;

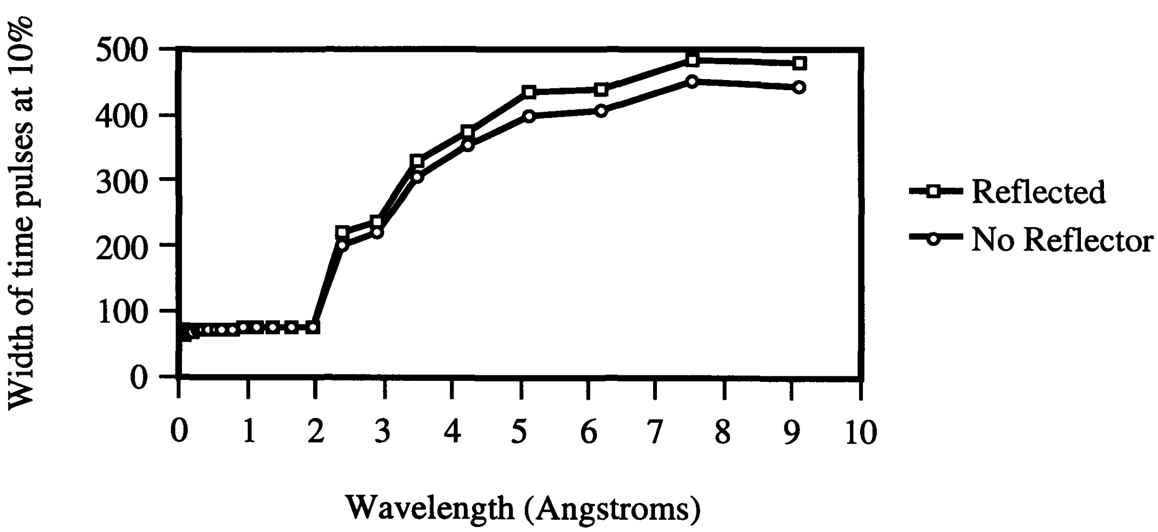

Figure 3-1: Full width at 10% of time distribution of neutrons from a CH_4 source.

that accounts for the minimum value of the time width at about 60 μsec. From this data, one might assume that the non-reflected situation is better, since the time width is less. However, it is important to recall that the uncertainty in the measured time value also varies with the inverse square root of the intensity. Figure 3-2 shows the relative uncertainty due to time width and intensity (assumes that intensity increases with λ^3 as shown in equation 2.71). The meaning of figure 3-2 is that the time of flight for a given neutron will be more uncertain; however, so many more neutrons will be recorded that the overall certainty in flight time for a given peak will be greater. Therefore, it is advantageous to use a reflector, even if the neutron spectrum is not going to be chopped.

3.4.3 Target Reflector

An series of monte-carlo evaluations were performed to verify a theory that a small reflector covering just the target could increase the flux by scattering high energy neutrons more efficiently than the moderator. In addition, it was thought that there may be additional flux

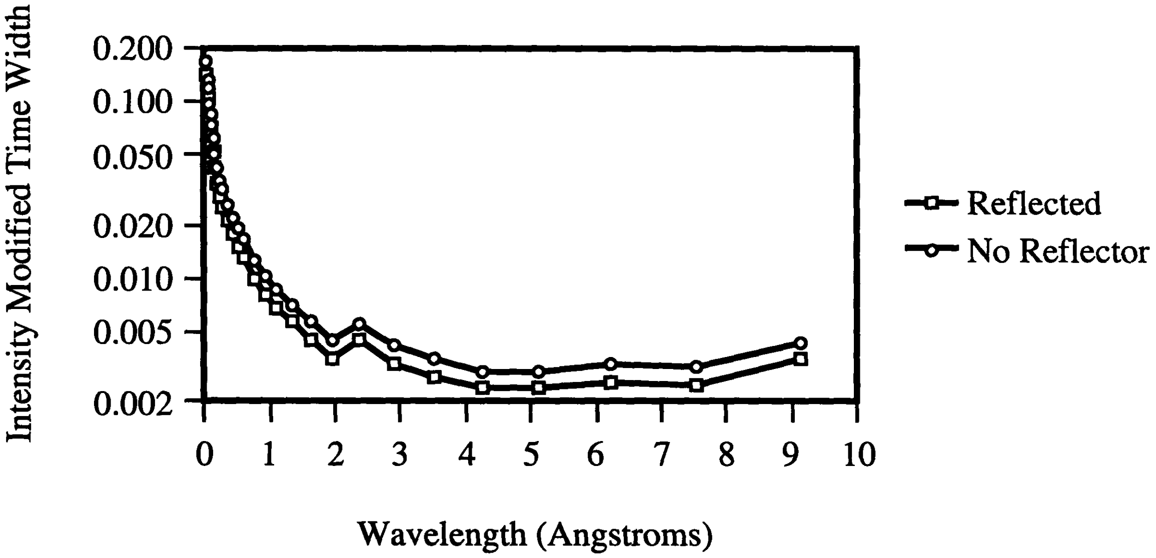

Figure 3-2: Intensity modified time width from CH_4 source.

due to neutron multiplication reactions. The potential limitation of such a small reflector is that the amount of moderator available for low energy scattering is reduced.

For the reflector material, the materials which performed most well in the large reflector evaluation were considered: Be, Ni, C, W, U-238, Cu, and H20. In each case, the real beryllium target was modeled as a 0.5 cm diameter spherical void. Surrounding this void was a 1 cm layer of the material in question, followed by 5 cm of water. In each case, the flux in the water was measured, assuming that all neutrons of energy less that 0.33 ev are thermal.

Figure 3-3 shows the results for the "best" performing materials. At 1 and 2 cm from the source center, the H_2O reflector resulted in the highest flux, while at more than 3 cm, the uranium flux is somewhat higher flux levels. However, this increase in flux is fairly insignificant (4%), and probably could be regained elsewhere if a target reflector is not used. The conclusion from this portion of the analysis is that the best thing to surround the target with is moderator.

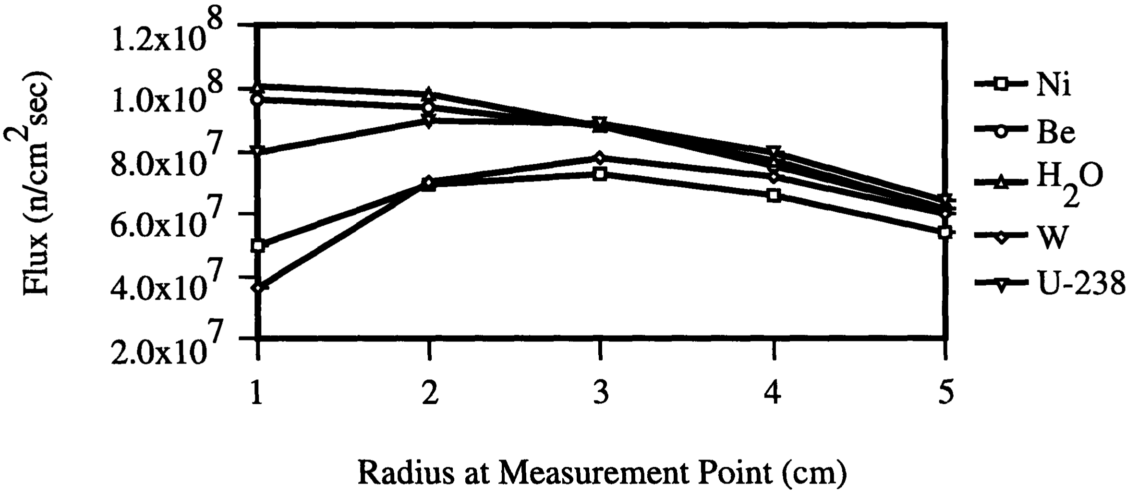

Figure 3-3: Effect of Materials Applied as Reflectors Around Target.

3.4.4 Optimization of Reflector Inner Radius

The "ideal" radii of reflected moderators are determined in this section, for moderators of light water, polyethelene, and liquid methane. Several monte-carlo simulations were carried out; each time a different moderator or moderator radius was modeled, starting with 5 cm and working up to 9 cm. The results are shown in Appendix D as contour graphs, figure D-1 corresponding to CH_4, figure D-2 corresponding to water, and figure D-3 corresponding to a polyethelene moderator.

If one was going to try to maximize the flux, while staying a "reasonable" distance from the source, say 3 cm in this case, then the following moderator radii would be appropriate: for CH_4, 5 cm; for water, 7 cm; and for polyethelene, 5 cm.

3.4.5 Optimization of Reflector Outer Radius

So far, the reflector has been assumed to be 6 cm thick; a thicker reflector would probably increase the flux going into the beam tube, but at the cost of higher dose rates outside

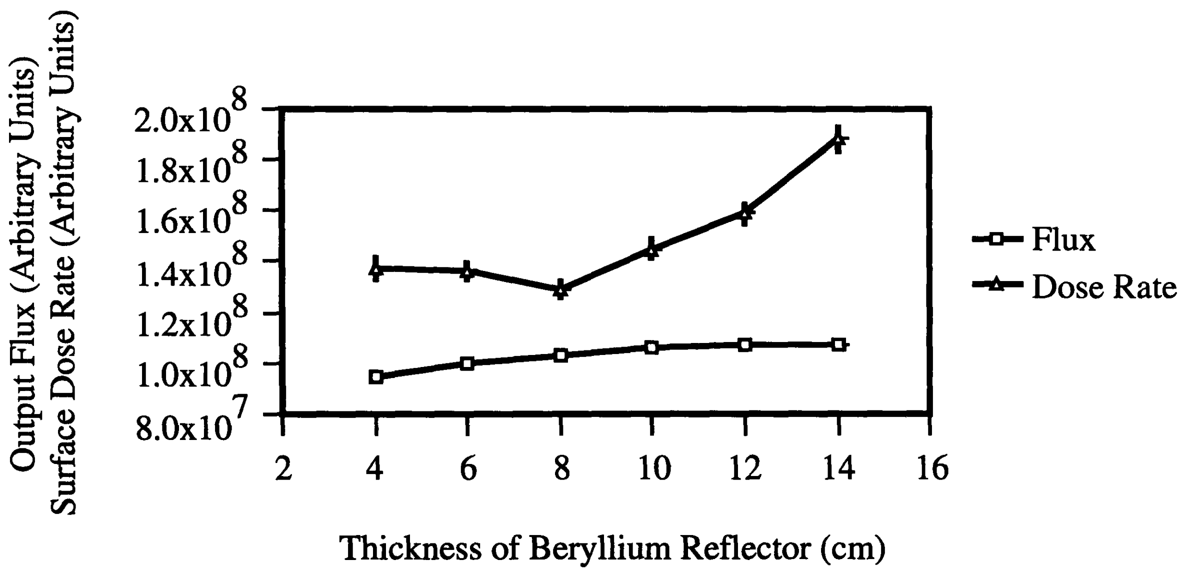

Figure 3-4: Effect of varying radius of reflected polyethelene moderator.

the source. Outside the source, a Be reflector actually decreases dose because it scatters high energy neutrons down, so that they can be thermalized and absorbed; if there is too much Be, however, dose rates will begin to rise because of the reduced amount of shielding material.

Figure 3-4 shows how dose rates external to the source and flux inside the source vary with reflector thickness. The figure illustrates that 8 cm is probably the "best" thickness for the reflector; additional thickness would just increase dose rate , while increasing the flux minimally.

3.4.6 Angular Dependence of Flux Inside Moderator

A attempt was made to see how flux varied with angle relative to a beam straight out of the source. Such a measurement was made with a set of angle and energy dependent tallies in a monte-carlo simulation. The goal of the investigation was to first see if there is a preferred direction of neutrons, and then see how the ratio of thermal flux to fast flux varies with

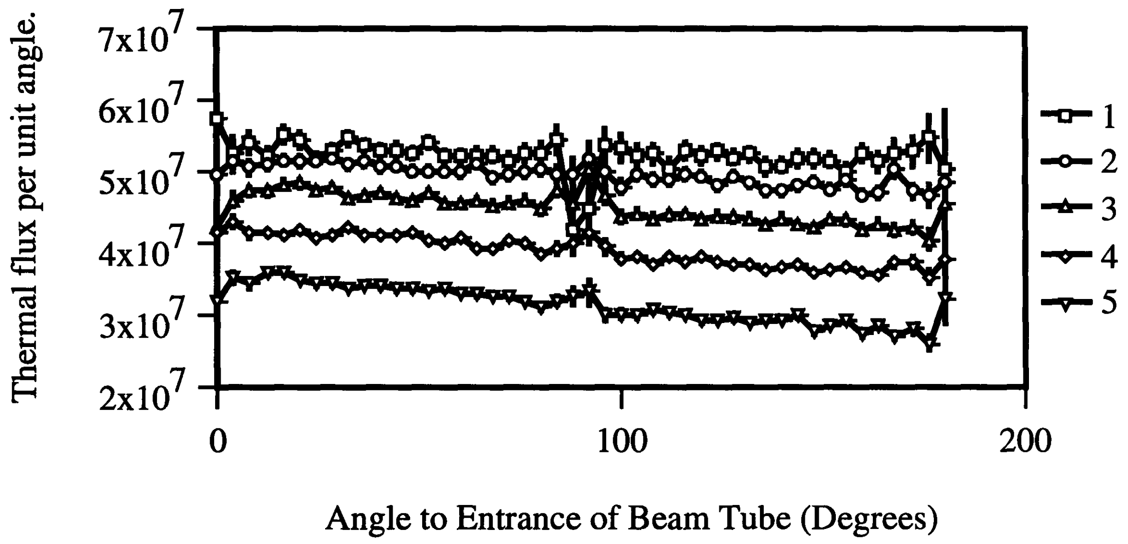

Figure 3-5: Flux vs measurement angle at several radii.

angle.

Figure 3-5 shows the flux vs. angle results, for measurements at five radii within the moderating sphere. It is evident that there is very little variation of flux dependent on angle; just a slight slope indicating that neutrons tend to diffuse out of the source rather than into it.

Figure 3-6 shows the thermal to fast neutron ratio at various angles and measurement radii. It is evident that this ratio increases with increasing angle; at about 90 degrees, however, uncertainties are high due to the measurement method. Even if these measurements were precise, they would probably not be correct; for thus far, the source beam itself has not been modeled. Such a beam tube is expected to be a major neutron sink.

3.4.7 Angular Dependence Measured with Beam Tubes.

The above results were inherently inaccurate near 90 degrees, because they didn't factor in the neutron loss due to beam tubes. A configuration employing 1 cm diameter beam tubes

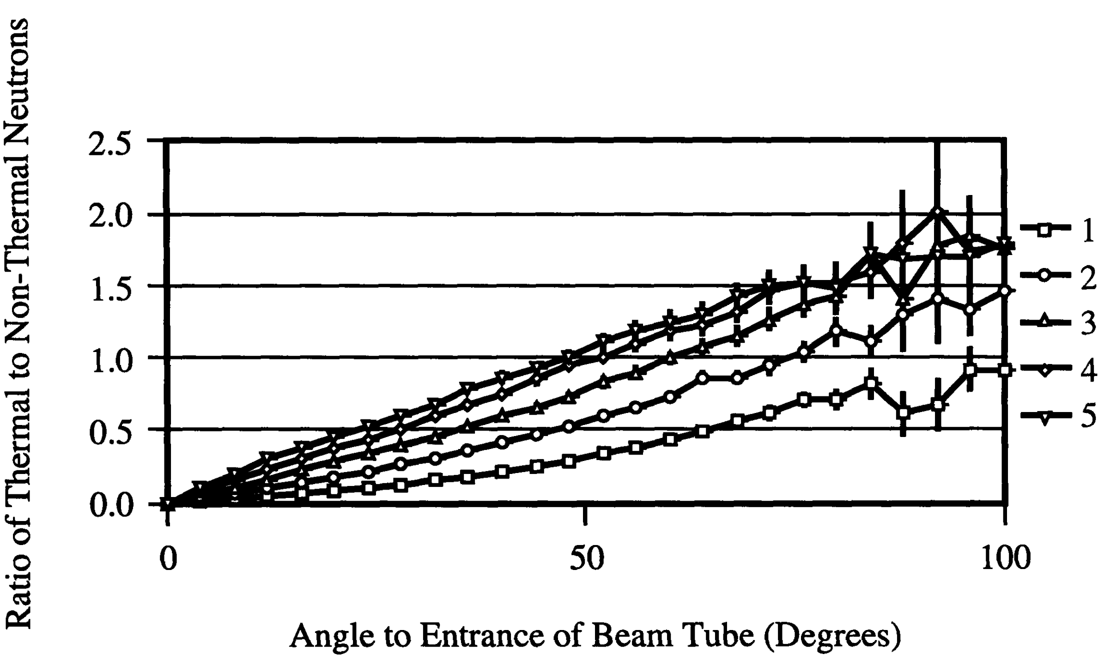

Figure 3-6: Thermal to fast flux ratio vs angle at several radii.

was evaluated, with measurement at angles of 0, 22.5, 45, 67.5, and 90 degrees relative to a beam straight out of the source.

Figure 3-7 shows the results; the thermal flux is essentially independent of the beam angle, while the thermal to fast ratio rises with increasing angle. Therefore, to reduce uncertainty, one ought to use a large angle relative to any beam straight out of the source.

3.4.8 Moderator Materials

Since hydrogen has a mass approximately equal to the neutron mass, it is the "best" moderating element in many cases, because a neutron can deposit up to half its energy to the hydrogen atom in a collision. It also has a high cross section for inelastic scattering a low energies. However, compared to deuterium and carbon, two other common moderators, it has a high absorption cross section, which may decrease its moderation efficiency somewhat. Nevertheless, it is not anticipated that absorption will have a major effect on the overall efficiency of a small moderator such as the one to be considered here, as the most of the

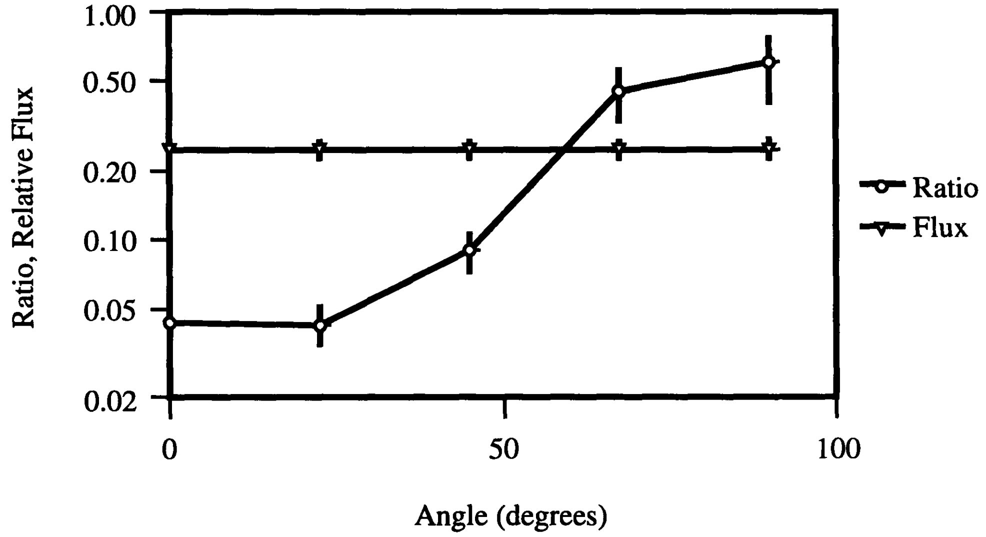

Figure 3-7: Flux parameters vs angle for beam tubes

neutron loss is expected to be due to escape, rather than capture. Therefore, it was assumed that greater hydrogen density would mean more efficient moderation.

Thermal water, at a temperature near or somewhat above room temperature is probably the most often used moderator, because it is cheap, easily available, and easy to manipulate. Assuming room temperature water with a density of 1 *gram/cc*, the hydrogen density can be easily calculated; it is simply the density of the water times the ratio of the atomic weight of the hydrogen atoms to the molecular weight of the water, or 0.112 *gram/cc*.

An evaluation was carried out, to see what materials moderated neutrons as well as or better than water. Normal water and ice were considered, as well as heavy water and heavy ice. Several other materials were examined, based on their high hydrogen content. Three temperature ranges were considered; thermal at 300 K, cool at 273 K, and cold at 20 K. In the two high temperature ranges, some materials had hydrogen densities much higher than water. From each temperature range, the materials with the highest hydrogen density were selected, so that both solid and liquid materials were represented. The materials, their temperature, state, hydrogen density, and nominal density are shown if table 3.5 In the low temperature range, solid methane, liquid hydrogen an solid deuterium were considered. Liquid ethane would have been considered, but a thermal scattering cross section kernel could not be found. In addition, there is evidence in the literature that methane is a much better moderator than ethane [40].

Using the Monte Carlo Neutron Transport Code (MCNP) from Los Alamos National Labs, the materials in table 3.5 were tested for their effectiveness as moderators. In each case, a 6 *cm* sphere of the material was assumed, with detectors arranged alone the radius of the sphere to see how the thermal flux varied with the radius. A 3 *Mev* neutron source emitting 10^{10} neutrons per second was assumed in the center of each sphere. 10^5 particle histories were tracked in each case. For many of the organic materials, no thermal scattering kernels were available. Therefore, the solid hydrocarbons were assumed to scatter like polyethelene, while the liquid ones were assume to behave like benzene.

The results of the MCNP simulation showed that in every case, the flux at all energies decreased along the radius. Therefore, to compare the materials, a radius of 2 cm was selected as the "reference" radius for comparing materials. For each material, the modified Maxwellian distribution from equation 2.37 was fit to the data. The integrated thermal flux (Φ_0) from each case is listed in table 3.5.

In the case of all the deuterium-containing materials, the Maxwellian fit was either very poor, or could not be fit at all; in any case, the integrated fluxes were orders of magnitude lower than in similar hydrogen-containing materials. The most effective moderator over all was shown to be $C_{13}H_{26}O_2$ at $273\,K$, a hydrocarbon with a melting point of $274\,K$. Since the scattering was assumed to be polyethelene-like, a potentially non-conservative assumption, these result will not be applied in this study; however, further study of this material is encouraged. The second-best moderator was $(CH_2)_n$, which is polyethelene, the common moderator that has been considered thus far in the analyses. Not surprisingly, the third-best moderator was $C_{19}H_{40}$ at $300\,K$, commonly called paraffin wax. and may be an effective shielding material, an area of the design where thermal interactions are not critical. Nevertheless, this is another moderator worthy of further study.

Table 3.5: Moderator Properties

Material	Temperature K	State	Hydrogen Density $gram/cc$	Nominal Density $gram/cc$	Integrated Flux at 2cm $1/cm^2sec$
H_2	20	Liquid	0.071	0.071	1.758×10^7
D_2	20	Solid	N/A	0.170	N/A
CH_4	20	Solid	0.132	0.524	1.332×10^7
H_2O	273	Solid	0.112	1.000	2.593×10^7
D_2O	273	Solid	N/A	1.104	0.010×10^7
H_4N_2	273	Solid	0.151	1.201	2.256×10^7
$C_{13}H_{26}O_2$ (Methyl Laurate)	273	Solid	0.152	1.236	$\mathbf{6.815}\times10^7$
H_2O	300	Liquid	0.112	1.000	$\mathbf{3.240}\times10^7$
D_2O	300	Liquid	N/A	1.104	0.002×10^7
$C_4H_{13}N_3$ (Diethylene Triamine)	300	Liquid	0.121	0.953	1.865×10^7
$C_8H_{23}N_5$ (Tetraethylene Pentamine)	300	Liquid	0.122	0.993	2.032×10^7
$C_{13}H_{26}O_2$ (Methyl Laurate)	300	Liquid	0.127	1.036	4.092×10^7
$C_{12}H_{27}N$ (Dodecane, 1-amino)	300	Solid	0.136	0.923	4.472×10^7
$C_{19}H_{40}$ (Paraffin Wax)	300	Solid	0.137	0.907	$\mathbf{5.092}\times10^7$
$(CH_2)_n$ (Polyethelene)	300	Solid	0.137	0.950	$\mathbf{5.257}\times10^7$

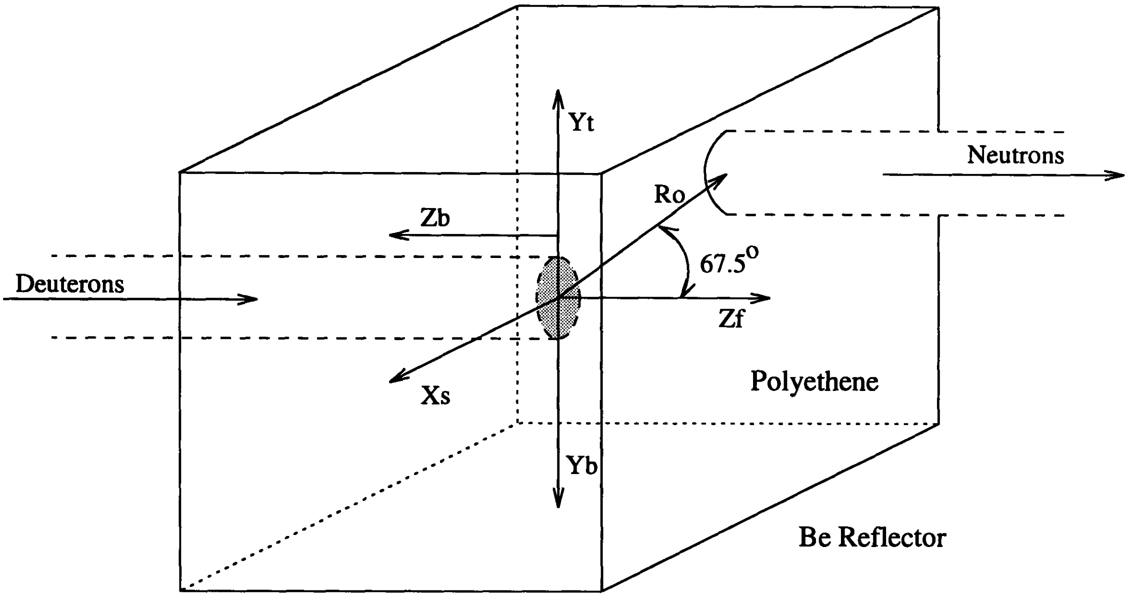

Figure 3-8: Geometry of Polyethelene-Moderated Neutron Source.

3.4.9 Moderator Geometry Optimization

In this step of the design process, the geometries of the moderators were specified more completely, to more closely approximate the "real world" configuration of the moderators. For example, spherical beryllium shells, which may not be available, were no longer modeled, in favor of rectangular beryllium blocks, which are available. Also, in the case of the cold source, the need to cool and insulate the source was considered.

Optimization of Thermal Neutron Source

The geometry of the thermal neutron moderator is shown in figure 3-8. It is a box of polyethelene, surrounded by 8 cm of beryllium (not shown); two 1 cm diameter holes enter the box, one for the deuteron beam and beryllium target, the other for the neutron beam.

It was assumed that input deuteron beam and the output neutron beam were both parallel with the Z-axis, in the Y-Z plane. The entrance to the neutron beam was assumed to be positioned along a vector extending from the target at 67.5 degrees. The thickness of the beryllium reflector was assumed to be 8 cm. Other geometrical factors were left variable, so that they could be optimized. The variables which were optimized were the:

1. Distance from target to sides of box (Xs) (Assumed right-left symmetric),
2. Distance from target to top of box (Yt),
3. Distance from target to bottom of box (Yb),
4. Distance from target to front of box (Zf),
5. Distance from target to back of box (Zb),
6. Distance from target to beam entrance (Ro).

The optimization consisted of estimating values for all of the above variables based on the results with the simple spherical source, then obtaining a Monte-Carlo approximation of the thermal flux. Each variable was then modified by a small increment (1 cm), and a set of Monte-Carlo approximations were obtained, each approximation corresponding to an incremental change in each variable. Based on big ($\approx$ 10%) changes, the estimated values were redefined. The optimization procedure was repeated until no changes were greater than 10%.

The resulting thermal flux was $3.0 \times 10^7 \frac{neutrons}{cm^2 sec}$ at $Xs = 5\ cm$, $Yt = 6\ cm$, $Yb = 6\ cm$, $Zf = 7\ cm$, $Zb = 5\ cm$, and $Ro = 8\ cm$.

Optimization of Cold Neutron Source

The geometry of the cold neutron moderator is shown in figure 3-9. Since the solid methane must be kept at cryogenic temperatures, it is assumed to be in a spherical, cooled, insulated container. Surrounding the insulating sphere is a layer of polyethelene, which fills up the space between the spherical moderator and the box-like Be reflector.

The insulation for the moderator was based on the assumption that 10 watts of cooling are available. Assuming a peak current of 140 μA of 900 kev deuterons, with a duty cycle of 2.25%, as per [42], the deuteron beam should deposit 2.83W to the moderator. Assuming

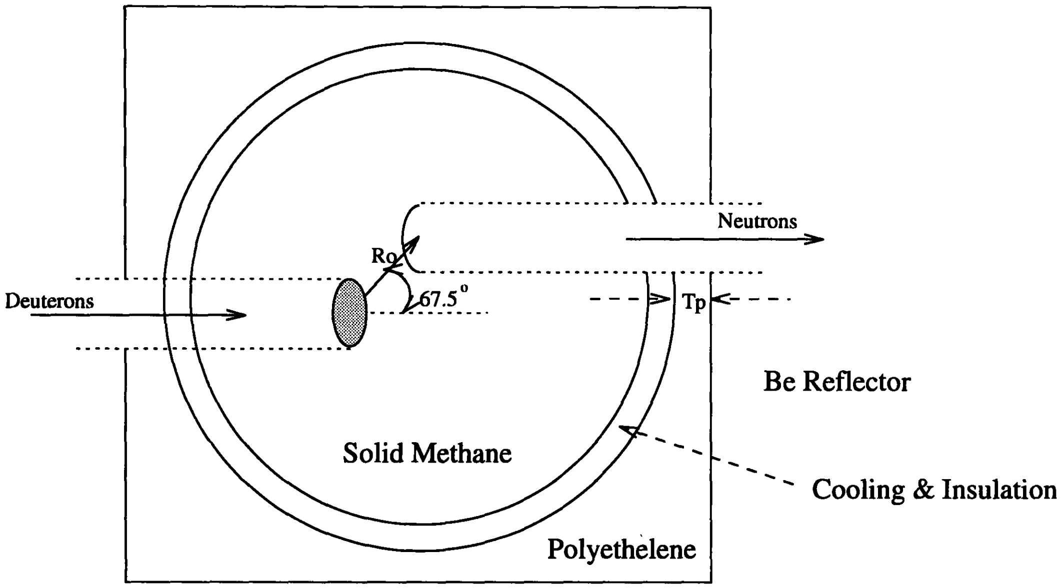

Figure 3-9: Geometry of Solid Methane Moderated Neutron Source.

a 1 cm diameter evacuated aluminum ($\epsilon = 0.1$) beam penetration into the moderator, the loss through the opening should be $\pi(1/2cm)^2\epsilon\sigma(T_{hot^4} - T^4_{cold}) = 0.01W$, assuming that $T_{hot} = 300K$ and $T_{cold} = 4K$.

Now, assuming that the moderator, container, cooling space, and cooling container have an outside radius of about r_1 =5.5 cm, the heat absorbed through the walls of the moderator is given by:

$$q = \frac{4\pi k_e(T - hot - T_{cold})}{r_1^{-1} - r_2^{-1}}, \tag{3.2}$$

where r_2 is the outer radius of the insulation, and k_e is the equivalent conductivity of the insulation around the moderator and cooler, given by:

$$k_e = k_0 \frac{T^2_{hot} + T^2_{cold}}{To^2_{hot} + To^2_{cold}} \frac{T_{hot} + T_{cold}}{To_{hot} + To_{cold}} \tag{3.3}$$

where k_0 is the thermal conductivity of the insulation measured at To_{hot} and To_{cold} [1]. Assuming a 0.2 cm thick layer of aluminized mylar evacuated insulation ($k_0 = 0.032mW/M\,K$

at 90 K and 273 K), the heat transfer through the insulated surface should be about 0.26 W. This gives a combined rate of heat gain for the moderator of 3.20 W, well within the capacity of a 10 W cooler.

For calculation purposes, the container walls, liquid He coolant, and insulation were modeled as a simple void 0.7 cm thick, between the solid methane and the polyethelene. Five parameters were varied, to try to optimize the flux n the output beam; these parameters were as follows:

1. Minimum thickness of Polyethelene Layer (Tp)
2. Radius of Methane Sphere (Rs)
3. Distance from target to beam entrance (Ro)
4. Z-axis displacement from target to center of moderator (Zc)
5. Y-axis displacement from target to center of moderator (Yc)

The optimization process was identical to the process used to obtain the optimum thermal flux. The resulting cold flux was $1.1 \times 10^7 \frac{neutrons}{cm^2 sec}$ at $Tp = 1\ cm$, $Rs = 5\ cm$, $Ro = 3.5\ cm$, $Zc = 1\ cm$, and $Yc = 0.5\ cm$.

3.5 sheilding

It is important to have an early estimate of the required shielding for the source at an early stage of the optimization process. The size and composition of the shielding not only determines the mass of the source assembly, but it also determines how roughly the beam can be collimated for a given beam width.

In general, the collimation of a collimated beam is given by *alpha*, the ratio of the width of a collimating section (w_c) to the length of the collimator (L). If the collimator is a Soller collimator, then $w_c = W/Nc$, where W is the width of the collimator and Nc is the number of collimating sections.

When performing neutron strain measurements, one may want to limit the area of the beam to a certain value, so that the measured volume is well defined; this sets a minimum value on W. At the same time, one may want the beam to have a great intensity, necessitating a large value of α. For a given maximum width W_{max}, the maximum ratio, α_{max} is limited by:

$$\alpha_{max} = \frac{W_{max}}{L_{min}}, \tag{3.4}$$

where $Lmin$ is determined by the size of the source shielding and the geometry of the source and sample.

3.5.1 Approximate Shielding Requirements

The shielding around the source performs two function; it protects the human operators, and it cuts down on stray neutrons, reducing noise. The shielding requirements for the sources was determined by assuming the area around the source is declared "restricted area" in accordance with 10CFR20. It is also assumed that a human operator stays 3 meters from the surface of the source 40 hours a week, 50 weeks a year. Under the requirements of 10CFR20, that person's quarterly dose limit is 1.25 rem, which translates into a hourly dose limit of 2.5 mrem/hour. The aim of the shielding design will be to meet this dose rate limit. In accordance with ALARA dose limitations, it is assumed that additional precautions will be take to lower the operator's dose rate below 2.5 mrem/hour; however, those precautions will not be accounted for in this analysis.

3.5.2 Shielding Optimization

The first shielding evaluations were designed to evaluate how a neutron-moderating, gamma producing material such as water could be combined with a neutron scattering, gamma absorbing material such as lead. Four Monte-Carlo simulations were performed: one with a shield of water only; one with water and 1 cm thick lead shields arranged every 10 cm in the water, one with water and 2 cm thick lead shields arranged every 10 cm in the water, and one with 3 cm of lead, surrounded by all water. The source was modeled as a 6 cm sphere of water, surrounded by 6 cm of beryllium reflector. The dose rate was measured within the shield at various radii, then adjusted to reflect the 3 meters of distance between the surface of the source and the operator.

The results, displayed in figure 3-10 shows that for small radius spheres, there is no advantage to the multiple shells of lead; the shells actually increase the dose rate by decreasing the amount of water available for moderating high energy neutrons down to low energies. A close examination of the results (Shown in Appendix E) reveals that in the all water and single Pb layer cases, much of the dose is due to photons which are not well shielded by the water; in the Pb shell cases, much of the dose is due to high energy neutrons. These results agree with the experimental results for shielding high- energy neutrons, as found in the literature [3, 2, 7]. In general, it seems that it is best to have a good high-energy scatterer near the source, followed by a moderator farther from the source.

Figure 3-10 shows that for a shield radius greater than 40 cm, there is a slight advantage to the Pb and water combination. The second set of shielding evaluations was intended to examine if there are other materials, which can case the same effect, but more so than Pb. 3 cm shields of Beryllium, Iron, and Tungsten, surrounded by water were modeled; their dose rates relative to the all water configuration are shown in figure 3-11. It is clear from the results that tungsten is the best choice; at every radius within the shield, it resulted in a lower dose than the other materials, and a lower dose than the all water configuration.

The third shielding evaluation examined how the neutron dose rate varies with the tungsten thickness, at various radii within the shield. The results, shown in Appendix E, figure E-5 indicate that the optimum thickness is about 8 cm. However, this means that a solid sphere of tungsten would be required, with a 12 cm inner radius and a 20 cm outer radius. Such a sphere would be very difficult and costly to manufacture.

As an alternative to the solid tungsten inner shield, an inner shield made of a water and powder tungsten slurry was considered. To determine the volume ratios, a simple model was employed: the tungsten particles were assumed to be all equally sized spherical particles well packed into an FCC-like array, with water filling in the inter-particle spaces. This gives the Tungsten a volume fraction of 74%, and the water 26%. Using these numbers, we get an

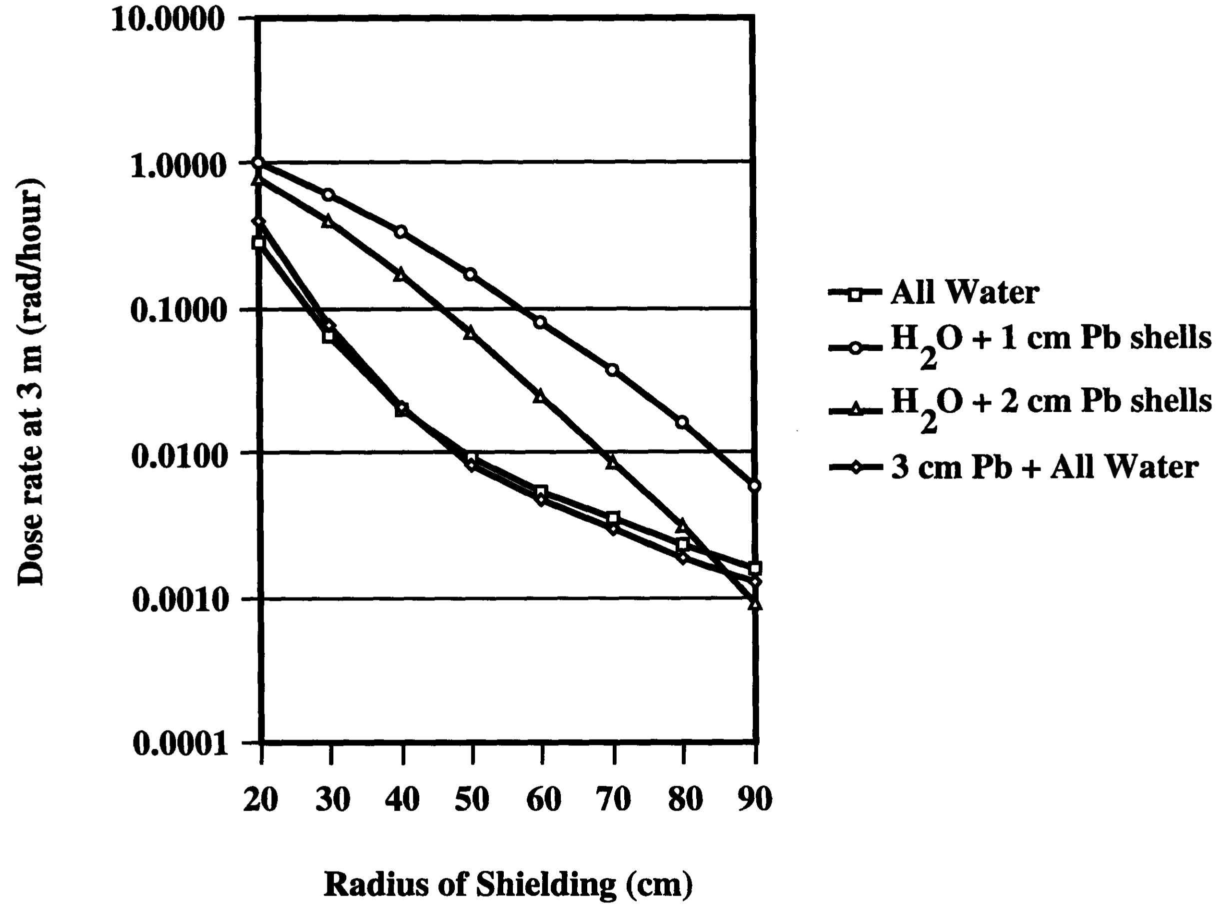

Figure 3-10: Dose rate at 3 meters vs radius of shield, for various water-lead combinations.

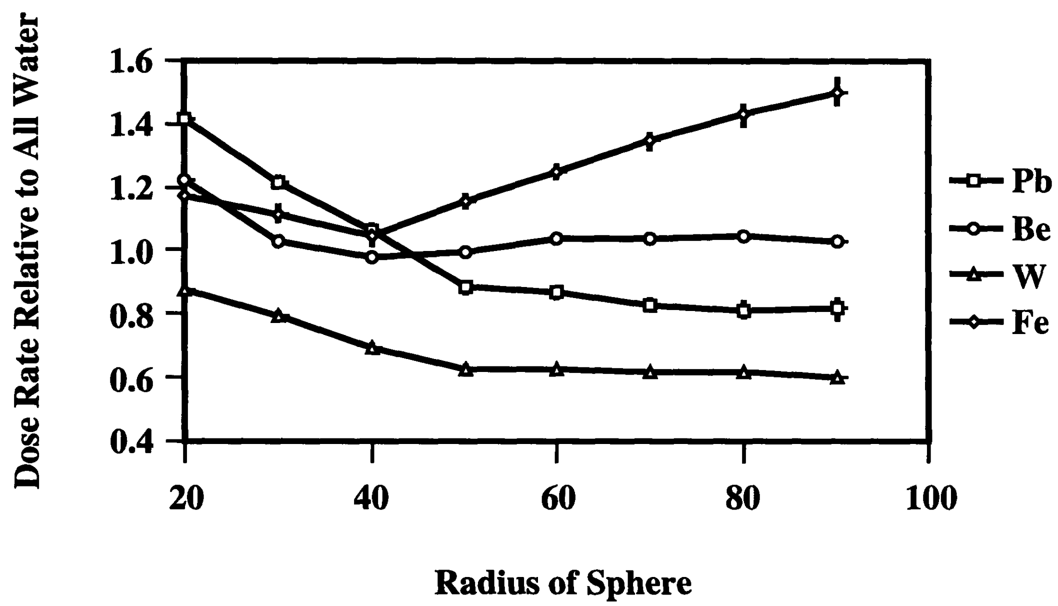

Figure 3-11: Dose rate relative to all water shield, for inner shields of Pb, Be, W, and Fe.

overall density of $14.55 g/cm^3$, and an atomic fraction of 64.3% tungsten and 35.7% water (23.8% hydrogen atoms and 11.9% oxygen atoms). The results for this shield (shown in figure E-6) indicate that the optimum water-tungsten thickness is about 12 cm, resulting in a lower dose rate than in the solid tungsten case.

If the outer shield is filled with boron, a neutron absorber, the neutron dose rate could be lowered even further. In case solid boron was found to be unavailable, a natural boron / water mixture similar to the tungsten-water mixture was considered. The mixture has a volume fraction of 74% solid boron, and 26% water. The ratio gives an overall density of $2.0 g/cm^3$, and an atomic fraction of 80% boron and 20% water (13.3% hydrogen atoms and 6.7% oxygen atoms). The shield was evaluated assuming the water-tungsten slurry inside, and the water-boron slurry outside. The results (shown in figure E-7) indicated that the optimum tungsten-water thickness was about 19 cm.

A tungsten powder sphere with a 12 cm inner radius and a 31 cm outer radius weighs about 3800 lbs. At an optimistic price of about \$50/pound, this means that the inner shield should cost about \$200,000! Clearly, another alternative is required. It was noted that the powdered tungsten, mixed with a moderator, was a better inner shield. It was also noted that polyethelene is a more efficient moderator than water. Combining these two ideas with the fact that any fraction of tungsten could be suspended in polyethelene led to the concept of a polyethelene-tungsten inner shield, and a polyethelene-boron outer shield.

Various percentages of tungsten and boron mixed with polyethelene were modeled, to see how the percentages affected the shielding ability. The results (shown in figure 3-12) indicate that the optimum volume percentage of tungsten and boron is 1%. Increasing or decreasing either the boron or tungsten concentration from this 1% value only increased the dose rate.

Based on the 1% boron and tungsten volume fractions, a final design was devised, consisting of a 19 cm thick layer of poly-tungsten, a 9 cm layer of poly-boron, and 5 cm of lead, to shield gamma rays from neutron capture. The MCNP results indicate that the dose rate at 3 meters from the surface is 2.2 mrad/hour, within the goal of 2.5 mrad/hour. About 50% of the dose is due to neutrons, while about 50% is due to photons, indicating that the ratio of neutron shielding to photon shielding is adequate.

3.6 Beam Collimation

The purpose of this section is to try to develop an understanding of the way various collimators affect beam intensity and angle uncertainty. Several types of collimators were considered.

3.6.1 Parallel Collimators

The simplest collimators are just beam tubes with constant cross sections. Of these, two designs were considered: those with rectangular cross sections and those with elliptical cross sections. In either case, for a surface source, the intensity transmitted through the tube is given by $I = I_0 \frac{A}{2\pi L^2}$, where A is the cross sectional area of the collimator, and L is the length of the tube.

Rectangular collimators are characterized by their collimation ratios: $\alpha = W/L$ and

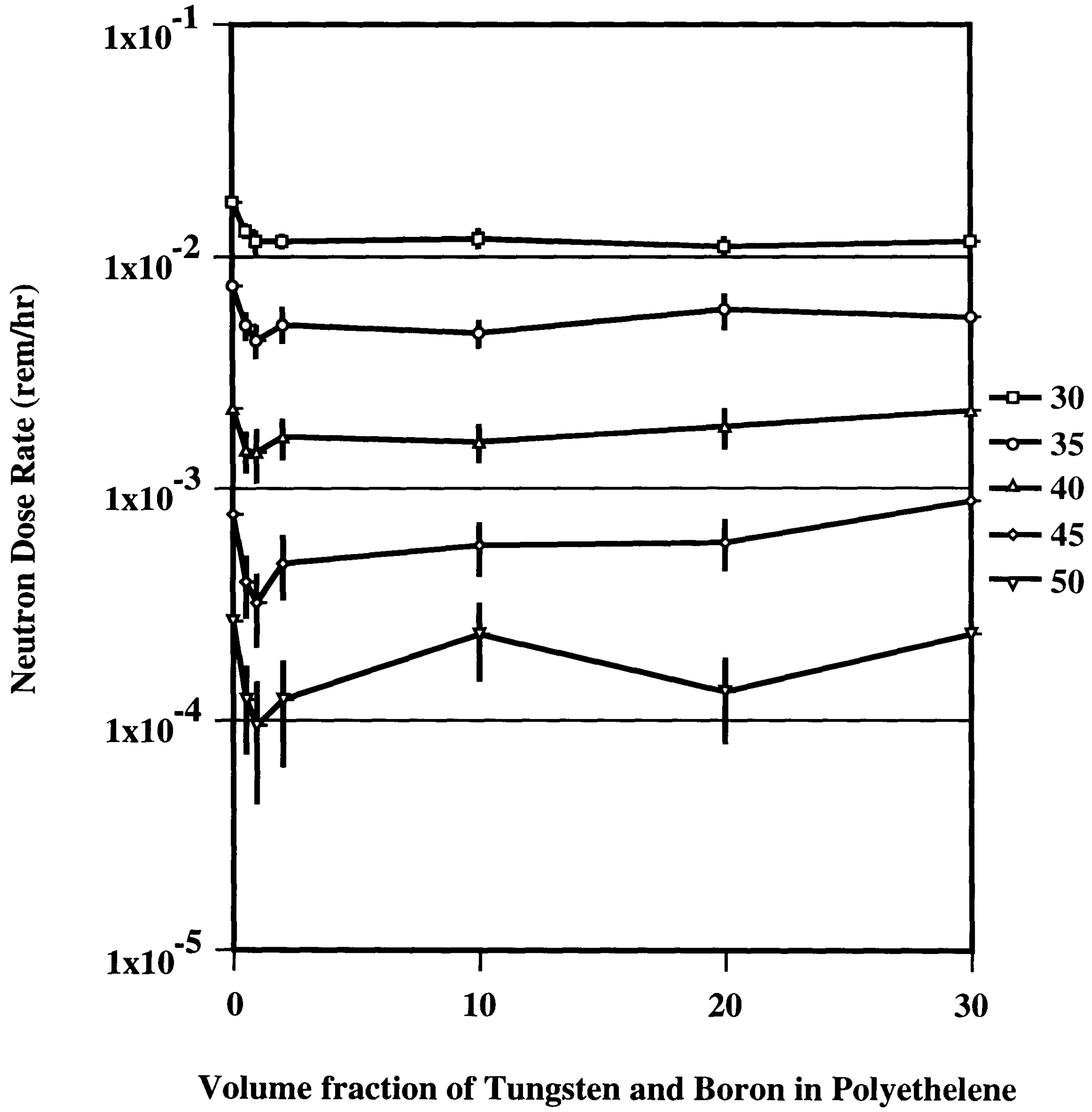

Figure 3-12: Dose Rate versus the volume fraction of W and B in a polyethelene shield.

$\beta = H/L$, where W is the width of the tube in the plane defined by changes in θ, and H is the height of the tube, perpendicular to W. The intensity transmitted is then given by $I = I_0 \frac{\alpha\beta}{2\pi}$. The angular distribution from such a tube is trapezoidal, with the maximum angle uncertainty being approximately equal to α. Such a distribution can be fit to a normal distribution of width σ_θ, if σ_θ is taken to be $\frac{\alpha}{\sqrt{2\pi}}$. This relationship was found through the simulation of several different collimators. In each case, several thousand particles were tracked, and their angular distribution fitted to a normal distribution. The overall best fit was obtained when $\sigma_{theta} = \frac{\alpha}{\sqrt{2\pi}}$.

Elliptical collimators are best characterized by the widths of their angular distributions, σ_θ and $\sigma_{\theta\perp}$, from which equivalent values for α and β can be obtained, where $\alpha = \sqrt{2\pi}\sigma_\theta$ and $\beta = \sqrt{2\pi}\sigma_{\theta\perp}$. The angular distribution from an elliptical collimator is not trapezoidal, but curved, making a normal distribution an easy fit. The best fit for σ_θ is given by $\sigma_\theta = \frac{a}{L}$, where a is the radius of the ellipse in the plane plane defined by changes in θ. There is an equivalent angular distribution in the perpendicular plane, given by $\sigma_{\theta\perp} = \frac{b}{L}$, where b is the radius of the ellipse perpendicular to a. Thus the equivalent α equals $\frac{a}{L}\sqrt{\pi}$ and the equivalent β equals $\frac{b}{L}\sqrt{\pi}$. Once again, the intensity transmitted is given by $I = I_0 \frac{\alpha\beta}{2\pi}$.

3.6.2 Cone Collimators

A somewhat more complicated situation arises when one end of the collimator is wider than the other end. In this case, the widths or radii of the wider end could be used in calculating the value of α and β. However, it should be noted that as the wider end gets several times wider than the narrower end, the assumption of a near-normal angular distribution becomes less valid.

To account for this, in the rectangular case, a slightly different definition of α can be used, where

$$\alpha = \frac{W_w}{L} \frac{2}{\sin(\frac{\pi}{2}(1 - \frac{W_t}{W_w})) + 2}, \tag{3.5}$$

W_w is the width of the wide end, and W_t is the width of the thin end.

3.6.3 Collimation and Azmuthal Angle

It is not necessary to explicitly collimate when measuring the azmuthal angle, ϕ of a neutron scattering from within a solid, as the angle is defined by the width of the beam and the width of the detector. In effect, a virtual collimator is formed by these two widths and the separation between them.

3.6.4 Radial Collimators

If one wishes to measure scattering at a specified angle from a location within a solid, it is necessary to collimate the neutrons scattering from that location, so that neutrons scattering at different angles from other locations are not counted also. However, if one wishes to measure scattering from one location at several angles simultaneously, several collimators can be pointed at the location, each positioned at a different angle.

In the case of monochromatic diffraction, the beam will diffract into a cone, defined by the angle 2θ. This cone will have a width $\sigma_\theta(\Theta)$, which is dependent on several factors (see Equation 2.27). It is assumed that the detectors are evenly spaced throughout the range of θ, each separated by an angle $d\theta$, and collimated to receive and angular distribution of width σ_{thetad}.

The intensity received by the set of detectors is given by

$$I = I_0 \frac{\beta}{2\pi} \int_{-\infty}^{\infty} \sum_{alldetectors} \frac{1}{\sqrt{2\pi}\sigma_\theta(\Theta)} \exp(-\frac{(2\theta_0 - \theta)^2}{2\sigma_\theta(\Theta)^2}) \exp(-\frac{(\theta_{detector} - \theta)}{2\sigma_{\theta d}^2})\ d\theta, \qquad (3.6)$$

where $2\theta_0$ is the angle of the scattering cone, and $\theta_{detector}$ is the angle at which each detector is positioned. Assuming a large number of detectors, where $\sigma_\theta(\Theta) > \sigma_{\theta d}$, the equation can be simplified to:

$$I = I_0 \frac{\beta}{2\pi} \frac{d\theta}{\sigma_{\theta d}}. \qquad (3.7)$$

Chapter 4

Evaluation

Using the source description, as laid out in Chapter 2, and the stress determination equations, as laid out in Chapter 1, a set of strain determination experiments were simulated. Two basic scenarios were examined; one using monochromatic neutrons, the other using time-of-flight detectors. In either case, the goal was to see how long it would take to resolve a stress with an uncertainty as low as 10% of the yield stress.

4.1 Evaluation of System Using Monochromatic Neutrons

The first part of Appendix F lists the MathCad worksheet used to determine the detection time for an experiment using monochromatic neutrons. Several different monochromators were evaluated. In each case, various reflections were examined, to determine which combination of monochromator and detector would resolve the stress in the least time.

Unfortunately, none of the combinations could resolve the 10% of yield strain in a time period less than several years. Therefore, the optimization of the system using monochromatic neutrons was not investigated further.

4.2 Evaluation of System Using Time-of-Flight Measurements

The second part of Appendix F lists the MathCad worksheet used to determine the detection time for an experiment using time-of-flight measurements. In this case, measurement times were generally on the order of tens of hours, meaning that a much more powerful source could perform these measurements in several minutes, a practical speed for an industrial system.

The first variables to be optimized dealt with the time spectrum of the beam; i.e. the distance of the chopper from the source (L_c), the time after the accelerator pulse at which the chopper reaches maximum open (t_0), and the time "width" of the chopper opening (s_t). At several values of L_c, the values of t_0 and s_t were varied to obtain the minimum stress detection time. The results for a sold methane moderator are shown in figure 4-1, which displays the optimum values of t_0 and s_t versus the distance between the chopper and the source. Also shown on the graph is the relative time required to make a measurement ($t_{10\%}$), and the time required if the chopper is removed (t_{inf}).

Since the chopper will most likely be located outside of the shielding, source to chopper distances less than 40 cm are unrealistic. However, for source to chopper distances greater than 20 cm, the measurement time without a chopper (t_{inf}) is less than the optimum measurement time with a chopper. The same conclusion was reached with the polyethelene moderator. Therefore, the system will not rely on chopping.

With more than about 16 azmuthal angle detectors, it was found that the measurement time becomes independent of the number of azmuthal angle detectors. Therefore, a modified form of equation 2.19 was employed to save computation time; equation 2.19 was analytically integrated over the range of ϕ ($-\pi/2$ to $\pi/2$), in effect modeling an infinite number of ϕ detectors, although the number was assumed to still be 16.

The next few optimizations amounted to varying the beam collimation and varying the number of θ detectors, so that the detection time reached a minimum. The optimum beam collimation was found to be the surprisingly high value of $\alpha = \beta = 0.117$, which represents

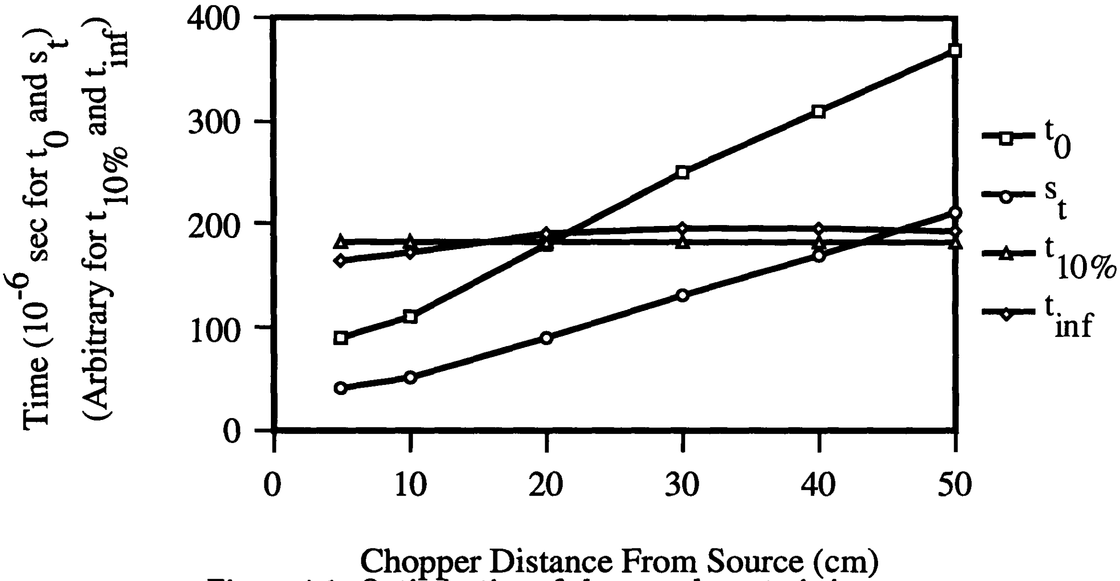

Figure 4-1: Optimization of chopper characteristics.

a 1 to 8.5 width to length ratio.

After several iterations, the optimum number of θ detectors was found to be about 128; combined with the 16 ϕ detection locations, this means that the system should have 2048 independent time of flight detectors, a high, but nevertheless realistic number.

The final value obtained for the time required to make a measurement with an accuracy of 10% of the yield strength was 8 hours. This is a practical length of time for making proof of concept measurements in a laboratory; however, to make measurements in an industrial setting, 8 hours is simply too long. However, if one obtains a source with similar characteristics to the one considered in this study, say with a thermal flux 100× higher than the flux considered here, then the time required to make a measurement falls to about 5 minutes, a practical length of time for industrial measurements.

Chapter 5

Conclusions and Recommendations for Further Work

5.1 Discussion

One way to evaluate the residual stress measurement system described in this thesis is to review and address the nine criteria for an ideal residual stress measurement system, as laid out in section 1.1.5;
The ideal residual stress measurement system should be:

1. *Portable, so that it can be taken to the measurement site.*
   The system is fairly portable, if attached to the back of a flatbed truck with a power generator. Since residual radioactivity is expected to be minimal, it is not expected that there will be any problem with transportation of the system. However, the requirement for an RFQ power supply, and the large mass of the shielding (about 1600 kg) severely limit the portability of the system.

2. *Maneuverable, so that it can be positioned in tight quarters, allowing for measurements at any location on a large object.*

   The system is about as maneuverable as the power supplies and other equipment which come with it, limiting its ability to measure at any location on a large object.

3. *Safe, so that it does not endanger the health of its operators.*

   There is some danger associated with the path of the beam into and out of the moderator/shield assembly. Assuming that these dangers can be avoided, the system is fairly safe, exposing an unprotected operator 3 meters away to less that 2.5 mrem/hour.

4. *Surface penetrating, so that the stresses anywhere within an object can be determined.*

   The low flux of an accelerator limits the surface penetration in iron to about a centimeter or two. However, this is several orders of magnitude better than many other systems, such as x-ray diffraction can claim.

5. *Precise enough to resolve small changes in stress.*

   The measurement precision increases with the square root of the measurement time. The baseline design, which can resolve stress to within 10% of the shear stress in 8 hours probably will not be very precise, as no one will be willing to wait for additional precision. A design using a flux 100 times greater than the flux of the baseline could resolve stresses down to 1% of the shear stress in about 8 hours, a somewhat reasonable time, if one really needs a precise measurement.

6. *Applicable to many engineering materials.*

   While only iron was examined in this study, there is no reason to believe that this method could not be applied to many other engineering materials. Some materials, such as nickel steel, would probably work better than iron, due to the high coherent scattering cross section of nickel. Other materials, such as borosillicate glasses, may not work so well.

7. *Socially acceptable, so that those who stand to benefit from it will not be afraid of it.*

   One objective of this design was to avoid the creation of radioactive waste products or residual radioactivity, two items that are very unpopular in our society; therefore a sub-critical booster was not investigated. Also, is not anticipated that an accelerator neutron source will be as threatening to people as many other neutron sources, such as radioisotopes or reactors, as an accelerator can simply be shut off.

8. *Inexpensive if mass-produced.*
   The dominant cost of an accelerator-based system for producing neutrons is the accelerator. The price of an accelerator which can produce 100 times the output of the baseline design could be between $100,000 for a Van de Graff generator [49] and approximately $500,000 for a RFQ linear accelerator [42]. In any case, the system is not inexpensive.

9. *Quick, so that measurements can be made within reasonable timeframes.*
   The baseline design, which can resolve stresses reasonably well in about eight hours is not "quick" by any means. However, if it successfully demonstrates technology which can be applied to a more powerful source, then it has shown that such a measurement could be done quickly.

5.2 Recommendations for Further Work

This system should be tested out, to see if it works as well as has been predicted. If it does manage to resolve stresses within eight hours or so, then the next logical step would be to proceed to a higher flux system, capable of making measurements in just a few minutes.

There is very little data in the literature about the angular and energy dependent cross section for deuterium-beryllium sources at low energies. It would be worthwhile to measure the angular and energy dependent cross section, so that 1) the data is available to the scientific community, and 2) so that this system can be better modeled.

Higher flux / lower energy neutron sources should be investigated. The higher flux results in quicker measurement times, while the lower energy reduces the amount of moderator and shielding required for the system.

In the section on moderator materials, $C_{13}H_{26}O_2$ (Methyl Laurate) was shown to be a potentially very effective moderator at 273 K. This material should be experimentally tested, to evaluate its actual performance as a moderator.

5.3 Conclusions

This thesis is significant, and unlike other works in the literature because it brings together the theory of neutron diffraction and diffracted intensity with practical concerns, such as the source of those diffracted neutrons and the application of the diffraction data to a specific problem, residual stress measurements.

Appendix A

Stress and Strain Theory

This appendix introduces the basics of stress and strain in polycrystalline materials as they relate to neutron diffraction.

A.1 Strains

A method of mathematically describing strains in a solid material is to embed three orthogonal unit vectors, $\hat{\imath}$, $\hat{\jmath}$, and $\hat{k}$ securely in the unstrained material. After a small uniform deformation occurs in the material, the unit vectors are distorted into the vectors $\hat{\imath}'$, $\hat{\jmath}'$, and $\hat{k}'$. So, an atom originally at the position

$$\vec{r} = x\hat{\imath} + y\hat{\jmath} + z\hat{k} \tag{A.1}$$

will be found at the position

$$\vec{r'} = x\hat{\imath}' + y\hat{\jmath}' + z\hat{k}'. \tag{A.2}$$

Ignoring translation of the axii, the new unit vectors may be expressed in terms of the old unit vectors:

$$\begin{aligned} \hat{\imath}' &= (1+\varepsilon_{xx})\hat{\imath} + \varepsilon_{xy}\hat{\jmath} + \varepsilon_{xz}\hat{k}; \\ \hat{\jmath}' &= \varepsilon_{yx}\hat{\imath} + (1+\varepsilon_{yy})\hat{\jmath} + \varepsilon_{yz}\hat{k}; \\ \hat{k}' &= \varepsilon_{zx}\hat{\imath} + \varepsilon_{zy}\hat{\jmath} + (1+\varepsilon_{zz})\hat{k}. \end{aligned} \tag{A.3}$$

The ε's define the deformation and rotation of each unit vector; in order to eliminate the rotational component, a different set of variables called *strain components* are typically used. The first three strain components (ϵ_x, ϵ_y, and ϵ_z) represent changes in the length of the orthogonal unit vectors, and are defined as:

$$\epsilon_x \equiv \varepsilon_{xx}; \quad \epsilon_y \equiv \varepsilon_{yy}; \quad \epsilon_z \equiv \varepsilon_{zz}. \tag{A.4}$$

The second three components, the *shear* strain components (γ_{xy}, γ_{yz}, and γ_{zx}) represent the angle cosines between the deformed vectors; they also ignore rotation of the axii:

$$\begin{aligned} \gamma_{xy} &\equiv \hat{\imath}' \cdot \hat{\jmath}' \cong \varepsilon_{yx} + \varepsilon_{xy}; \\ \gamma_{yz} &\equiv \hat{\jmath}' \cdot \hat{k}' \cong \varepsilon_{zy} + \varepsilon_{yz}; \\ \gamma_{zx} &\equiv \hat{k}' \cdot \hat{\imath}' \cong \varepsilon_{xz} + \varepsilon_{zx}. \end{aligned} \tag{A.5}$$

Combining equations A.3, A.4, and A.5 yields the following equations for the deformed vectors:

$$\begin{aligned} \hat{\imath}' &= (1+\epsilon_x)\hat{\imath} + \tfrac{1}{2}\gamma_{xy}\hat{\jmath} + \tfrac{1}{2}\gamma_{zx}\hat{k}; \\ \hat{\jmath}' &= \tfrac{1}{2}\gamma_{xy}\hat{\imath} + (1+\epsilon_y)\hat{\jmath} + \tfrac{1}{2}\gamma_{yz}\hat{k}; \\ \hat{k}' &= \tfrac{1}{2}\gamma_{zx}\hat{\imath} + \tfrac{1}{2}\gamma_{yz}\hat{\jmath} + (1+\epsilon_z)\hat{k}. \end{aligned} \tag{A.6}$$

Now the strain tensor $\mathcal{E}$ can be defined. It is a (3×3) matrix which includes all the strain components as follows:

$$\mathcal{E} = \begin{bmatrix} 1+\epsilon_x & \frac{1}{2}\gamma_{xy} & \frac{1}{2}\gamma_{zx} \\ \frac{1}{2}\gamma_{xy} & 1+\epsilon_y & \frac{1}{2}\gamma_{yz} \\ \frac{1}{2}\gamma_{zx} & \frac{1}{2}\gamma_{yz} & 1+\epsilon_z \end{bmatrix}. \tag{A.7}$$

Thus, the deformed position of an atom originally at $\vec{r}$ is given by:

$$\vec{r'} = \mathcal{E}\vec{r}, \tag{A.8}$$

It is worth noting that the strain tensor $\mathcal{E}$ is a symmetric matrix; i.e. $\mathcal{E}^T = \mathcal{E}$.

A.2 Stress and Strain Relations

According to Hooke's law, stresses leading to small elastic deformations (strains) are proportional to those strains. Thus stress components are linear functions of strain components, as follows:

$$\begin{aligned}
\sigma_x &= C_{11}\epsilon_x + C_{12}\epsilon_y + C_{13}\epsilon_z + C_{14}\gamma_{xy} + C_{15}\gamma_{yz} + C_{16}\gamma_{zx};\\
\sigma_y &= C_{21}\epsilon_x + C_{22}\epsilon_y + C_{23}\epsilon_z + C_{24}\gamma_{xy} + C_{25}\gamma_{yz} + C_{26}\gamma_{zx};\\
\sigma_z &= C_{31}\epsilon_x + C_{32}\epsilon_y + C_{33}\epsilon_z + C_{34}\gamma_{xy} + C_{35}\gamma_{yz} + C_{36}\gamma_{zx};\\
\tau_{xy} &= C_{41}\epsilon_x + C_{42}\epsilon_y + C_{43}\epsilon_z + C_{44}\gamma_{xy} + C_{45}\gamma_{yz} + C_{46}\gamma_{zx};\\
\tau_{yz} &= C_{51}\epsilon_x + C_{52}\epsilon_y + C_{53}\epsilon_z + C_{54}\gamma_{xy} + C_{55}\gamma_{yz} + C_{56}\gamma_{zx};\\
\tau_{zx} &= C_{61}\epsilon_x + C_{62}\epsilon_y + C_{63}\epsilon_z + C_{64}\gamma_{xy} + C_{65}\gamma_{yz} + C_{66}\gamma_{zx}.
\end{aligned} \tag{A.9}$$

The 36 C's are the elastic constants of the material; they have units of stress. Many of these constants tend to be equal to each other or zero, in accordance with energy conservation laws and the degree of symmetry in the material. For example, in an isotropic material there are only two independent elastic constants, E and ν, as

$$\begin{gathered}
C_{11} = C_{22} = C_{33} = \tfrac{E(1-\nu)}{(1+\nu)(1-2\nu)},\\
C_{44} = C_{55} = C_{66} = \tfrac{E}{2(1+\nu)},\\
C_{12} = C_{21} = C_{13} = C_{31} = C_{23} = C_{32} = \tfrac{\nu E}{(1+\nu)(1-2\nu)},\\
C_{other} = 0.
\end{gathered} \tag{A.10}$$

A.3 Note on Math

Much of the math in this section relies on a few simple matrix identities. First,

$$\mathbf{M}\vec{A} \cdot (\mathbf{M}\vec{B} \times \mathbf{M}\vec{B}) = |\mathbf{M}|\vec{A} \cdot (\vec{B} \times \vec{C}), \tag{A.11}$$

where $\mathbf{M}$ is a 3×3 matrix, and $\vec{A}$, $\vec{B}$, and $\vec{C}$ are vectors. Also,

$$\mathbf{M}^T(\mathbf{M}\vec{B} \times \mathbf{M}\vec{B}) = |\mathbf{M}|\vec{B} \times \vec{C}, \tag{A.12}$$

where $\mathbf{M}^T$ represents the transpose of $\mathbf{M}$. Combining these two relations yields:

$$\frac{\mathbf{M}^T((\mathbf{M}\vec{B}) \times (\mathbf{M}\vec{C}))}{\mathbf{M}\vec{A} \cdot ((\mathbf{M}\vec{B}) \times (\mathbf{M}\vec{C}))} = \frac{\vec{B} \times \vec{C}}{\vec{A} \cdot (\vec{B} \times \vec{C})}, \tag{A.13}$$

which is an important simplification to be used later in the text.

For example, we can now determine that the determinant of $\mathcal{E}$ gives the volume ratio of the unstrained unit cell to the strained unit cells, as the unstrained volume equals $\vec{a}_1(\vec{a}_2 \times \vec{a}_3)$, which equals $(\mathcal{E}\vec{a}_1) \cdot ((\mathcal{E}\vec{a}_2) \times (\mathcal{E}\vec{a}_3))/|\mathcal{E}|$, as per equation A.11.

A.4 Crystal Lattices

A perfect crystal lattice can be represented by a single unit cell, repeated continuously in space. This unit cell may be expressed by three basic vectors corresponding to the edges of the unit cell. In the orthorhombic case, these vectors ($\vec{a_1}$, $\vec{a_2}$, and $\vec{a_3}$) are simply $(a, 0, 0)$, $(0, b, 0)$, and $(0, 0, c)$, where a, b, and c are the dimensions of the unit cell.

For every crystal lattice described by three basic vectors, there is a reciprocal lattice, described by three reciprocal vectors, $\vec{b_1}$, $\vec{b_2}$, and $\vec{b_3}$, defined by equations A.14.

$$\vec{b_1} = \frac{\vec{a_2} \times \vec{a_3}}{\vec{a_1} \cdot (\vec{a_2} \times \vec{a_3})}, \quad \vec{b_2} = \frac{\vec{a_3} \times \vec{a_1}}{\vec{a_2} \cdot (\vec{a_3} \times \vec{a_1})}, \quad \vec{b_3} = \frac{\vec{a_1} \times \vec{a_2}}{\vec{a_3} \cdot (\vec{a_1} \times \vec{a_2})}. \tag{A.14}$$

Like the basic vectors, these reciprocal vectors correspond to the edges of a reciprocal unit cell, which is repeated throughout reciprocal space.

Vectors which connect points on a reciprocal lattice are perpendicular to planes in the associated real lattice. Thus, if we denote a vector $\vec{R}$ between two points in a reciprocal lattice with the indices (h, k, l); then $\vec{R}$ is normal to the (h, k, l) plane. $\vec{R}$ can be calculated from:

$$\vec{R} = h\vec{b_1} + k\vec{b_2} + l\vec{b_3}. \tag{A.15}$$

The length of this vector is inversely related to d_0, the interplanar spacing for the (h, k, l) plane, as $|R| = \frac{1}{d}$.

A polycrystalline material may be approximated by many small perfect crystals, oriented at all possible directions. The rotated basic vectors can be obtained by applying a rotation tensor $\mathbf{D}$ to the original vectors;

$$\vec{a_1^r} = \mathbf{D}\vec{a_1}, \quad \vec{a_2^r} = \mathbf{D}\vec{a_2}, \quad \vec{a_3^r} = \mathbf{D}\vec{a_3}, \tag{A.16}$$

where $\mathbf{D}$ is the set of direction cosines corresponding to the rotated axii of each microcrystal. It is worth noting now that the $\mathbf{D}$'s are orthogonal tensors; they only cause rotation, not deformation. Hence, $\mathbf{D}^T = \mathbf{D}^{-1}$, and $|\mathbf{D}| = 1$. These simplifications will become relevant later in the analysis.

When a set of basic vectors is rotated, the corresponding set of reciprocal vectors also rotates. As the following few equations show, the reciprocal lattice undergoes the same rotation as the basic lattice:

$$\vec{b_1^r} = \frac{\vec{a_2^r} \times \vec{a_3^r}}{\vec{a_1^r} \cdot (\vec{a_2^r} \times \vec{a_3^r})} = \frac{\mathbf{D}\vec{a}_2 \times \mathbf{D}\vec{a}_3}{\mathbf{D}\vec{a}_1 \cdot (\mathbf{D}\vec{a}_2 \times \mathbf{D}\vec{a}_3)} \tag{A.17}$$

$$\mathbf{D}^T \vec{b_1^r} = \frac{\mathbf{D}^T((\mathbf{D}\vec{a_2}) \times (\mathbf{D}\vec{a_3}))}{\mathbf{D}\vec{a_1} \cdot ((\mathbf{D}\vec{a_2}) \times (\mathbf{D}\vec{a_3}))} = \frac{\vec{a_2} \times \vec{a_3}}{\vec{a_1} \cdot (\vec{a_2} \times \vec{a_3})} = \vec{b_1}. \tag{A.18}$$

Thus $\vec{b_1^r} = (\mathbf{D}^T)^{-1}\vec{b_1} = \mathbf{D}\vec{b_1}$.

If the reciprocal lattice is rotated in every possible direction, any set of (h, k, l) indices describe a sphere of radius $|\vec{R}|$.

Applying a stress to a lattice will deform it; in small regions this deformation will be uniform, and representable by a set of strains. In a polycrystalline material, it is assumed that the micro-crystals are small enough that each crystal undergoes uniform deformation when the material is stressed. Uniform strain applied to a crystal deforms the basic vectors which describe that crystal. This deformation can be modeled by multiplying each basic vector with the strain tensor $\mathcal{E}$ (equation(A.7):

$$\vec{a_n^d} = \mathcal{E}\vec{a_n^r} = \mathcal{E}\mathbf{D}\vec{a_n}.$$

A deformed basic lattice will lead to a deformed reciprocal lattice. Using the same logic as in equations A.17 and A.18, we find

$$\vec{b_1^d} = (\mathcal{E}^T)^{-1}\vec{b_1^r} = \mathcal{E}^{-1}\vec{b_1^r}$$

So, under rotation and deformation, a reciprocal vector $\vec{R}$ becomes $\vec{R^d}$, where

$$\vec{R^d} = (\mathcal{E})^{-1}\mathbf{D}\vec{R} = (\mathcal{E})^{-1}\vec{R^r}.$$

Notice that $\mathcal{E}\vec{R^d} = \vec{R^r}$. Since we are only considering powder diffraction, only the length of the $\vec{R}$ vectors are important. Since rotation does not change the length of a vector, we can say $|\vec{R}| = |\vec{R^r}|$. Since $\mathcal{E}\vec{R^d} = \vec{R^r}$ we can also say

$$|\vec{R}| = |\mathcal{E}\vec{R^d}|. \tag{A.19}$$

This is the basic relationship between reciprocal lattice vectors and the strain tensor which can be manipulated to determine the 3-dimensional stresses in a polycrystalline material.

Appendix B

Prediction of θ in a Scattering Experiment

If one were to simulate the diffraction process through a strained material, say for a Monte Carlo calculation, it becomes necessary to determine the value of θ for a given set of ϕ, $\mathcal{E}$, λ, and d_0 values. If such a determination was done numerically, one would most likely start with a guess value for θ, based on the assumption of no strain, and then iteratively determine the correct value of θ, using equation 2.9. However, this could be time-consuming if a large number of determinations must be made; an analytical method would be quicker, determining the θ values without needing to iterate.

An analytical method for determining θ can be devised by first expanding equation 2.9 and making a few simplifying substitutions[1]:

$$\begin{gathered} A\sin^2 2\theta + B[\cos(2\theta) - 1]^2 + C\sin(2\theta)[\cos(2\theta) - 1] - D = 0, \\ \text{where} \\ A = \eta_{xy}\cos(\phi)\sin\phi + \eta_{xx}\cos^2(\phi) + \eta_{yy}\sin^2(\phi), \\ B = \eta_{zz}, \quad C = \eta_{yz}\sin(\phi) + \eta_{zx}\cos(\phi), \quad \text{and} \quad D = \frac{\lambda^2}{d_0^2} \end{gathered} \tag{B.1}$$

---

[1] The η's were defined in equation 2.5.

Now, if the $\sin(2\theta)$ and $\cos(2\theta)$ terms are expanded into their exponential equivalents, and the following substitution is made;

$$X = e^{2i\theta}, \tag{B.2}$$

then equation B.1 becomes

$$\begin{gathered} c_4X^4 + c_3X^3 + c_2X^2 + c_1X + c_0 = 0, \\ \text{where} \\ c_4 = A - B + iC, \quad c_3 = 4B - 2iC, \quad c_2 = 2A - 6B + 4D, \\ c_1 = 4B + 2iC, \ \text{and} \ c_0 = A - B - iC. \end{gathered} \tag{B.3}$$

A real positive root of X can then be determined analytically, using a technique such as the one described in [6]. The value of θ is then simply

$$\theta = -\frac{i}{2} ln(X). \tag{B.4}$$

Appendix C

Characterization of Deuterium on Beryllium Neutron Source

The next seven pages list the MathCad worksheet used to calculate the MCNP source description. The calculation is carried out assuming a deuteron energy of 900kev.

Following the worksheet are the actual MCNP source descriptions; the first one assumes 900 kev deuterons, while the second one assumes 1500 kev deuterons. They both model a 50 μsec pulse from a source emitting 10^{10} neutrons per second, with the deuteron beam traveling along the x-axis, striking the target at the origin.

C.1 Characterization of Deuterium on Beryllium Neutron Source

$\theta := (0\ \ 30\ \ 60\ \ 90\ \ 120\ \ 150)^T$ $\quad i := 0..5$ **Define set of angle values**

$Q := (0.78\ \ 2.21\ \ 2.62\ \ 3.64\ \ 4.36)$ $\quad j := 0..4$ **Define Q values (Mev)**

Data from Karadeniz: Deuterons at 600 kev

Relative Pulse Areas:
Columns corresponnd to Q-values
Rows correspond to angle values.

Relative Detector Efficiencies
corresponding to angle:

$$Kh := \begin{bmatrix} 51 & 46 & 42 & 56 & 24 \\ 38 & 12 & 09 & 18 & 10 \\ 31 & 20 & 11 & 22 & 10 \\ 35 & 30 & 18 & 48 & 19 \\ 17 & 33 & 15 & 43 & 22 \\ 10 & 22 & 09 & 26 & 22 \end{bmatrix} \qquad Kv := \begin{bmatrix} 1.96 \\ 0.43 \\ 0.63 \\ 0.73 \\ 0.43 \\ 0.35 \end{bmatrix}$$

Adjust data, to account
for detector efficiencies:

$$D600_{i,j} := \frac{Kh_{i,j}}{Kv_i}$$

Look at adjusted data:

$$D600 = \begin{bmatrix} 26 & 23 & 21 & 29 & 12 \\ 88 & 28 & 21 & 42 & 23 \\ 49 & 32 & 17 & 35 & 16 \\ 48 & 41 & 25 & 66 & 26 \\ 40 & 77 & 35 & 100 & 51 \\ 29 & 63 & 26 & 74 & 63 \end{bmatrix}$$

Data from Siemssen: (at 1100, 1540, and 1950 kev)

$$D1100 := \begin{bmatrix} 1.5 & 2.1 & 0.90 & 6.6 & 6.0 \\ 3.5 & 3.2 & 1.41 & 6.9 & 6.0 \\ 5.1 & 4.2 & 1.05 & 7.4 & 5.3 \\ 4.9 & 4.1 & 0.87 & 7.8 & 6.0 \\ 3.5 & 4.2 & 1.05 & 9.0 & 7.5 \\ 2.8 & 4.1 & 1.35 & 9.4 & 9.0 \end{bmatrix} \qquad D1540 := \begin{bmatrix} 1.3 & 2.9 & 0.60 & 9.0 & 6.8 \\ 3.3 & 4.5 & 1.17 & 9.5 & 7.1 \\ 5.9 & 5.3 & 0.60 & 8.7 & 6 \\ 6.4 & 4.4 & 0.75 & 7.8 & 5.6 \\ 4.9 & 4.5 & 1.05 & 8.3 & 6.6 \\ 4.1 & 4.9 & 1.11 & 8.1 & 6.3 \end{bmatrix}$$

$$D1950 := \begin{bmatrix} 1.4 & 3.8 & 0.84 & 9.2 & 6.2 \\ 2.9 & 4.6 & 1.50 & 10.5 & 9.8 \\ 4.5 & 4.5 & 0.87 & 8.9 & 7.2 \\ 5.4 & 4.1 & 0.87 & 7.5 & 6.2 \\ 4.7 & 4.2 & 1.05 & 9.3 & 7.5 \\ 2.5 & 5.1 & 1.17 & 9 & 7.4 \end{bmatrix}$$

Convert data sets into normalized cross sections:

$$\sigma600 := \frac{D600}{\sum_{i}\sum_{j} D600_{i,j}} \qquad \sigma1100 := \frac{D1100}{\sum_{i}\sum_{j} D1100_{i,j}}$$

$$\sigma1540 := \frac{D1540}{\sum_{i}\sum_{j} D1540_{i,j}} \qquad \sigma1950 := \frac{D1950}{\sum_{i}\sum_{j} D1950_{i,j}}$$

Fit 3rd order polynomial equation to each data set: $N := 3$

$$xx := \begin{bmatrix} 600 \\ 1100 \\ 1540 \\ 1950 \end{bmatrix} \quad Y(k,l) := \begin{bmatrix} \sigma 600_{k,l} \\ \sigma 1100_{k,l} \\ \sigma 1540_{k,l} \\ \sigma 1950_{k,l} \end{bmatrix} \quad n := 0..N \quad X^{<n>} := \overrightarrow{xx^{n}}$$

$$bb := \left(X^{T} \cdot X\right)^{-1}$$

Interpolate values for E=900 kev

$$E := 900 \qquad \sigma E_{i,j} := \left| \sum_{n} bb^{<n>^{T}} \cdot \left(X^{T} \cdot Y(i,j)\right) \cdot E^{n} \right|$$

Look at values:

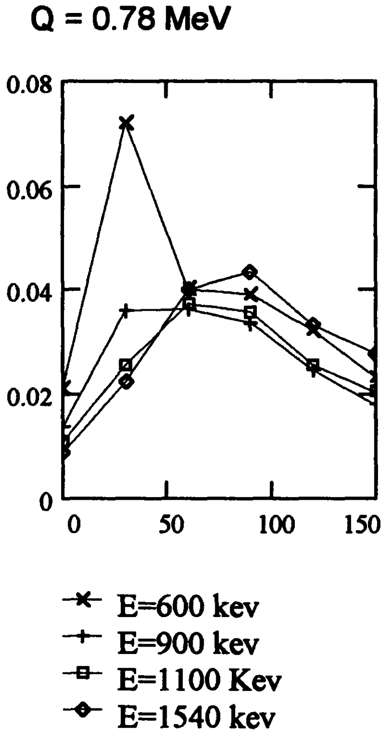

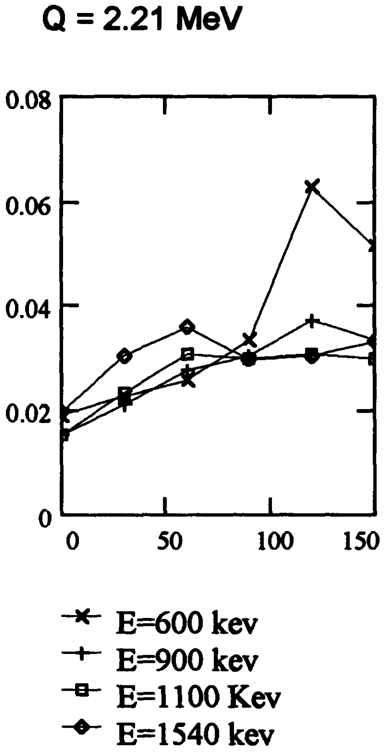

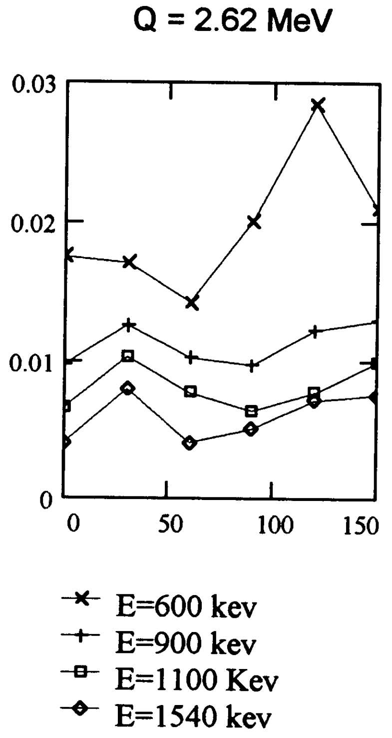
Q = 2.62 MeV

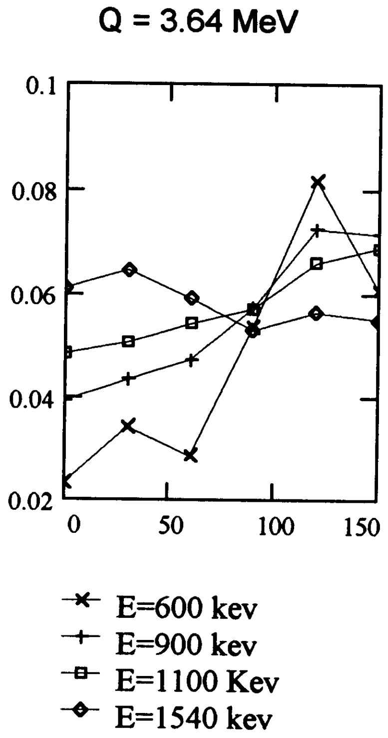
Q = 3.64 MeV

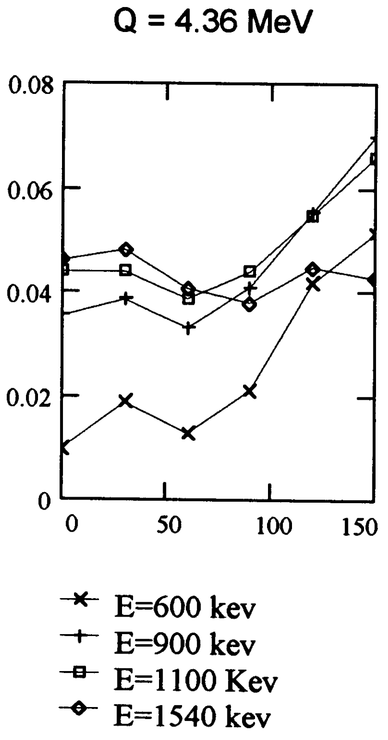
Q = 4.36 MeV

Now need to form general expression for $\sigma(\phi, Q)$

$m := 21 \quad \phi := -1, -1 + \dfrac{2}{m-1} .. 1$ Create range of ϕ values

Fit 4th order polynomial to data at 900 kev:

$$N := 4 \quad n := 0..N \quad \mu := \overrightarrow{\cos(\theta \cdot deg)} \quad x^{<n>} := \overrightarrow{\mu^{n}} \quad b := \left(x^{T} \cdot x\right)^{-1} \cdot \left(x^{T} \cdot \sigma E\right)$$

$$\sigma(\phi, j) := \sum_{n} \phi^{n} \cdot b_{n,j}$$

Look at fit of polynomials:

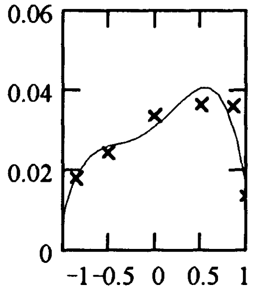
Q = 0.78

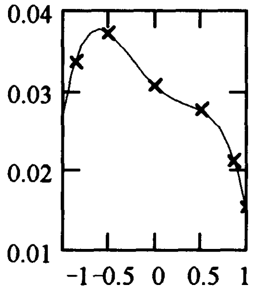
Q = 2.21

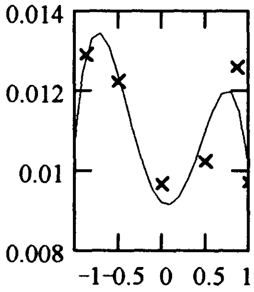
Q = 2.62

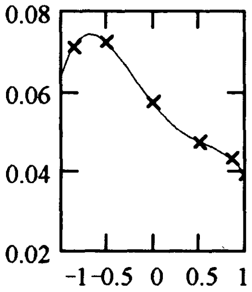
Q = 3.64

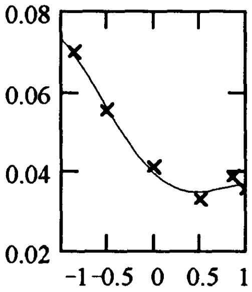
Q = 4.36

Adjust Data for MCNP:

$v := 7 \quad q := 0..v-1 \quad \phi_q := \cos\left(\frac{\pi \cdot q}{v-1}\right)$ **Make set of Cosine bins**

$\sigma E_{6,j} := \sigma(\phi_6, j) \qquad ii := 0..6 \qquad N\sigma E_{ii,j} := \frac{\sigma E_{ii,j}}{\sum_{ii} \sigma E_{ii,j}}$ **Renormalize cross-sections**

$pE_{i,j} := (\phi_i - \phi_{i+1}) \cdot \frac{N\sigma E_{i,j} + N\sigma E_{i+1,j}}{2}$ **Convert cross-sections to probabilities**

$spE := \sum_i \sum_j pE_{i,j} \qquad pE := \frac{pE}{spE}$ **Normalize probabilities**

Adjustable Roundoff Function:

$$\mathrm{Round}(x,n,b) := \mathrm{if}\left(x \cdot 10^n - \mathrm{floor}(x \cdot 10^n) < b, \mathrm{floor}(x \cdot 10^n) \cdot 10^{-n}, \mathrm{ceil}(x \cdot 10^n) \cdot 10^{-n}\right)$$

$pE := \overrightarrow{\mathrm{Round}(pE, 4, .5)} \qquad \sum_i \sum_j pE_{i,j} = 1$ **Roundoff Probabilities, make Sure sum still equals 1**

$MpE_{j,i} := pE_{5-i,j}$ **Each element of the MpE matrix corresponds to the Probability that a neutron has a Q-value and an approximate angle corresponding to the row and column of the Matrix**

$$MpE = \begin{bmatrix} 0.0069 & 0.0304 & 0.0568 & 0.0681 & 0.0516 & 0.0130 \\ 0.0140 & 0.0450 & 0.0588 & 0.0504 & 0.0310 & 0.0085 \\ 0.0135 & 0.0393 & 0.0468 & 0.0426 & 0.0357 & 0.0128 \\ 0.0153 & 0.0444 & 0.0547 & 0.0441 & 0.0280 & 0.0093 \\ 0.0184 & 0.0440 & 0.0462 & 0.0356 & 0.0253 & 0.0095 \end{bmatrix}$$

Within each angular bin, need to dictate shape of distribution

$$M\sigma E_{j,ii} := N\sigma E_{6-ii,j} \qquad \overline{M\sigma E := \mathrm{Round}(M\sigma E,3,.48)} \qquad \sum_{ii} M\sigma E_{j,ii}$$

$$M\sigma E = \begin{bmatrix} 0.05 & 0.105 & 0.144 & 0.197 & 0.212 & 0.211 & 0.081 \\ 0.138 & 0.175 & 0.194 & 0.159 & 0.144 & 0.11 & 0.08 \\ 0.136 & 0.166 & 0.157 & 0.124 & 0.131 & 0.161 & 0.125 \\ 0.161 & 0.181 & 0.183 & 0.145 & 0.12 & 0.11 & 0.1 \\ 0.212 & 0.201 & 0.159 & 0.118 & 0.096 & 0.111 & 0.103 \end{bmatrix} \qquad \begin{matrix} \boxed{1} \\ \boxed{1} \\ \boxed{1} \\ \boxed{1} \\ \boxed{1} \end{matrix}$$

Now, calculate energy as a function of cos(angle).

$Mn := 939.566$
$Md := 1875.613$
$Mb := 9324.439$
$Ed := 1.5$

$$\rho(\phi) := \frac{\sqrt{Mn \cdot Ed \cdot Md}}{Mb + Mn} \cdot \phi \qquad \omega(Q) := \frac{Mb \cdot Q + Ed \cdot (Mb + -Md)}{Mb + Mn}$$

$$\mathrm{Enh}(\phi, Q) := \left(\rho(\phi) + \sqrt{\rho(\phi)^2 + \omega(Q)}\right)^2$$

$$Z_{j,q} := \mathrm{Enh}\left[\phi_{6-q}, \left(Q^T\right)_j\right]$$

Within each bin defined by angle and Q, the energy varies between the corresponding values in the matrix Z:

$$Z = \begin{bmatrix} 1.42 & 1.465 & 1.597 & 1.797 & 2.022 & 2.205 & 2.275 \\ 2.587 & 2.65 & 2.83 & 3.096 & 3.388 & 3.618 & 3.706 \\ 2.927 & 2.994 & 3.186 & 3.469 & 3.777 & 4.019 & 4.111 \\ 3.779 & 3.857 & 4.076 & 4.395 & 4.74 & 5.009 & 5.112 \\ 4.386 & 4.469 & 4.706 & 5.049 & 5.418 & 5.705 & 5.813 \end{bmatrix}$$

C.2 Source Description - 900 kev Deuterons

```
sdef   dir=d1 erg=fdir d2 wgt=10e9 vec=1 0 0 x=0 y=0 z=0  tme=d500
si1    s 010     020     030     040     050     060    $ Q=0.78
         110     120     130     140     150     160    $ Q=2.21
         210     220     230     240     250     260    $ Q=2.62
         310     320     330     340     350     360    $ Q=3.64
         410     420     430     440     450     460    $ Q=4.36
sp1    0.0069  0.0304  0.0568  0.0681  0.0516  0.013  $ Q=0.78
       0.014   0.045   0.0588  0.0504  0.031   0.0085 $ Q=2.21
       0.0135  0.0393  0.0468  0.0426  0.0357  0.0128 $ Q=2.62
       0.0153  0.0444  0.0547  0.0441  0.028   0.0093 $ Q=3.64
       0.0184  0.044   0.0462  0.0356  0.0253  0.0095 $ Q=4.36
ds2    s 015     025     035     045     055     065    $ Q=0.78
         115     125     135     145     155     165    $ Q=2.21
         215     225     235     245     255     265    $ Q=2.62
         315     325     335     345     355     365    $ Q=3.64
         415     425     435     445     455     465    $ Q=4.36
si010 a -1.000 -0.866
sp010    0.05    0.105
si015 a 1.104    1.135
sp015   1 1
si020 a -0.866 -0.500
sp020   0.105    0.144
si025 a 1.135    1.226
sp025   1 1
si030 a -0.500  0.000
sp030   0.144    0.197
si035 a 1.226    1.362
sp035   1 1
si040 a  0.000   0.500
sp040   0.197    0.212
si045 a 1.362    1.513
sp045   1 1
si050 a  0.500   0.866
sp050   0.212    0.211
si055 a 1.513    1.633
sp055   1 1
si060 a  0.866   1.000
sp060   0.211    0.081
si065 a 1.633     1.68
sp065   1 1
si110 a -1.000 -0.866
sp110   0.138    0.175
si115 a 2.29   2.336
sp115   1 1
si120 a -0.866 -0.500
sp120   0.175    0.194
si125 a 2.336    2.468
sp125   1 1
si130 a -0.500  0.000
sp130   0.194    0.159
si135 a 2.468    2.661
sp135   1 1
si140 a  0.000   0.500
sp140   0.159    0.144
si145 a 2.661    2.869
sp145   1 1
si150 a  0.500   0.866
```

```
sp150    0.144    0.11
si155 a 2.869    3.031
sp155    1 1
si160 a  0.866   1.000
sp160    0.11     0.08
si165 a 3.031    3.092
sp165    1 1
si210 a -1.000  -0.866
sp210    0.136   0.166
si215 a 2.635    2.685
sp215    1 1
si220 a -0.866  -0.500
sp220    0.166   0.157
si225 a 2.685    2.827
sp225    1 1
si230 a -0.500   0.000
sp230    0.157   0.124
si235 a 2.827    3.033
sp235    1 1
si240 a  0.000   0.500
sp240    0.124   0.131
si245 a 3.033    3.255
sp245    1 1
si250 a  0.500   0.866
sp250    0.131   0.161
si255 a 3.255    3.427
sp255    1 1
si260 a  0.866   1.000
sp260    0.161   0.125
si265 a 3.427    3.492
sp265    1 1
si310 a -1.000  -0.866
sp310    0.161   0.181
si315 a 3.501    3.559
sp315    1 1
si320 a -0.866  -0.500
sp320    0.181   0.183
si325 a 3.559    3.723
sp325    1 1
si330 a -0.500   0.000
sp330    0.183   0.145
si335 a 3.723     3.96
sp335    1 1
si340 a  0.000   0.500
sp340    0.145   0.12
si345 a 3.96    4.212
sp345    1 1
si350 a  0.500   0.866
sp350    0.12    0.11
si355 a 4.212    4.406
sp355    1 1
si360 a  0.866   1.000
sp360    0.11    0.1
si365 a 4.406    4.479
sp365    1 1
si410 a -1.000  -0.866
sp410    0.212   0.201
si415 a 4.116     4.18
sp415    1 1
si420 a -0.866  -0.500
```

```
sp420   0.201   0.159
si425 a 4.18   4.358
sp425   1 1
si430 a -0.500  0.000
sp430   0.159   0.118
si435 a 4.358   4.614
sp435   1 1
si440 a  0.000  0.500
sp440   0.118   0.096
si445 a 4.614   4.885
sp445   1 1
si450 a  0.500  0.866
sp450   0.096   0.111
si455 a 4.885   5.094
sp455   1 1
si460 a  0.866  1.000
sp460   0.111   0.103
si465 a 5.094   5.172
sp465   1 1
si500 a 0 5000
sp500   1 1
```

C.3 Source Description - 1500 kev Deuterons

```
sdef  dir=d1 erg=fdir d2 wgt=10e9 vec=1 0 0 x=0 y=0 z=0 tme=d500
si1   s 010     020     030     040     050     060    $ Q=0.78
        110     120     130     140     150     160    $ Q=2.21
        210     220     230     240     250     260    $ Q=2.62
        310     320     330     340     350     360    $ Q=3.64
        410     420     430     440     450     460    $ Q=4.36
sp1   0.0122 0.0366 0.0628 0.0689 0.0378 0.0069 $ Q=0.78
      0.0137  0.037 0.0482 0.0527 0.0386 0.0106 $ Q=2.21
      0.0139 0.0435 0.0489 0.0378 0.0366 0.0132 $ Q=2.62
       0.012 0.0345 0.0461  0.047 0.0375 0.0139 $ Q=3.64
      0.0123 0.0366 0.0467  0.044 0.0359  0.014 $ Q=4.36
ds2   s 015     025     035     045     055     065    $ Q=0.78
        115     125     135     145     155     165    $ Q=2.21
        215     225     235     245     255     265    $ Q=2.62
        315     325     335     345     355     365    $ Q=3.64
        415     425     435     445     455     465    $ Q=4.36
si010 a -1.000 -0.866
sp010   0.136   0.137
si015 a  1.42   1.465
sp015   1 1
si020 a -0.866 -0.500
sp020   0.137   0.162
si025 a 1.465   1.597
sp025   1 1
si030 a -0.500  0.000
sp030   0.162   0.213
si035 a 1.597   1.797
sp035   1 1
si040 a  0.000  0.500
sp040   0.213   0.199
si045 a 1.797   2.022
sp045   1 1
si050 a  0.500  0.866
sp050   0.199    0.11
si055 a 2.022   2.205
sp055   1 1
si060 a  0.866  1.000
sp060    0.11  0.044
si065 a 2.205   2.275
sp065   1 1
si110 a -1.000 -0.866
sp110   0.148   0.157
si115 a 2.587    2.65
sp115   1 1
si120 a -0.866 -0.500
sp120   0.157   0.145
si125 a  2.65    2.83
sp125   1 1
si130 a -0.500  0.000
sp130   0.145   0.143
si135 a  2.83   3.096
sp135   1 1
si140 a  0.000  0.500
sp140   0.143   0.172
si145 a 3.096   3.388
sp145   1 1
si150 a  0.500  0.866
```

```
sp150   0.172   0.144
si155 a 3.388   3.618
sp155   1 1
si160 a  0.866  1.000
sp160   0.144   0.092
si165 a 3.618   3.706
sp165   1 1
si210 a -1.000 -0.866
sp210   0.124   0.185
si215 a 2.927   2.994
sp215   1 1
si220 a -0.866 -0.500
sp220   0.185    0.17
si225 a 2.994   3.186
sp225   1 1
si230 a -0.500  0.000
sp230    0.17   0.123
si235 a 3.186   3.469
sp235   1 1
si240 a  0.000  0.500
sp240   0.123   0.103
si245 a 3.469   3.777
sp245   1 1
si250 a  0.500  0.866
sp250   0.103   0.195
si255 a 3.777   4.019
sp255   1 1
si260 a  0.866  1.000
sp260   0.195     0.1
si265 a 4.019   4.111
sp265   1 1
si310 a -1.000 -0.866
sp310   0.128    0.14
si315 a 3.779   3.857
sp315   1 1
si320 a -0.866 -0.500
sp320   0.14   0.142
si325 a 3.857   4.076
sp325   1 1
si330 a -0.500  0.000
sp330   0.142   0.134
si335 a 4.076   4.395
sp335   1 1
si340 a  0.000  0.500
sp340   0.134   0.147
si345 a 4.395    4.74
sp345   1 1
si350 a  0.500  0.866
sp350   0.147   0.159
si355 a  4.74   5.009
sp355   1 1
si360 a  0.866  1.000
sp360   0.159   0.151
si365 a 5.009   5.112
sp365   1 1
si410 a -1.000 -0.866
sp410   0.126   0.147
si415 a 4.386   4.469
sp415   1 1
si420 a -0.866 -0.500
```

```
sp420   0.147   0.151
si425 a 4.469   4.706
sp425   1 1
si430 a -0.500  0.000
sp430   0.151   0.128
si435 a 4.706   5.049
sp435   1 1
si440 a  0.000  0.500
sp440   0.128   0.135
si445 a 5.049   5.418
sp445   1 1
si450 a  0.500  0.866
sp450   0.135   0.158
si455 a 5.418   5.705
sp455   1 1
si460 a  0.866  1.000
sp460   0.158   0.154
si465 a 5.705   5.813
sp465   1 1
si500 a 0 5000
sp500   1 1
```

Appendix D

Results from Moderation Study

This appendix shows the results from the study of intensity verses moderator thickness for the three moderator materials studied: solid methane, water, and polyethelene.

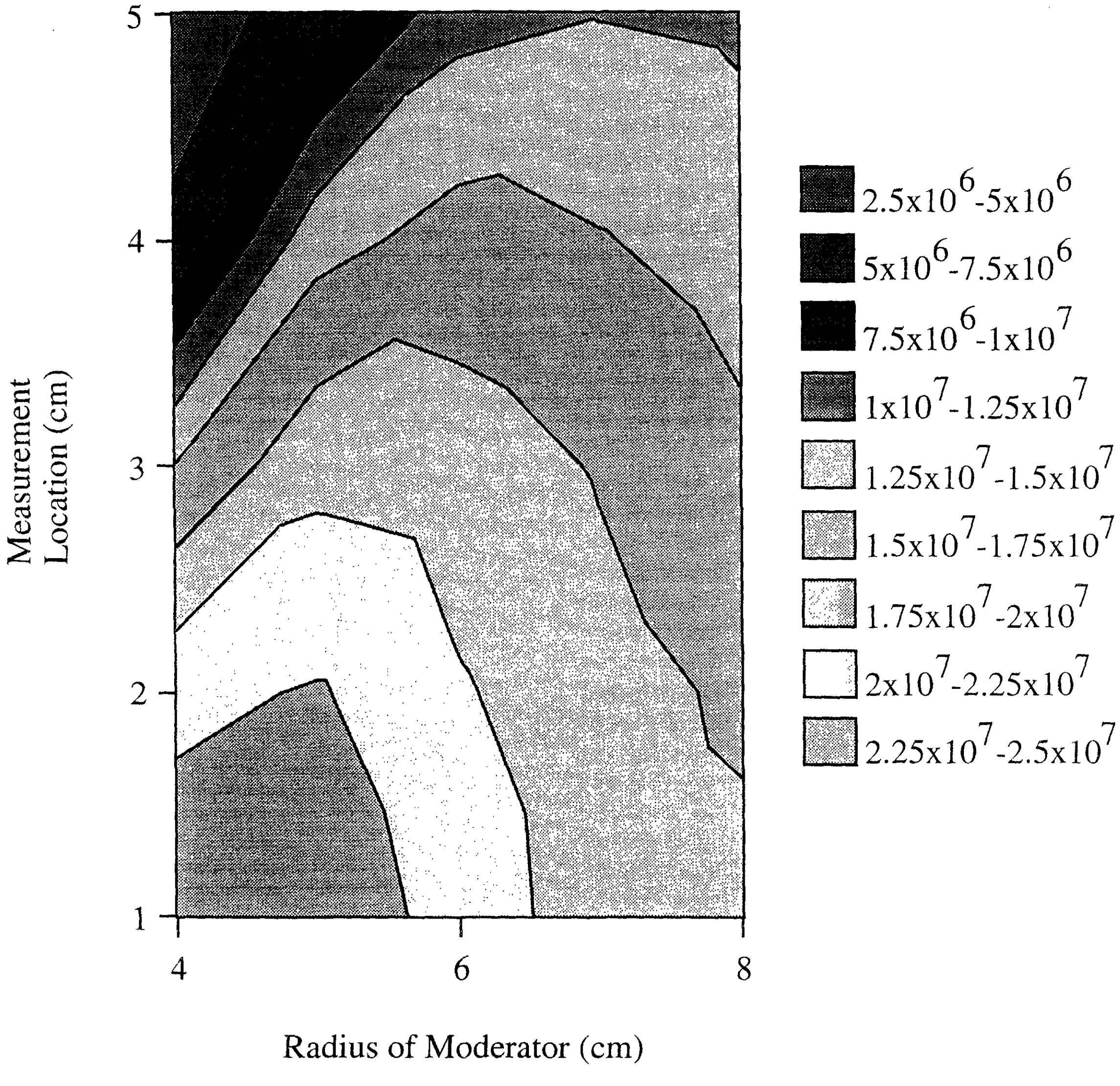

Figure D-1: Effect of varying radius of reflected CH_4 moderator.

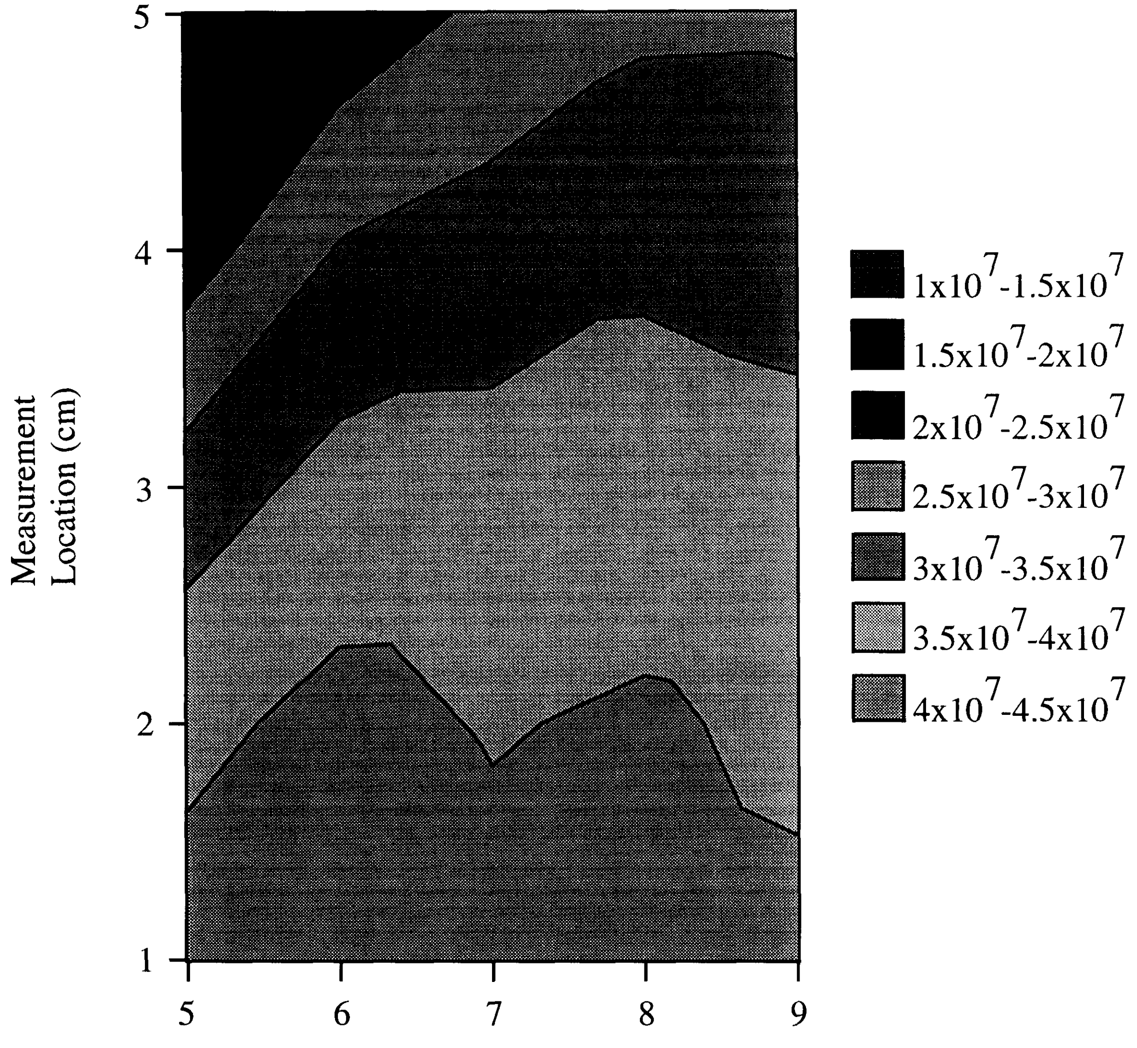

Figure D-2: Effect of varying radius of reflected water moderator.

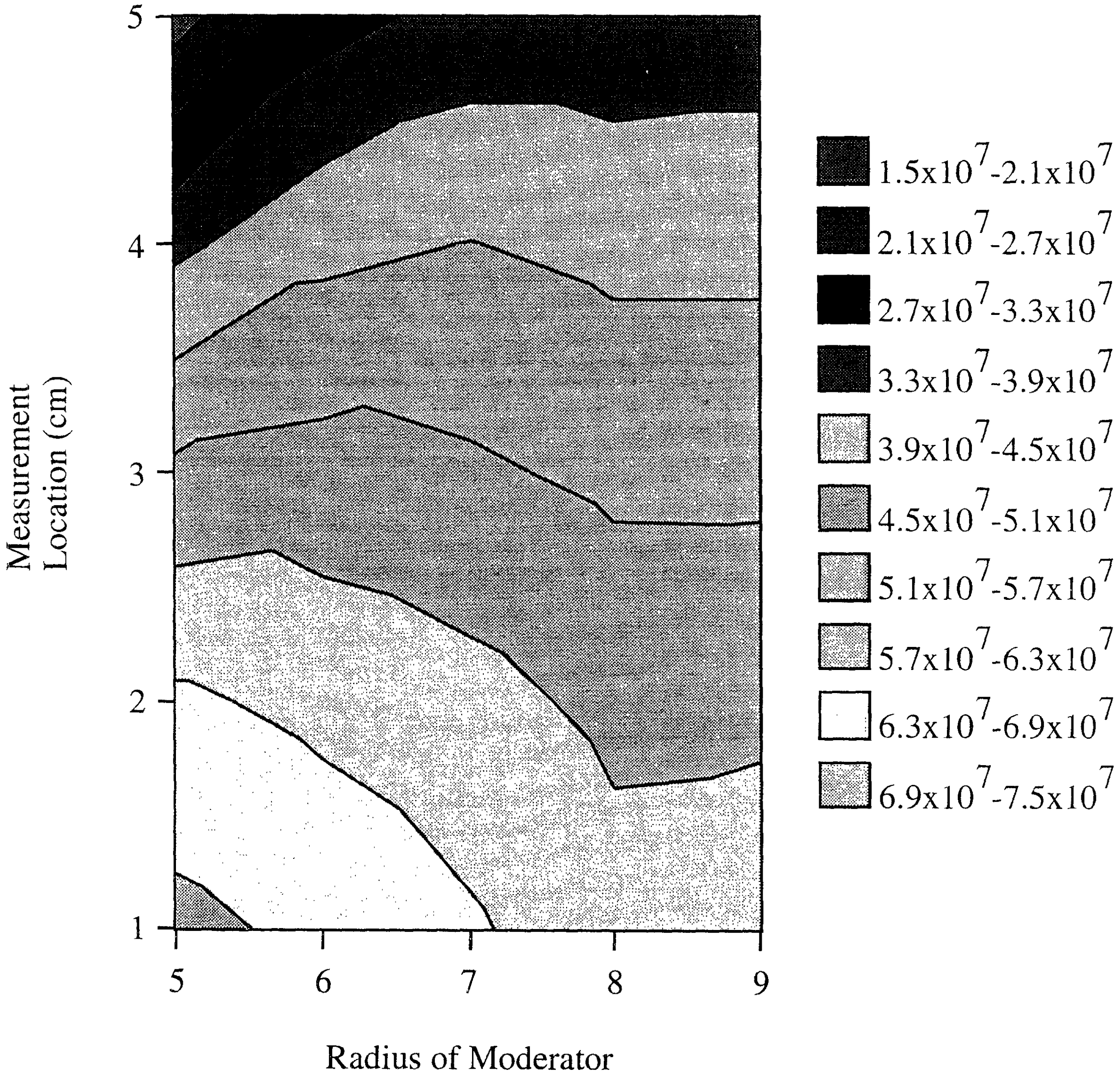

Figure D-3: Effect of varying radius of reflected polyethelene moderator.

Appendix E

Results from Shielding Calculations

The following seven graphs illustrate findings encountered during the shielding design.

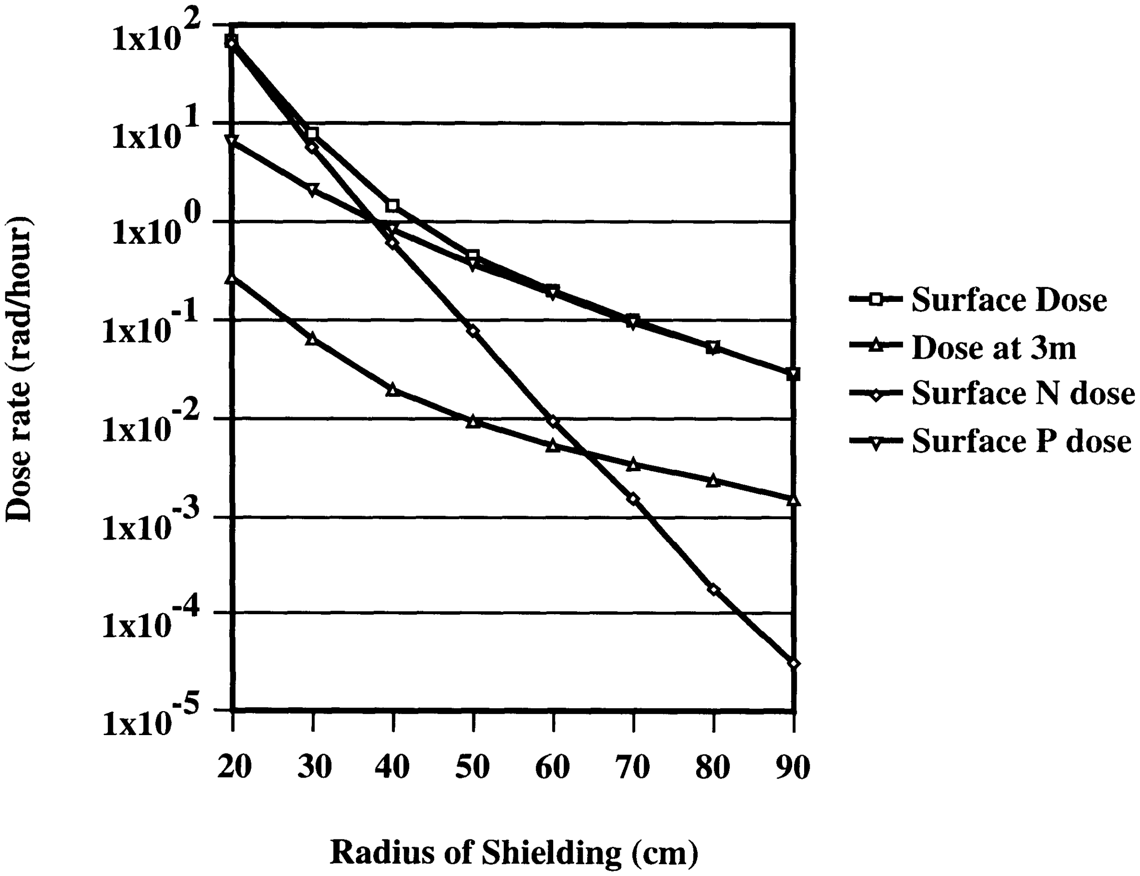

Figure E-1: Dose rate versus thickness of all water shield.

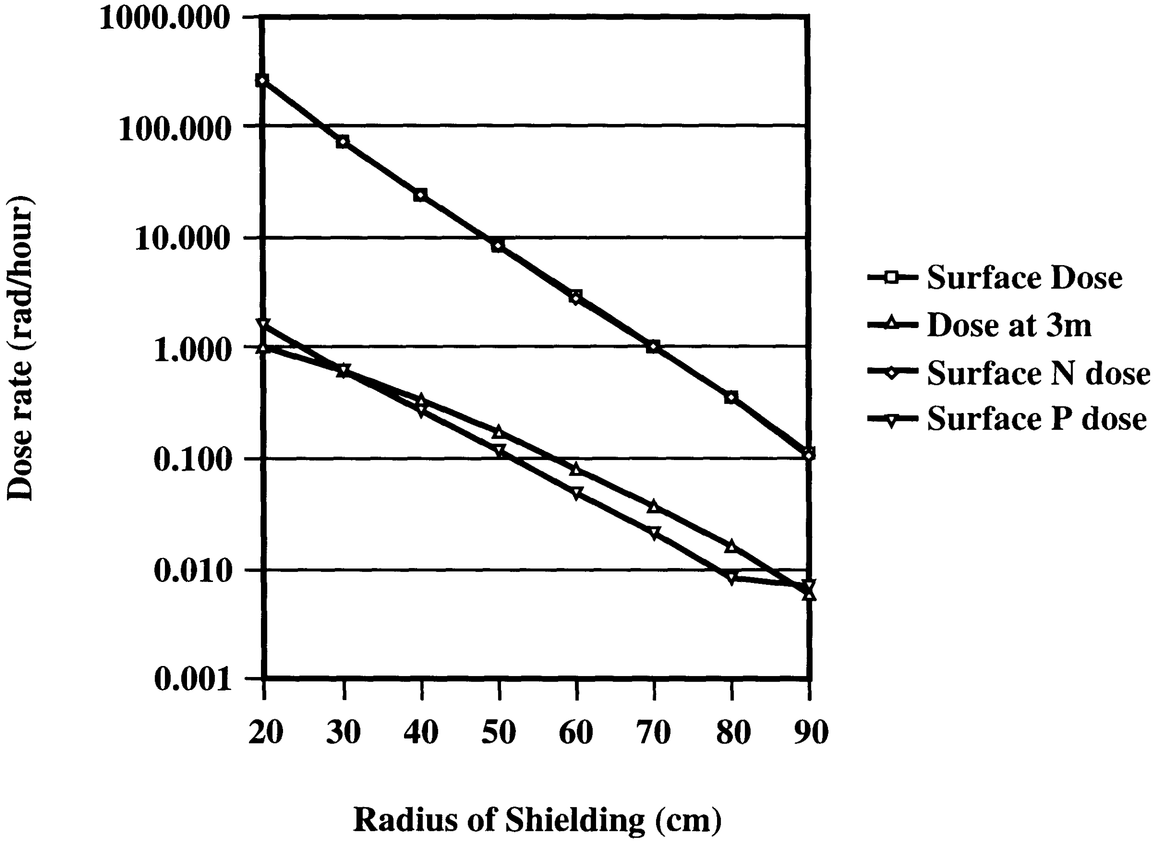

Figure E-2: Dose rate vs thickness for water shield with 1 cm thick Pb layers every 10 cm.

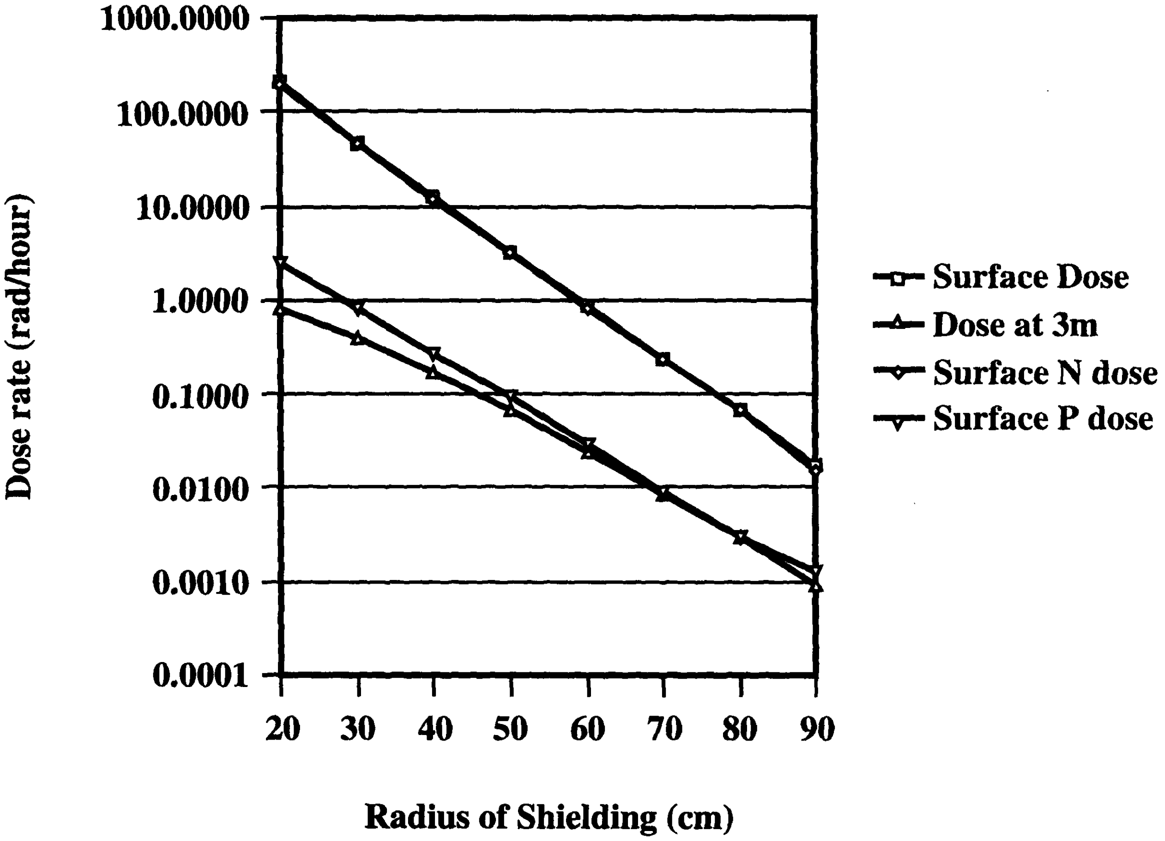

Figure E-3: Dose rate vs thickness for water shield with 2 cm thick Pb layers every 10 cm.

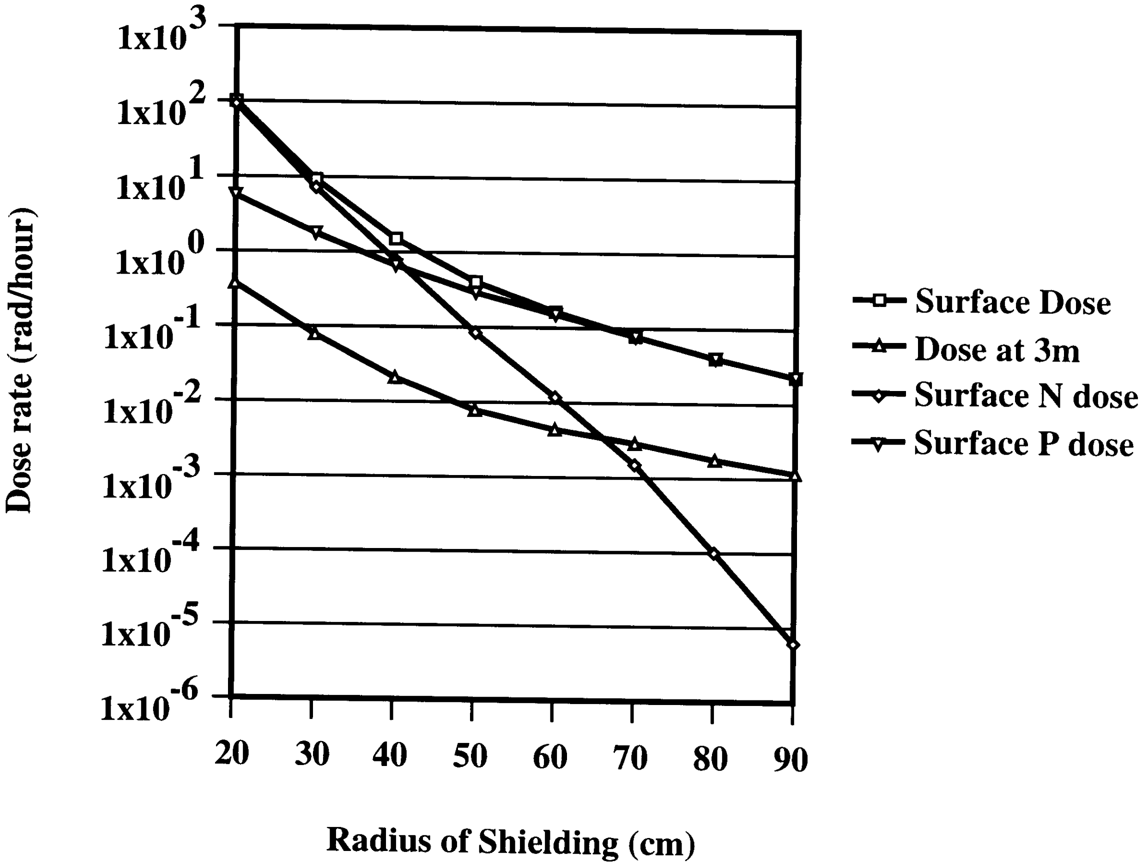

Figure E-4: Dose rate vs thickness for a shield consisting of 3 cm of Pb, followed by water.

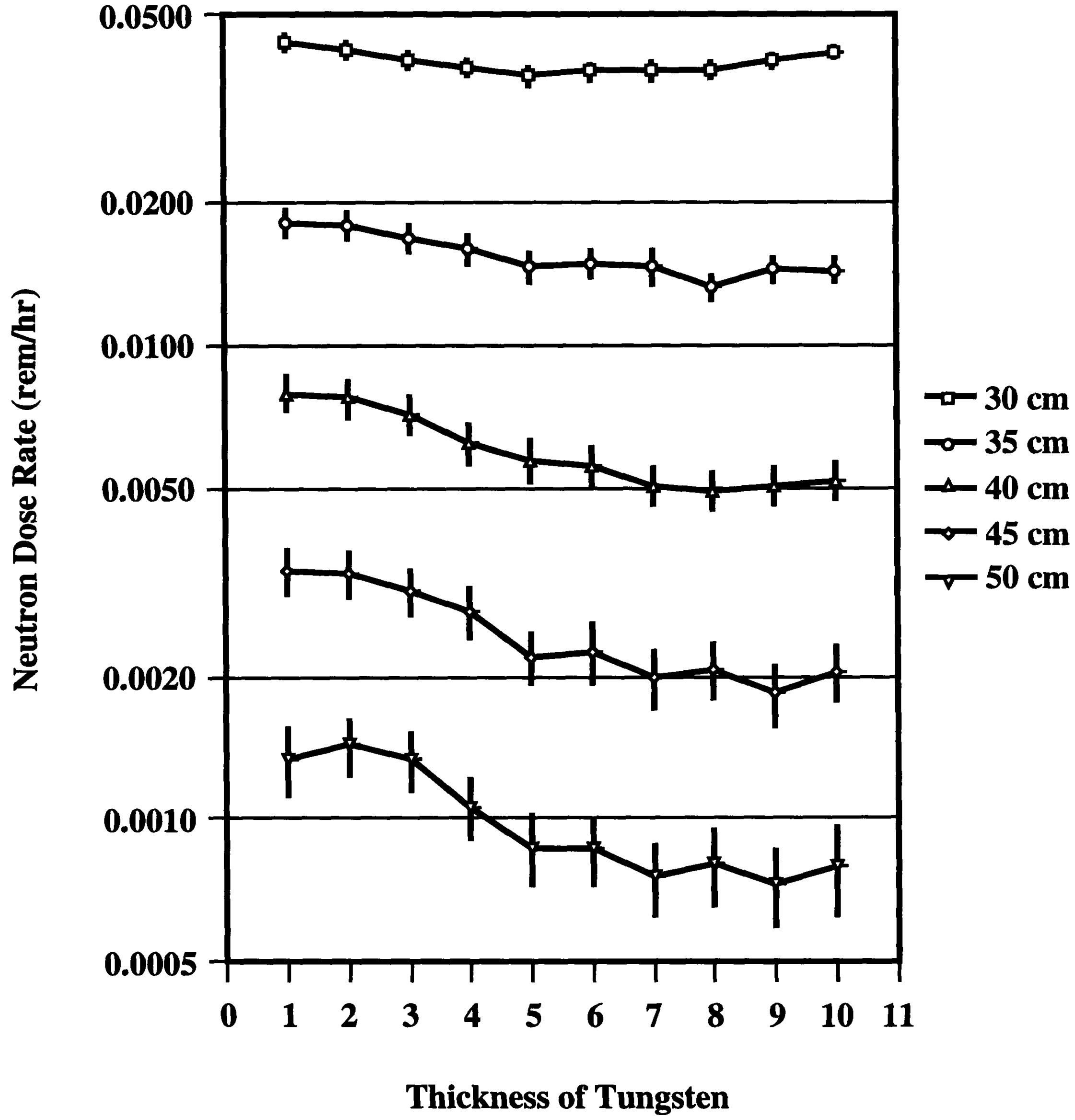

Figure E-5: Dose rate vs inner shield thickness for an inner shield consisting of tungsten.

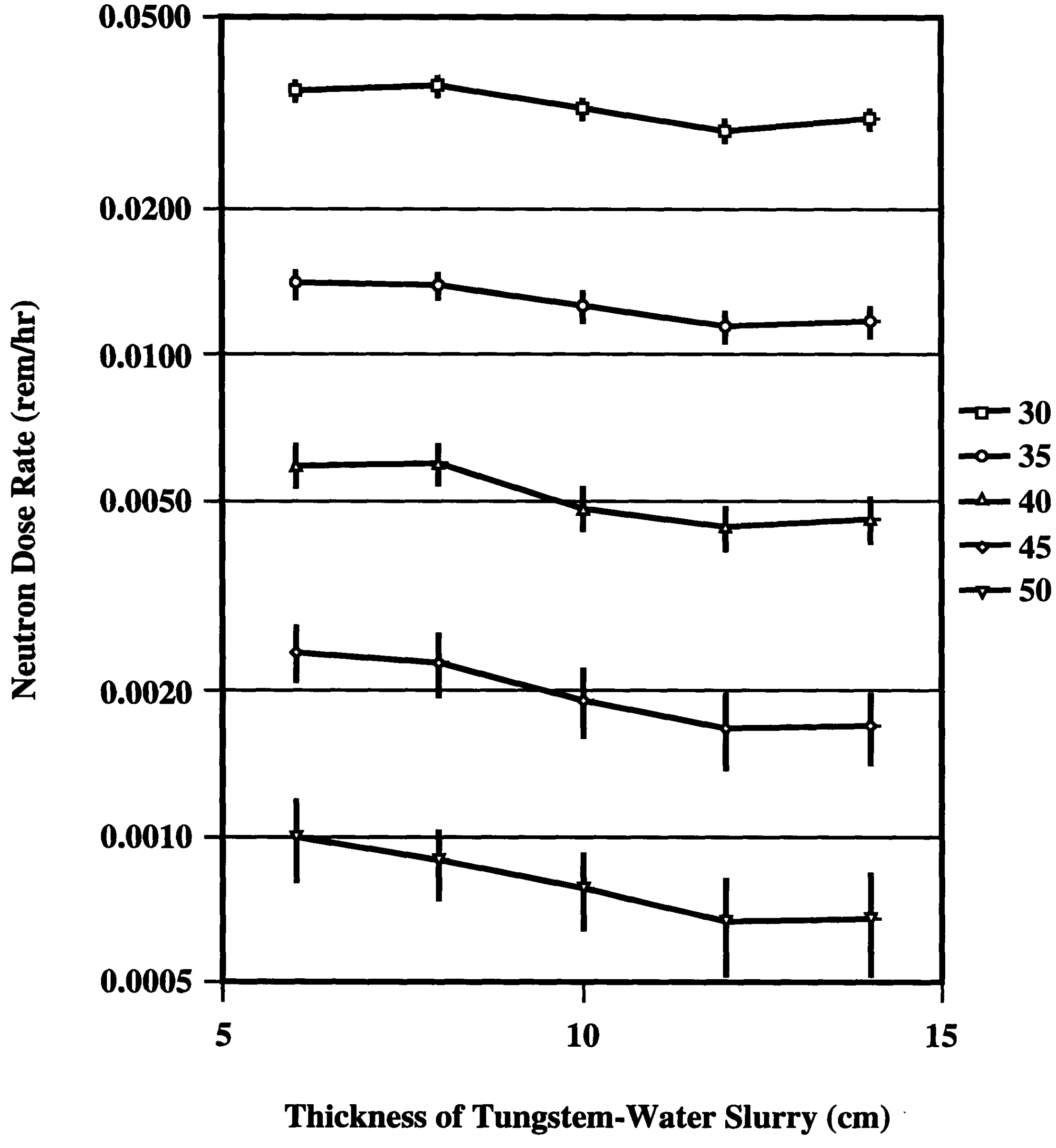

Figure E-6: Dose rate vs inner shield thickness for an inner shield consisting of a tungsten-water slurry.

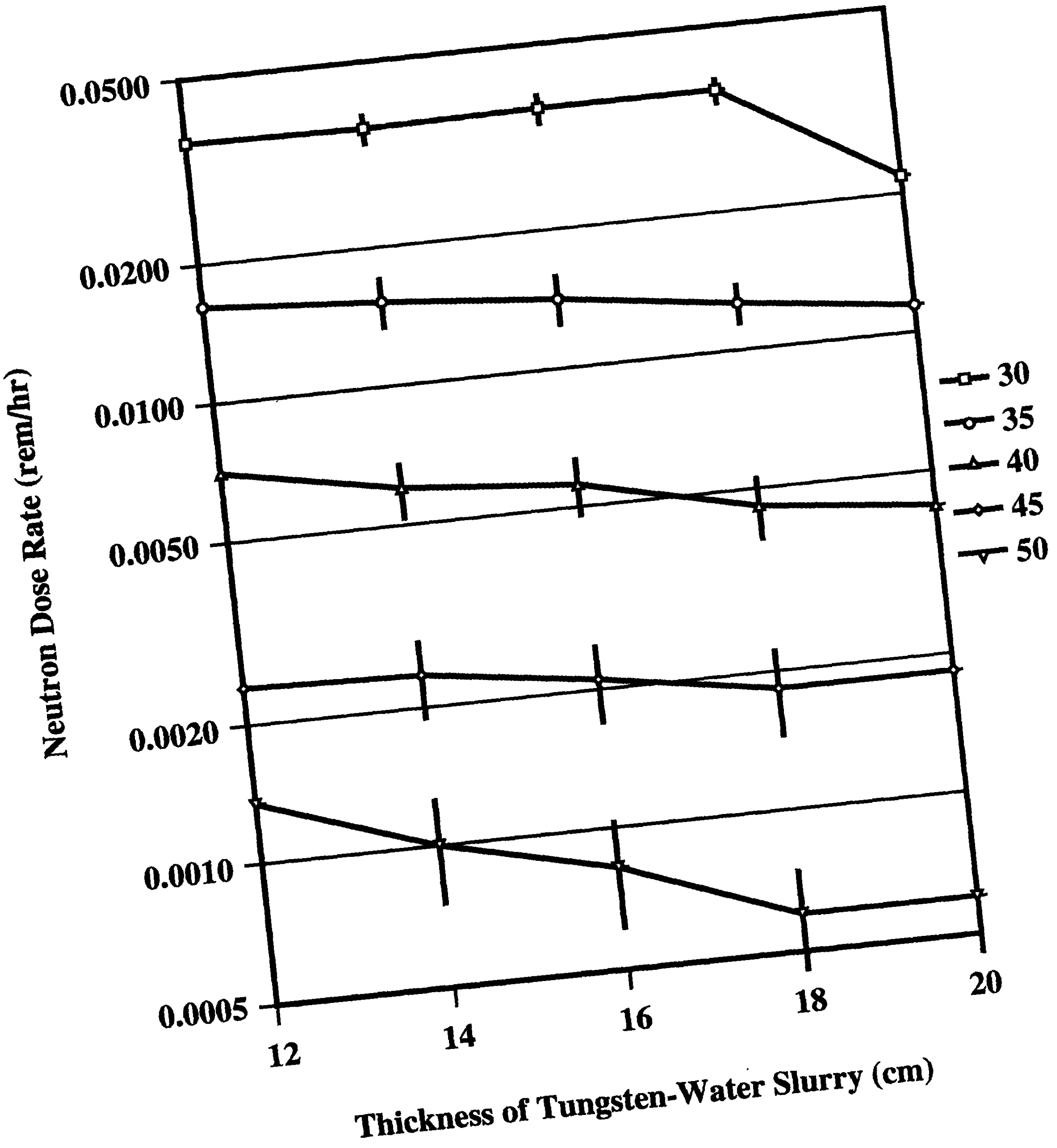

Figure E-7: Dose rate vs inner shield thickness for an inner shield consisting of a tungsten-water slurry, surrounded by a boron-water slurry.

Appendix F

System Evaluation Calculations

The next two sections are the MathCad worksheets used to calculate the time required to determine strains with an accuracy of 10% of the yield strain

The first worksheet (12 pages) simulates the diffraction experiment using a monochromatic neutron beam, assuming a copper monochromator and a polyethelene moderator. The results from the solid methane moderator, and from other monochromators were on the same time scale: several years.

The second worksheet (10 pages) simulates the diffraction experiment using a polychromatic neutron beam, with a pulsed source and time-of-flight detector. This particular worksheet assumes that the polyethelene moderator is used; the solid methane moderator yielded slightly better results (approximately 10but not much better considering the extra effort required of a solid methane moderator.

F.1 Evaluation of System Using A Monochromatic Beam

$A := 10^{-8} \cdot cm$	Define angstroms
$ev := 1.60217733 \cdot 10^{-19} \cdot joule$	Define Energy Units
$Mev := 10^{6} \cdot ev \quad mev := 10^{-3} \cdot ev$	
$h := 6.6260755 \cdot 10^{-34} \cdot joule \cdot sec$	Planck's Constant
$k := 1.380658 \cdot 10^{-23} \cdot \frac{joule}{K}$	Boltzman's Constant
$mn := 1.6749286 \cdot 10^{-27} \cdot kg$	Mass of Neutron
$amu := 1.6605402 \cdot 10^{-27} \cdot kg$	Atomic mass unit
$shake := 10^{-8} \cdot sec \qquad \mu sec := 10^{-6} \cdot sec$	Time Units
$hour := 60 \cdot min \qquad day := 24 \cdot hour$	
$year := 365 \cdot day$	
$pos(x) := x \cdot (x>0 \cdot x)$	Convenient Function

Now read in Energy-vs-Intensity data from MCNP:

$data := READPRN(polynt)$

Fomat of data:

$$\begin{bmatrix} energy_{1} & Flux_{1,1} & Uncert_{1,1} \\ energy_{2} & Flux_{2,1} & Uncert_{2,1} \\ \cdots & \cdots & \cdots \\ energy_{n\lambda} & Flux_{n\lambda,1} & Uncert_{n\lambda,1} \end{bmatrix}$$

Define energy to wavelength, wavelength to energy conversions:

$$\lambda e(E) := \frac{h}{\sqrt{2 \cdot mn \cdot E}} \qquad E\lambda(\lambda) := \frac{h^2}{2 \cdot mn \cdot \lambda^2}$$

Set up column matrix of wavelength values:

$$n\lambda := \mathrm{length}\left(data^{<0>}\right) - i\lambda := 0 .. n\lambda$$

$$\delta\lambda_{i\lambda} := \left| \lambda e\left(data_{n\lambda + 1 - i\lambda, 0} \cdot Mev\right) - \lambda e\left(data_{n\lambda - i\lambda, 0} \cdot Mev\right) \right|$$

$$\lambda_{i\lambda} := \lambda e\left(data_{n\lambda + 1 - i\lambda, 0} \cdot Mev\right) + \frac{\delta\lambda_{i\lambda}}{2}$$

$$\lambda min := \min(\lambda) \qquad \lambda max := \max(\lambda)$$

$$\lambda min = 0.042 \cdot A \qquad \lambda max = 9.127 \cdot A$$

Set up matrices of differential flux and uncertainty values:

$$I0_{i\lambda} := data_{n\lambda + 1 - i\lambda, 1} \cdot \left| \frac{1}{\delta\lambda_{i\lambda}} \right| \cdot \frac{1}{cm^2 \cdot sec} \qquad \sigma I0_{i\lambda} := data_{n\lambda - i\lambda, 2}$$

Normalize flux values

$Int := 3 \cdot 10^7 \cdot cm^{-2} \cdot sec^{-1}$ $\qquad \lambda int := 0.5 \cdot A$

Integrated Differential flux > λint for complicated source

$$IntFlux := \sum_{i\lambda} I0_{i\lambda} \cdot \delta\lambda_{i\lambda} \cdot \left(\lambda_{i\lambda} > \lambda int\right)$$

Integrated Differential flux > λint for simple evaluation source

$$IntFlux = 3.345 \cdot 10^9 \cdot cm^{-2} \cdot sec^{-1}$$

$$Adjust := \frac{Int}{IntFlux} \qquad Adjust = 0.009$$

Must multiply flux values obtained from simple source by "Adjust"

Create spline function to represent intensity vs wavelength

$$vs := \mathrm{cspline}(\lambda, I0) \qquad \mathrm{spline}(\lambda x) := \mathrm{interp}(vs, \lambda, I0, \lambda x) \cdot Adjust$$

Now fit "modified Maxwellian" distribution to data:

$T := 300 \cdot K$	Approximate Spectral Temperature of Maxwellian
$peak := \dfrac{h}{\sqrt{5 \cdot mn \cdot k \cdot T}}$	Guess value for lambda at maximum intensity
$N0 := \dfrac{2}{125} \cdot spline(peak) \cdot \dfrac{h}{\sqrt{mn \cdot k}} \cdot exp\left(\dfrac{5}{2}\right) \cdot \sqrt{\dfrac{5}{T}}$	Guess value of Maxwell intensity constant
$N1 := spline(0.4 \cdot A) \cdot 0.4 \cdot A$	Guess value of 1/lambda intensity constant

Modified Maxwellian function:

$$v0(T,\lambda,N0,N1) := \frac{N0}{2} \cdot \frac{h^4}{mn^2 \cdot k^2 \cdot T^2 \cdot \lambda^5} \cdot exp\left(-\frac{h^2}{2 \cdot mn \cdot k \cdot \lambda^2 \cdot T}\right) + \frac{N1}{\lambda} \cdot exp\left(-\frac{2 \cdot mn \cdot k \cdot \lambda^2 \cdot T}{h^2}\right)$$

Now use Mathcad "Minerr" routine to solve for best (least squares) fit of above constants to modified Maxwellian function:

$$\text{given} \quad \sum_{i\lambda} \frac{\left(\left(\dfrac{v0\left(T,\lambda_{i\lambda},N0,N1\right)}{Adjust} - I0_{i\lambda}\right)\right)^2}{\left(I0_{i\lambda} \cdot \sigma I0_{i\lambda}\right)^2} \quad T>0 \cdot K \quad 1=1 \quad \begin{pmatrix} N0 \\ N1 \\ T \end{pmatrix} := minerr(N0,N1,T)$$

We find: $N0 = 2.81 \cdot 10^7 \cdot \dfrac{1}{cm^2 \cdot sec}$ $N1 = 1.76 \cdot 10^6 \cdot \dfrac{1}{cm^2 \cdot sec}$ $T = 310 \cdot K$

and define:

$$v(\lambda) := \left(\frac{N0}{2} \cdot \frac{h^4}{mn^2 \cdot k^2 \cdot T^2 \cdot \lambda^5} \cdot exp\left(-\frac{h^2}{2 \cdot mn \cdot k \cdot \lambda^2 \cdot T}\right) + \frac{N1}{\lambda} \cdot exp\left(-\frac{2 \cdot mn \cdot k \cdot \lambda^2 \cdot T}{h^2}\right)\right)$$

Look at fit:

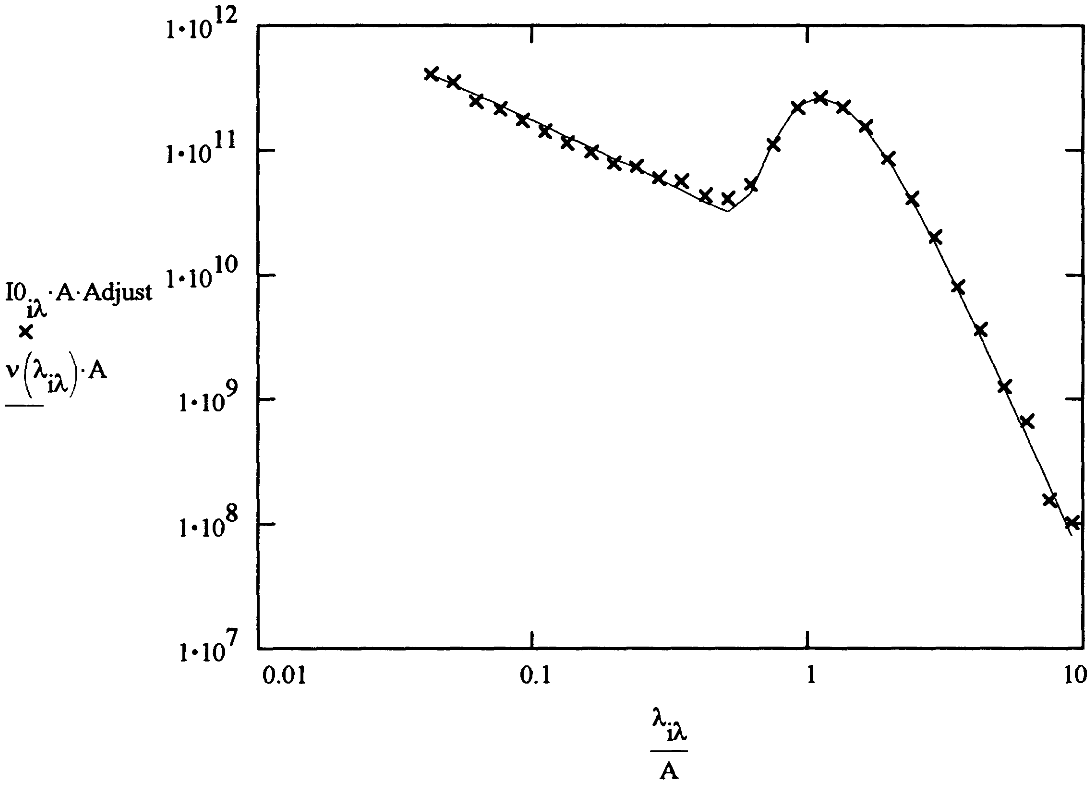

$1 \cdot 10^{12}$
$1 \cdot 10^{11}$
$1 \cdot 10^{10}$
$1 \cdot 10^{9}$
$1 \cdot 10^{8}$
$1 \cdot 10^{7}$
$IO_{i\lambda} \cdot A \cdot Adjust$
×
$\nu(\lambda_{i\lambda}) \cdot A$
0.01
0.1
1
10
$\frac{\lambda_{i\lambda}}{A}$

Monochromator Characterization (FCC Copper):

Atom positions in various Cubic Matrices:

Simple Cubic **Body Centered Cubic** **Face Centered Cubic**

$$\mathrm{pSIM} := \begin{pmatrix} 0 \\ 0 \\ 0 \end{pmatrix} \qquad \mathrm{pBCC} := \begin{pmatrix} 0 & 0.5 \\ 0 & 0.5 \\ 0 & 0.5 \end{pmatrix} \qquad \mathrm{pFCC} := \begin{pmatrix} 0 & 0.5 & 0.5 & 0 \\ 0 & 0.5 & 0 & 0.5 \\ 0 & 0 & 0.5 & 0.5 \end{pmatrix}$$

$$\mathrm{pDIA} := \begin{pmatrix} 0 & 0.5 & 0.5 & 0 & 0.75 & 0.25 & 0.25 & 0.75 \\ 0 & 0.5 & 0 & 0.5 & 0.75 & 0.25 & 0.75 & 0.25 \\ 0 & 0 & 0.5 & 0.5 & 0.75 & 0.75 & 0.25 & 0.25 \end{pmatrix}$$

Diamond Cubic

$\mathrm{pm} := \mathrm{pFCC}$	Structure of Monochromator
$\mathrm{dm0} := 3.6150 \cdot \mathrm{A}$	Cell edge Length
$\mathrm{bm} := 7.7718 \cdot 10^{-15} \cdot \mathrm{m}$	Scattering Length
$\sigma\mathrm{im} := 0.7 \cdot 10^{-24} \cdot \mathrm{cm}^2$	Incoherent Cross Section
$\sigma\mathrm{am} := 3.8 \cdot 10^{-24} \cdot \mathrm{cm}^2$	Absorption Cross Section
$\mathrm{mam} := 63.50 \cdot \mathrm{amu}$	Mass of Atom
$\Theta\mathrm{m} := 320 \cdot \mathrm{K}$	Debye Temperature
$\mathrm{Tm} := 293 \cdot \mathrm{K}$	Temperature
$\mathrm{hklm} := \begin{pmatrix} 1 \\ 1 \\ 1 \end{pmatrix}$	Reflection Used
$\mathrm{dm} := \mathrm{dm0} \cdot \sqrt{(\mathrm{hklm} \cdot \mathrm{hklm})^{-1}}$	Plane spacing of given reflection
$\theta\mathrm{mmin} := 5 \cdot \mathrm{deg}$ $\theta\mathrm{mmax} := 45 \cdot \mathrm{deg}$	Range of Theta to be examined

$$nm := \mathrm{length}\left[\left(pm^{T}\right)^{<0>}\right]$$

Atoms / unit cell

$$Ncm := \frac{1}{dm0^{3}}$$

Cells / unit volume

$$\mu m := \left(4\cdot\pi\cdot bm^{2} + \sigma im + \sigma am\right)\cdot Ncm\cdot nm$$

Linear Absorption Coefficient

$$Wm := \frac{6\cdot h^{2}}{\Theta m^{2}\cdot mam\cdot k}\cdot\frac{Tm}{4\cdot dm^{2}}\cdot\left(1 + \frac{\Theta m^{2}}{36\cdot Tm^{2}} - \frac{\Theta m^{4}}{3600\cdot Tm^{4}}\right)$$

Debrye-Waller factor

$$ipm := 0\,..\,nm - 1$$

$$Fm := \left|\sum_{ipm} bm\cdot\exp\left(2\cdot i\ \cdot\pi\cdot hklm\cdot pm^{<ipm>}\right)\right|\cdot\exp(-Wm)$$

Structure factor for reflection

$$\frac{Fm}{bm}\cdot\exp(Wm) = 4$$

Relative value of structure Factor.

Set up an array of possible scattering angles

$$n\theta m := \mathrm{floor}\left[(\theta mmax - \theta mmin)\cdot deg^{-1} + 0.5\right] \quad i\theta m := 0\,..\,n\theta m$$

$$d\theta m := \frac{\theta mmax - \theta mmin}{n\theta m} \quad \theta m_{i\theta m} := \theta mmin + \frac{\theta mmax - \theta mmin}{n\theta m}\cdot i\theta m$$

$$\lambda m := \overrightarrow{2\cdot dm\cdot\sin(\theta m)}$$

Define reflection functions for a crystal of thickness t0, at angle θ, reflectivity Q, linear absorption coefficient μ, and mosaic spread η

$$a(Q,\mu,\eta,\Delta) := \frac{Q}{\mu}\cdot\left(\frac{1}{\eta\cdot\sqrt{2\cdot\pi}}\cdot\exp\left(\frac{-1}{2}\cdot\frac{\Delta^{2}}{\eta^{2}}\right)\right)$$

$$R(t0,\theta,Q,\mu,\eta) := \int_{-\eta\cdot 5}^{\eta\cdot 5}\frac{a(Q,\mu,\eta,\Delta)}{1 + a(Q,\mu,\eta,\Delta)\ \ldots + \sqrt{1 + 2\cdot a(Q,\mu,\eta,\Delta)}\cdot\coth\left(\frac{\mu\cdot t0}{\sin(\theta)}\cdot\sqrt{1 + 2\cdot a(Q,\mu,\eta,\Delta)}\right)}\,d\Delta$$

Define function to determine Q value for a reflection:

$$Q(\lambda,\mathrm{Nc},\theta,F) := \frac{\lambda^{3}\cdot \mathrm{Nc}^{2}}{\sin(\theta\cdot 2)}\cdot F^{2}$$

Define function to account for intensity change due to collination and mosaic spread of monochromator:

$$\theta\mathrm{int}(\eta m,\theta,\alpha 0,\alpha 1,\beta 0,\beta 1) := \frac{\alpha 0\cdot \alpha 1\cdot \eta m}{\sqrt{\alpha 0^{2}+\alpha 1^{2}+4\cdot \eta m^{2}}}\cdot\frac{\beta 0\cdot \beta 1}{\sqrt{\beta 0^{2}+\beta 1^{2}+4\cdot \sin(\theta)^{2}\cdot \eta m^{2}}}$$

Flux getting through monochromator to sample:

$$\Phi 1(\lambda,\theta,t0,\mu m,\eta m,\alpha 0,\alpha 1,\beta 0,\beta 1) := \frac{\frac{\nu(\lambda)}{2\cdot \pi}\cdot \lambda\cdot \cot(\theta)\cdot \theta\mathrm{int}(\eta m,\theta,\alpha 0,\alpha 1,\beta 0,\beta 1)}{R(t0,\theta,Q(\lambda,\mathrm{Ncm},\theta,\mathrm{Fm}),\mu m,\eta m)^{-1}}$$

Uncertainty in angle due to monochromator & collimators:

$$\sigma\Theta(\alpha 0,\alpha 1,\eta m) := \sqrt{\frac{\alpha 0^{2}\cdot \eta m^{2}+\alpha 1^{2}\cdot \eta m^{2}+\alpha 0^{2}\cdot \alpha 1^{2}}{\alpha 0^{2}+\alpha 1^{2}+4\cdot \eta m^{2}}}$$

Now, Deal with the sample (BCC Iron)

$p := \mathrm{pBCC}$	Structure of sample
$d0 := 2.8663\cdot A$	Cell edge Length
$b := 9.54\cdot 10^{-15}\cdot m$	Scattering Length
$\sigma i := 0.39\cdot 10^{-24}\cdot cm^{2}$	Incoherent Cross Section
$\sigma a := 2.56\cdot 10^{-24}\cdot cm^{2}$	Absorption Cross Section
$ma := 55.85\cdot amu$	Mass of Atom
$\Theta := 411\cdot K$	Debye Temperature
$T := 293\cdot K$	Temperature

$tin := 1 \cdot cm$ Thickness of specimen traversed by beam entering sample

$tout := 1 \cdot cm$ Thickness of specimen traversed by beam exiting sample

$Vol := (1 \cdot cm)^3$ Volume of observed region

$n := \mathrm{length}\left[\left(p^{T}\right)^{<0>}\right]$ # Atoms / unit cell

$Nc := d0^{-3}$ # Cells / unit volume

$\mu := \left(4 \cdot \pi \cdot b^2 + \sigma i + \sigma a\right) \cdot Nc \cdot n$ Linear Absorption Coeff.

$\theta min := \frac{\pi}{8} \qquad \theta max := 3 \cdot \frac{\pi}{8}$ Measuring range of θ for neutrons scattered from sample

$\phi 1 := -\frac{\pi}{2} \quad \phi 2 := \frac{\pi}{2}$ Measuring range of ϕ for neutrons scattered from sample

$\lambda min := \min(\lambda m)$ Define expected range of wavelengths

$\lambda max := \max(\lambda m)$

$dmin := \frac{1}{2} \cdot \frac{\lambda min}{\sin(\theta max)}$ Define applicable range of d's

$dmax := \frac{1}{2} \cdot \frac{\lambda max}{\sin(\theta min)}$

nr is the ratio of max to min r values under consideration (maximum value=30)

$nr := \min\left(\left(\mathrm{ceil}\left(\frac{2 \cdot d0}{\lambda min}\right) \quad 30\right)\right) \qquad ir := 1 .. nr \qquad jr := 1 .. nr \qquad maxr := \frac{2 \cdot \pi}{d0} \cdot nr$

$Nr := \sum_{ir} \left[\sum_{jr} (jr + 1) \cdot (jr \le ir) + 1\right]$ Nr is the number of plane families that could exist between the min and max r values

Calculate all variations of HKL

$hh_0 := 1 \quad kk_0 := 0 \quad ll_0 := 0 \qquad ii := 1..Nr \qquad jj := 0..Nr$

$$\begin{bmatrix} hh_{ii} \\ kk_{ii} \\ ll_{ii} \end{bmatrix} := \begin{bmatrix} hh_{ii-1} + \left(hh_{ii-1} = ll_{ii-1}\right) \\ \left[kk_{ii-1} + \left(kk_{ii-1} = ll_{ii-1}\right)\right]\cdot\left(hh_{ii-1} \neq ll_{ii-1}\right) \\ \left[ll_{ii-1} + \left(kk_{ii-1} \neq ll_{ii-1}\right)\right]\cdot\left(kk_{ii-1} \neq ll_{ii-1}\right) \end{bmatrix}$$

$hkl := \mathrm{augment}(hh, \mathrm{augment}(kk, ll))^T$

$$m0 := \overrightarrow{\frac{48}{\left[2^{((hh=kk)+(kk=ll)+(kk=0)+(ll=0))} + 2\cdot(hh=ll)\right]}}$$

Calculate multiplicity of planes

$$r_{jj} := \frac{\sqrt{\left(hh_{jj}\right)^2 + \left(kk_{jj}\right)^2 + \left(ll_{jj}\right)^2}}{d0} \qquad d0 := \overrightarrow{\frac{1}{r}}$$

Calculate reciprocal and real lattice spacings

$$W_{jj} := \frac{6\cdot h^2}{\Theta^2\cdot k\cdot ma}\cdot\frac{T}{4\cdot\left(d0_{jj}\right)^2}\cdot\left(1 + \frac{\Theta^2}{36\cdot T^2} - \frac{\Theta^4}{3600\cdot T^4}\right)$$

Debrye-Waller factor

$i := 0..n-1$

$$F0_{jj} := \left|\sum_i b\cdot\exp\left(2\cdot i\cdot\pi\cdot hkl^{<jj>}\cdot p^{<i>}\right)\right|\cdot\exp\left(-W_{jj}\right)$$

Structure factor for reflection

To save time, the planes are sorted, so that only those which are expected to diffract with a large intensity are evaluated further:

$$int_{jj} := m0_{jj}\cdot\left(F0_{jj}\right)^2\cdot\left(d0_{jj}\right)^3$$

Make intensity estimate

Make matrix, for sorting:

$sortmat := \mathrm{augment}\left(\mathrm{augment}\left(int\cdot A^{-4}, m0\cdot A\right), \mathrm{augment}(F0, d0)\right)$

$sortout := \mathrm{csort}(sortmat, 0)$

Do the sort

$nhkl := 20 \quad hk := 0..nhkl-1 \quad d_{hk} := sortout_{Nr-hk,3}$

$F_{hk} := sortout_{Nr-hk,2} \qquad m_{hk} := sortout_{Nr-hk,1}\cdot A^{-1}$

Retreive values of sorted variables

The following values can be varied to optimize the output for a given monochromating crystal and monochromating plane:

$t0 := 0.2\cdot cm$ Thickness of Monochromator

$\eta m := .3\cdot deg$ Mosaic spread

$n\phi := 32 \qquad n\theta := 128$ # of Detectors for measuring ϕ and θ

$$d\theta := \frac{\theta max - \theta min}{n\theta} \qquad d\phi := \frac{\phi 2 - \phi 1}{n\phi}$$

$l0 := 50\cdot cm \qquad ww := 7\cdot cm$ Length of primary collimator, widest width of collimator

$ws := 1\cdot cm \qquad ds := 10\cdot cm$ Sample width, distance from end of collimation to sample location

$tmin := 0.01\cdot cm$ Minimum thickness of collimator

$r2 := 10\cdot cm \qquad l2 := .6\cdot cm$ Radial and side length of detector collimators

$r2\cdot d\theta = 0.614\cdot mm$ Width of Detector Collimators

$\alpha 0 := \dfrac{ww}{l0 + ds} \qquad \beta 0 := \alpha 0$ Primary collimation

$\alpha 2 := d\theta\cdot\dfrac{r2}{l2}\cdot\dfrac{0.87\cdot\sqrt{2\cdot\pi}}{\sin\left(\dfrac{\pi}{2}\cdot\dfrac{l2}{r2}\right) + 2} \qquad \beta 2 := \dfrac{ws}{r2}$ Detector collimation, virtual collimation.

$\dfrac{\alpha 2\cdot r2}{ws} = 1.065$ This value should be about 1 ... May need to adjust value of l2

$\eta d := 5\cdot\%$ Detector Efficiency

$\eta c := \dfrac{r2\cdot d\theta - tmin}{r2\cdot d\theta}$ Fraction accounts for decrease in intensity due to collimator wall thickness

$\alpha 1 := \alpha 0 \quad \beta 1 := \beta 0$ Monochromator ratios

$\sigma\theta 0 := \sigma\Theta(\alpha 0, \alpha 1, \eta m)$

$\sigma\phi 0 := \sigma\Theta(\beta 0, \beta 1, \eta m)$

Determine Uncertainty in angle due to monochromator & collimators

$\sigma\theta d := \dfrac{\alpha 2\cdot d\theta}{\sqrt{2\cdot\pi}} \qquad \sigma\phi d := \dfrac{\beta 2}{\sqrt{2\cdot\pi}}$ Determine Uncertainty in angle due to detector collimators

Now, the Diffraction process in the sample is modeled:

Function to determine fraction of flux converted to diffracted intensity:

$$I2(hkl,\lambda) := \frac{1}{2}\cdot m_{hkl}\cdot\left(F_{hkl}\right)^2\cdot Vol\cdot Nc^2\cdot\lambda^2\cdot d_{hkl}\cdot\frac{\alpha2}{d\theta}\cdot\frac{d\phi}{2\cdot\pi}\cdot\frac{1}{\eta d\cdot\eta c}\cdot\exp(-\mu\cdot(tin+tout))$$

Determine flux of beam exiting monochromator:

$$K1_{i\theta m} := \Phi1\left(\lambda m_{i\theta m},\operatorname{asin}\left(\frac{1}{2}\cdot\frac{\lambda m_{i\theta m}}{dm}\right),t0,\mu m,\eta m,\alpha0,\alpha1,\beta0,\beta1\right)$$

Determine intensity diffracted into each detector:

$$K2_{i\theta m,hk} := \left(\lambda m_{i\theta m}<2\cdot\sin(\theta max)\cdot d_{hk}\right)\cdot\left(\lambda m_{i\theta m}>2\cdot\sin(\theta min)\cdot d_{hk}\right)\cdot I2\left(hk,\lambda m_{i\theta m}\right)\cdot K1_{i\theta m}$$

Determine the incoherent background flux at each detector:

$$Inc_{i\theta m} := K1_{i\theta m}\cdot\exp(-\mu\cdot(tin+tout))\cdot\left(\frac{\alpha2\cdot d\phi}{d\theta\cdot2\cdot\pi}\cdot Vol\cdot Nc\cdot n\cdot\sigma i\right)\cdot\frac{1}{\eta d\cdot\eta c}$$

Set up array of ϕ values:

$$i\phi := 0..n\phi-1 \qquad \phi_{i\phi} := \phi1+d\phi\cdot\left(i\phi+\frac{1}{2}\right)$$

Determine which values of θm result in useable neutrons:

$$U_{i\theta m} := \sum_{hk}\left(K2_{i\theta m,hk}>\frac{0}{sec}\right)$$

Function for calculating uncertainty in angle:

$$\sigma\theta(\theta,\phi,\theta m) := \sqrt{\sigma\theta0^2+\sigma\theta d^2+\left(\left|\tan(\theta)\cdot\cot(\theta m)-\cos(\phi)\right|\cdot\sigma\theta0+\sin(\phi)^2\cdot\sigma\phi0\right)^2}$$

Functions for evaluating strain uncertainties, adapted from equations 2.19 & 2.22.

$x(\phi,\theta) := \cos(\phi)\cdot\sin(\theta\cdot 2) \qquad y(\phi,\theta) := \sin(\phi)\cdot\sin(\theta\cdot 2) \qquad z(\theta) := \cos(\theta\cdot 2) - 1$

$$AA(\theta,\phi) := \begin{bmatrix} x(\phi,\theta)^2 \\ y(\phi,\theta)^2 \\ z(\theta)^2 \\ x(\phi,\theta)\cdot y(\phi,\theta) \\ y(\phi,\theta)\cdot z(\theta) \\ z(\theta)\cdot x(\phi,\theta) \end{bmatrix} \cdot \begin{bmatrix} x(\phi,\theta)^2 \\ y(\phi,\theta)^2 \\ z(\theta)^2 \\ x(\phi,\theta)\cdot y(\phi,\theta) \\ y(\phi,\theta)\cdot z(\theta) \\ z(\theta)\cdot x(\phi,\theta) \end{bmatrix}^T$$

L value per unit time:

$$L(\theta,\phi,\theta m,KK,Inc) := \frac{64\cdot\sin(\theta)^4\cdot\cot(\theta m)^2\cdot\sigma\theta 0 + 16\cdot\sin(2\cdot\theta)^2\cdot\sigma\theta(\theta,\phi,\theta m)^2}{KK^2\cdot(KK + 7.5\cdot Inc)^{-1}}$$

$$PhiSum(\lambda m,d,\theta m,K2,Inc) := \left(K2 > \frac{0}{sec}\right)\cdot\sum_{i\phi}\frac{AA\left(asin\left(\frac{\lambda m}{2\cdot d}\right),\phi_{i\phi}\right)}{L\left(asin\left(\frac{\lambda m}{2\cdot d}\right),\phi_{i\phi},\theta m,K2,Inc\right)}$$

Determine σ, rms value of uncertainty in strain components per unit time$^{1/2}$

$$\sigma_{i\theta m} := \left(U_{i\theta m} > 1\right)\cdot\sqrt{\frac{1}{6}\cdot tr\left[\left(\sum_{hk} PhiSum\left(\lambda m_{i\theta m}, d_{hk}, \theta m_{i\theta m}, K2_{i\theta m,hk}, Inc_{i\theta m}\right)\right)^{-1}\right]}$$

$$\sigma_{i\theta m} := \sigma_{i\theta m} + \left(U_{i\theta m} < 2\right)\cdot\sqrt{10^{10}\cdot sec}$$

Neutron wavelength and monorchromator scattering angle resulting in minimum uncertainty:

$$csort\left(augment\left(\frac{\sigma\cdot A}{\sqrt{sec}},\lambda m\right),0\right)_{0,1} = 2.15\cdot A \qquad csort\left(augment\left(\frac{\sigma}{\sqrt{sec}},\theta m\right),0\right)_{0,1} = 31\cdot deg$$

Time required to resolve 10% of yield strain: $\left(\frac{\min(\sigma)}{0.02\cdot\%}\right)^2 = 9\cdot year$ Time required at 100 x the intensity: $\left(\frac{\min(\sigma)}{0.02\cdot\%}\right)^2\cdot\frac{1}{100} = 32.616\cdot day$

F.2 Evaluation of System Using Time-of-Flight Measurements

$A := 10^{-8}\cdot cm$	Define angstroms
$ev := 1.60217733\cdot 10^{-19}\cdot joule$	Define Energy Units
$Mev := 10^{6}\cdot ev\,mev := 10^{-3}\cdot ev$	
$h := 6.6260755\cdot 10^{-34}\cdot joule\cdot sec$	Planck's Constant
$k := 1.380658\cdot 10^{-23}\cdot \frac{joule}{K}$	Boltzman's Constant
$mn := 1.6749286\cdot 10^{-27}\cdot kg$	Mass of Neutron
$amu := 1.6605402\cdot 10^{-27}\cdot kg$	Atomic mass unit
$shake := 10^{-8}\cdot sec \quad \mu sec := 10^{-6}\cdot sec$	Time Units
$hour := 60\cdot min \quad day := 24\cdot hour$	
$year := 365\cdot day$	
$pos(x) := x\cdot(x>0)$	Convenient Function

Now read in Energy & Time -vs- Intensity data from MCNP:

$data := READPRN(poly)$

Fomat of data:

$$\begin{bmatrix} 0 & time_1 & 0 & \ldots & time_{nt} & 0 \\ energy_1 & Flux_{1,1} & Uncert_{1,1} & \ldots & Flux_{1,nt} & Uncert_{1,nt} \\ energy_2 & Flux_{2,1} & Uncert_{2,1} & \ldots & Flux_{2,nt} & Uncert_{2,nt} \\ \ldots & \ldots & \ldots & \ldots & \ldots & \ldots \\ energy_{n\lambda} & Flux_{n\lambda,1} & Uncert_{n\lambda,1} & \ldots & Flux_{n\lambda,nt} & Uncert_{n\lambda,nt} \end{bmatrix}$$

Define energy to wavelength, and wavelength to velocity functions:

$$\lambda e(E) := \frac{h}{\sqrt{2 \cdot mn \cdot E}} \quad v(\lambda) := \frac{h}{mn \cdot \lambda}$$

Set up column matrix of wavelength values:

$$n\lambda := \text{length}\left(data^{<0>}\right) \quad i\lambda := 0 .. n\lambda - 1$$

Define Counters

$$\delta\lambda_{i\lambda} := \left| \lambda e\left(data_{n\lambda + 1 - i\lambda, 0} \cdot Mev\right) - \lambda e\left(data_{n\lambda - i\lambda, 0} \cdot Mev\right) \right|$$

Determine wavelength bin sizes

$$\lambda_{i\lambda} := \lambda e\left(data_{n\lambda + 1 - i\lambda, 0} \cdot Mev\right) + \frac{\delta\lambda_{i\lambda}}{2}$$

Determine Wavelength values

Set up column matrix of time bins

$$nt := \frac{\text{length}\left[\left(data^{T}\right)^{<0>}\right] - 1}{2} \quad it := 0 .. nt - 1$$

Define Counters

$$\delta t_{it} := data_{0, it \cdot 2 + 1} \cdot shake - data_{0, pos(it \cdot 2 - 1)} \cdot shake$$

Determine Time bin sizes

$$t_{it} := \left(data_{0, it \cdot 2 + 1} \cdot shake\right) - \frac{\delta t_{it}}{2}$$

Determine Time values

Look at Ranges

$\lambda min := \min(\lambda)$ $\lambda max := \max(\lambda)$ $tmin := \min(t)$ $tmax := \max(t)$

$\lambda min = 0.042 \cdot A$ $\lambda max = 9.128 \cdot A$ $tmin = 0.05 \cdot \mu sec$ $tmax = 572.7 \cdot \mu sec$

Set up matrices of differential flux and uncertainty values:

Differential Flux: (Also Sets Zero values to small, non-zero value)

$$I0_{i\lambda, it} := \left[\left(data_{n\lambda - i\lambda, it \cdot 2 + 1}\right) \cdot \left| \frac{1}{\delta\lambda_{i\lambda} \cdot \delta t_{it}} \right| + \left(data_{n\lambda - i\lambda, it \cdot 2 + 1} = 0\right) \cdot \frac{10^{-10}}{A \cdot shake}\right] \cdot \frac{1}{cm^{2} \cdot sec}$$

Differential Flux Uncertainty: (Sets zero values to very large value)

$$\sigma I0_{i\lambda, it} := \left[data_{n\lambda - i\lambda, it \cdot 2 + 2} + 10^{10} \cdot \left(data_{n\lambda - i\lambda, it \cdot 2 + 2} = 0\right) \right] \cdot I0_{i\lambda, it}$$

Normalize flux values

$\mathrm{Int} := 3\cdot 10^{7}\cdot \mathrm{cm}^{-2}\cdot \mathrm{sec}^{-1}$ $\lambda\mathrm{int} := 0.5\cdot \mathrm{A}$ Integrated Differential flux > λint for complicated source

$$\mathrm{IntFlux} := \sum_{i\lambda}\sum_{it} I0_{i\lambda,it}\cdot \delta\lambda_{i\lambda}\cdot \delta t_{it}\cdot\left(\lambda_{i\lambda} > \lambda\mathrm{int}\right)$$

Integrated Differential flux > λint for simple evaluation source

$\mathrm{IntFlux} = 1.26\cdot 10^{8}\cdot \mathrm{cm}^{-2}\cdot \mathrm{sec}^{-1}$

$\mathrm{Adjust} := \dfrac{\mathrm{Int}}{\mathrm{IntFlux}}$ $\mathrm{Adjust} = 0.238$ Must multiply flux values obtained from simple source by "Adjust"

Make linear interpolated lookup function:

$it0_{it} := it$

$$\mathrm{lookup}(I,lt,t,tx) := I0^{<\mathrm{floor}(lt)>} + \frac{I0^{<\mathrm{ceil}(lt)>} - I0^{<\mathrm{floor}(lt)>}}{t_{\mathrm{ceil}(lt)} - t_{\mathrm{floor}(lt)}}\cdot\left(tx - t_{\mathrm{floor}(lt)}\right)$$

$$\nu 0(\lambda x,tx,lt) := \mathrm{linterp}\left(\lambda,\mathrm{if}\left(lt = \mathrm{floor}(lt), I0^{<lt>}, \mathrm{lookup}(I0,lt,t,tx)\right),\lambda x\right)\cdot \mathrm{Adjust}$$

$$\nu 1(\lambda x,tx) := \frac{(\lambda x \ge \lambda\mathrm{min})\cdot(\lambda x \le \lambda\mathrm{max})\cdot(tx \ge t\mathrm{min})\cdot(tx \le t\mathrm{max})}{\nu 0(\lambda x,tx,\mathrm{linterp}(t,it0,tx))^{(-1)}}$$

Now account for chopper

$Lp := 70\cdot \mathrm{cm}$ Path length from source to detector (including sample interior):

$Lc := 50\cdot \mathrm{cm}$ Travel Length before chopper

$t0 := 270\cdot \mu\mathrm{sec}$ Time when chopper is at "peak"

$\sigma t := 10^{5}\cdot \mu\mathrm{sec}$ Width of time peak (due to chopper speed)
(Large Values indicate chopper turned off)

Define linear wavelength and time scales

$\lambda 1\mathrm{min} := .1\cdot \mathrm{A}$ $\lambda 1\mathrm{max} := 6\cdot \mathrm{A}$ $n\Lambda := n\lambda\cdot 1$

New Wavelength Scale

$i\Lambda := 0\,..\,n\Lambda - 1$ $\lambda 1_{i\Lambda} := \dfrac{\lambda 1\mathrm{max} - \lambda 1\mathrm{min}}{n\Lambda - 1}\cdot i\Lambda + \lambda 1\mathrm{min}$

$$t1min := \max\left(\left(tmin + \frac{Lp\cdot 1.01}{v(\lambda min)} \quad t0 - 6\cdot \sigma t + \frac{Lp - Lc}{v(\lambda 1min)}\right)\right)$$

$$t1max := \min\left(\left(tmax + \frac{Lp\cdot 0.99}{v(\lambda max)} \quad t0 + 6\cdot \sigma t + \frac{Lp - Lc}{v(\lambda 1max)}\right)\right)$$

New Time Scale

$$nT := 10\cdot nt iT := 0..nT - 1 t1_{iT} := iT\cdot\frac{t1max - t1min}{nT - 1} + t1min$$

Create time-shifted data set, accounting for flight time and chopper

$$iT0_{iT} := iT$$

$$I1_{i\Lambda,iT} := v1\left(\lambda 1_{i\Lambda}, t1_{iT} - \frac{Lp}{v\left(\lambda 1_{i\Lambda}\right)}\right)\cdot \exp\left[-\left(t1_{iT} - \frac{Lp - Lc}{v\left(\lambda 1_{i\Lambda}\right)} - t0\right)^2\cdot\frac{1}{2\cdot\sigma t^2}\right]$$

Make new linear interpolated lookup function:

$$v01(\lambda x, tx, lt) := \mathrm{linterp}\left(\lambda 1, \mathrm{if}\left(lt = \mathrm{floor}(lt), I1^{<lt>}, \mathrm{lookup}(I1, lt, t1, tx)\right), \lambda x\right)$$

$$v2(\lambda x, tx) := \frac{(\lambda x \ge \lambda 1min)\cdot(\lambda x \le \lambda 1max)\cdot(tx \ge t1min)\cdot(tx \le t1max)}{v01(\lambda x, tx, \mathrm{linterp}(t1, iT0, tx))^{(-1)}}$$

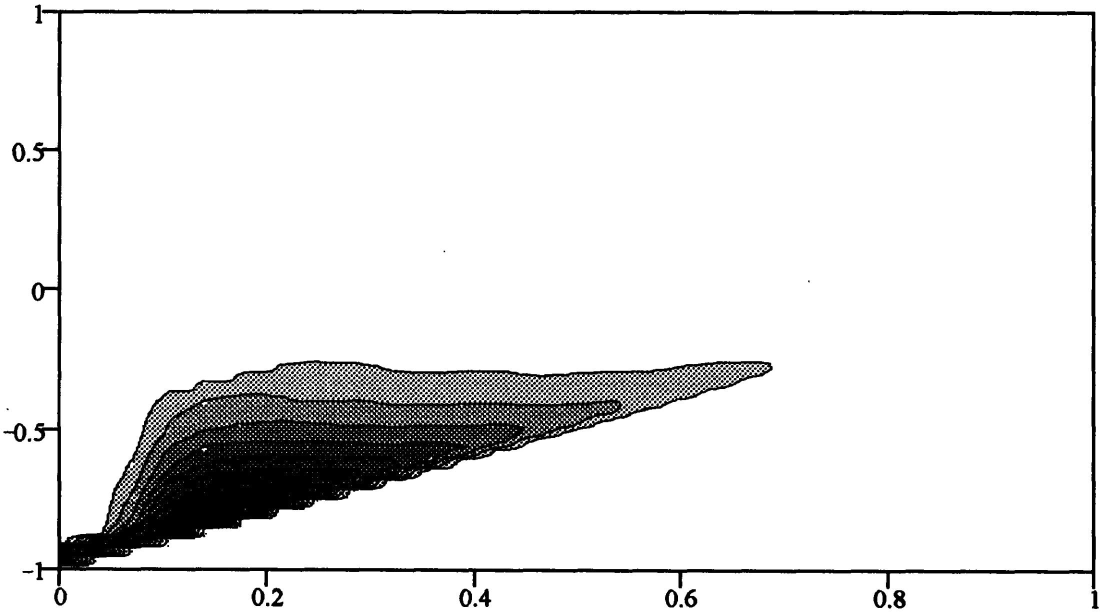

$$\overrightarrow{\left[-\left[I1\cdot\left(cm^2\cdot sec\cdot A\cdot \mu sec\cdot Adjust\right) + 100\right]^{0.25}\right]}$$

Now Determine Wavelength dependent Intensity and Time functions:

$$\Sigma I_{i\Lambda} := \sum_{iT} I1_{i\Lambda,iT} \qquad t00_{i\Lambda} := \frac{\sum_{iT} t1_{iT} \cdot I1_{i\Lambda,iT}}{\Sigma I_{i\Lambda}}$$

Determine time at which intensity reaches maximum for each value of wavelength

$$\sigma t0_{i\Lambda} := \sqrt{\frac{\sum_{iT} \left(t1_{iT} - t00_{i\Lambda}\right)^2 \cdot I1_{i\Lambda,iT}}{\Sigma I_{i\Lambda}}}$$

Determine uncertainty in time for each value of wavelength

$$At0_{i\Lambda} := \Sigma I_{i\Lambda} \cdot \frac{t1max - t1min}{length(t1)} \cdot \frac{1}{\sqrt{2 \cdot \pi} \cdot \sigma t0_{i\Lambda}}$$

Determine Amplitude of distribution for each value of wavelength

Look at data

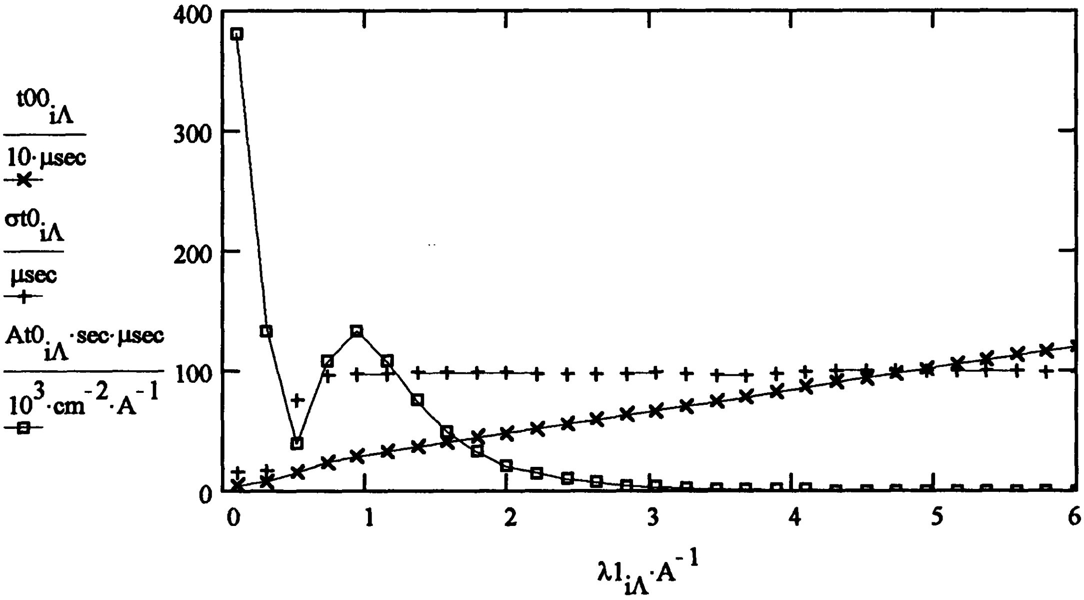

Spline functions:

$vt0 := cspline(\lambda 1, t00)$ $\qquad t0(\lambda) := interp(vt0, \lambda 1, t00, \lambda)$

$v\sigma t := cspline(\lambda 1, \sigma t0)$ $\qquad \sigma t(\lambda) := interp(v\sigma t, \lambda 1, \sigma t0, \lambda)$

$vAt := cspline(\lambda 1, At0)$ $\qquad At(\lambda) := interp(vAt, \lambda 1, At0, \lambda)$

Now, Deal with the sample (BCC Iron)

$pBCC := \begin{pmatrix} 0 & 0.5 \\ 0 & 0.5 \\ 0 & 0.5 \end{pmatrix}$	Location of atoms in BCC matrix
$p := pBCC$	Structure of material under investigation
$d0 := 2.8663 \cdot A$	Cell edge Length
$b := 9.54 \cdot 10^{-15} \cdot m$	Scattering Length
$\sigma i := 0.39 \cdot 10^{-24} \cdot cm^2$	Incoherent Cross Section
$\sigma a := 2.56 \cdot 10^{-24} \cdot cm^2$	Absorption Cross Section
$ma := 55.85 \cdot amu$	Mass of Atom
$\Theta := 411 \cdot K$	Debye Temperature
$T := 293 \cdot K$	Temperature
$tin := 1 \cdot cm$	Thickness of specimen traversed by beam entering sample
$tout := 1 \cdot cm$	Thickness of specimen traversed by beam exiting sample
$Vol := (1 \cdot cm)^3$	Volume of observed region
$n := \mathrm{length}\left[\left(p^T\right)^{<0>}\right]$	# Atoms / unit cell
$Nc := d0^{-3}$	# Cells / unit volume
$\mu := \left(4 \cdot \pi \cdot b^2 + \sigma i + \sigma a\right) \cdot Nc \cdot n$	Linear Absorption Coeff.
$\theta min := \frac{\pi}{8} \quad \theta max := 3 \cdot \frac{\pi}{8}$	Define measurement range
$dmin := \frac{1}{2} \cdot \frac{\lambda 1min}{\sin(\theta max)}$	Define applicable range of d's
$dmax := \frac{1}{2} \cdot \frac{\lambda 1max}{\sin(\theta min)}$	

nr is the ratio of max to min r values under consideration (maximum value=30)

$$nr := \min\left(\left(\mathrm{ceil}\left(\frac{2\cdot d0}{\lambda 1min}\right)\quad 30\right)\right) \qquad ir := 1..nr \qquad jr := 1..nr \qquad maxr := \frac{2\cdot\pi}{d0}\cdot nr$$

$$Nr := \sum_{ir}\left[\sum_{jr}(jr+1)\cdot(jr \le ir) + 1\right]$$

Nr is the number of plane families that could exist between the min and max r values

Calculate all variations of HKL

$$hh_0 := 1 \qquad kk_0 := 0 \qquad ll_0 := 0 \qquad ii := 1..Nr \qquad jj := 0..Nr$$

$$\begin{bmatrix} hh_{ii} \\ kk_{ii} \\ ll_{ii} \end{bmatrix} := \begin{bmatrix} hh_{ii-1} + \left(hh_{ii-1} = ll_{ii-1}\right) \\ \left[kk_{ii-1} + \left(kk_{ii-1} = ll_{ii-1}\right)\right]\cdot\left(hh_{ii-1} \ne ll_{ii-1}\right) \\ \left[ll_{ii-1} + \left(kk_{ii-1} \ne ll_{ii-1}\right)\right]\cdot\left(kk_{ii-1} \ne ll_{ii-1}\right) \end{bmatrix}$$

$$hkl := \mathrm{augment}(hh, \mathrm{augment}(kk, ll))^T$$

$$m0 := \overrightarrow{\frac{48}{\left[2^{((hh=kk)+(kk=ll)+(kk=0)+(ll=0))} + 2\cdot(hh=ll)\right]}}$$

Calculate multiplicity of planes

$$r_{jj} := \frac{\sqrt{\left(hh_{jj}\right)^2 + \left(kk_{jj}\right)^2 + \left(ll_{jj}\right)^2}}{d0} \qquad d0 := \overrightarrow{\frac{1}{r}}$$

Calculate reciprocal and real lattice spacings

$$W_{jj} := \frac{6\cdot h^2}{\Theta^2\cdot k\cdot ma}\cdot\frac{T}{4\cdot\left(d0_{jj}\right)^2}\cdot\left(1 + \frac{\Theta^2}{36\cdot T^2} - \frac{\Theta^4}{3600\cdot T^4}\right)$$

Determine Debrye-Waller factor

$$i := 0..n-1$$

$$F0_{jj} := \left|\sum_{i} b\cdot\exp\left(2\cdot i\cdot\pi\cdot hkl^{\langle jj\rangle}\cdot p^{\langle i\rangle}\right)\right|\cdot\exp\left(-W_{jj}\right)$$

Determine Structure factor for each reflection

To save time, the planes are sorted, so that only those which are expected to diffract with a large intensity are evaluated further:

$\mathrm{int}_{jj} := \mathrm{m0}_{jj}\cdot\left(\mathrm{F0}_{jj}\right)^{2}\cdot\left(\mathrm{d0}_{jj}\right)^{3}$ Make intensity estimate

Make matrix, for sorting:

$\mathrm{sortmat} := \mathrm{augment}\left(\mathrm{augment}\left(\mathrm{int}\cdot A^{-4}, \mathrm{m0}\cdot A\right), \mathrm{augment}(\mathrm{F0}, \mathrm{d0})\right)$

$\mathrm{sortout} := \mathrm{csort}(\mathrm{sortmat}, 0)$ Do the sort

$\mathrm{nhkl} := 20 \quad kk := 0..\mathrm{nhkl} - 1$ Setup new counter

$m_{kk} := \mathrm{sortout}_{Nr - kk, 1}\cdot A^{-1}$

$F_{kk} := \mathrm{sortout}_{Nr - kk, 2} \quad d_{kk} := \mathrm{sortout}_{Nr - kk, 3}$

Retrieve values of sorted variables

Now, specify some constants relevant to Difrraction and Detection:

$n\theta := 128 \quad d\theta := \dfrac{\theta max - \theta min}{n\theta}$ Define set of Angle Values

$i\theta := 0..n\theta - \theta_{i\theta} := \theta min + d\theta\cdot\left(i\theta + \dfrac{1}{2}\right)$

$\lambda 2_{i\theta, kk} := 2\cdot d_{kk}\cdot\sin\left(\theta_{i\theta}\right)$ Define set of Wavelength Values

$\phi 1 := -\dfrac{\pi}{2} \quad \phi 2 := \dfrac{\pi}{2}$ Define range of Azmuthal Angle Values

$l0 := 50\cdot cm \quad ww := 7\cdot cm$ Length of primary collimator, widest width of collimator

$ws := 1\cdot cm \quad ds := 10\cdot cm$ Sample width, distance from end of collimation to sample location

$\alpha 0 := \dfrac{ww}{l0 + ds} \quad \beta 0 := \alpha 0$ Primary collimation

$\eta d := 5\cdot\%$	Efficiency of detector
$twall := 0.01\cdot cm$	Thickness of collimator walls
$r2 := 10\cdot cm \; l2 := .6\cdot cm$	Radial and side length of detector collimators
$r2\cdot d\theta = 0.614\cdot mm$	Width of Detector Collimators
$\eta c := \frac{r2\cdot d\theta - twall}{r2\cdot d\theta}$	Fraction accounts for decrease in intensity due to collimator wall thickness
$\alpha 2 := d\theta\cdot\frac{r2}{l2}\cdot\frac{0.87\cdot\sqrt{2\cdot\pi}}{\sin\left(\frac{\pi}{2}\cdot\frac{l2}{r2}\right) + 2}$	Detector Collimation
$\frac{\alpha 2\cdot r2}{ws} = 1.065$	This value should be about 1 ... May need to adjust value of l2
$\sigma\theta := \frac{1}{2}\cdot\sqrt{\alpha 0^2 + \alpha 2^2}$	Uncertainty in angle
$\sigma\lambda(\theta,\lambda) := \sqrt{\lambda^2\cdot\cot(\theta)^2\cdot\sigma\theta^2 + \sigma t(\lambda)^2\cdot\frac{h^2}{mn^2\cdot Lp^2}}$	Uncertainty in wavelength

Next Two Functions calculate intensity diffracted and measured for each family of planes and for each detector

$$Atsig(\theta,\lambda) := (\lambda 1min<\lambda)\cdot(\lambda<\lambda 1max)\cdot 2\cdot\pi\cdot At(\lambda)\cdot\sigma t(\lambda)\cdot\sigma\lambda(\theta,\lambda)\cdot\frac{\lambda^3}{4\cdot\sin(\theta)}\cdot\eta c\cdot\eta d$$

$$I2_{i\theta,kk} := Atsig\left(\theta_{i\theta},\lambda 2_{i\theta,kk}\right)\cdot\left(F_{kk}\right)^2\cdot m_{kk}\cdot Nc^2\cdot Vol\cdot\frac{\alpha 0\cdot\beta 0}{2\cdot\pi}\cdot\frac{\phi 2 - \phi 1}{2\cdot\pi}\cdot\exp(-\mu\cdot(tin + tout))$$

Calculate background due to incoherent scattering.

$$Inc_{i\theta,kk} := \frac{At\left(\lambda 2_{i\theta,kk}\right)\cdot\sigma t\left(\lambda 2_{i\theta,kk}\right)\cdot\sigma\lambda\left(\theta_{i\theta},\lambda 2_{i\theta,kk}\right)\cdot\frac{\alpha 0\cdot\beta 0}{2\cdot\pi}\cdot(Vol\cdot Nc\cdot n\cdot\sigma i)\cdot\frac{\phi 2 - \phi 1}{2\cdot\pi}}{\exp(\mu\cdot(tin + tout))\cdot(\eta c\cdot\eta d)^{-1}}$$

Now, the strain determination process is modeled:

These equations represent equation 2.??, Integrated over the range of phi.

$$a1(\theta) := \frac{\pi}{8}\cdot\sin(\theta\cdot 2)^4$$

$$a2(\theta) := \frac{\pi}{2}\cdot\sin(2\cdot\theta)^2\cdot(\cos(\theta\cdot 2) - 1)^2$$

$$a3(\theta) := \pi\cdot(\cos(\theta\cdot 2) - 1)^4$$

$$a4(\theta) := \frac{2}{3}\cdot\sin(2\cdot\theta)^3\cdot(\cos(\theta\cdot 2) - 1)$$

$$a5(\theta) := 2\cdot(\cos(\theta\cdot 2) - 1)^3\cdot\sin(\theta\cdot 2)$$

$$aa(\theta) := \begin{bmatrix} 3\cdot a1(\theta) & a1(\theta) & a2(\theta) & 0 & 0 & 2\cdot a4(\theta) \\ a1(\theta) & 3\cdot a1(\theta) & a2(\theta) & 0 & 0 & a4(\theta) \\ a2(\theta) & a2(\theta) & a3(\theta) & 0 & 0 & a5(\theta) \\ 0 & 0 & 0 & a1(\theta) & a4(\theta) & 0 \\ 0 & 0 & 0 & a4(\theta) & a2(\theta) & 0 \\ 2\cdot a4(\theta) & a4(\theta) & a5(\theta) & 0 & 0 & a2(\theta) \end{bmatrix}$$

Calculate σ, rms uncertainty per unit time$^{1/2}$

$$LL(\theta,\lambda,I,Inc) := \frac{32\cdot\left(\sin(2\cdot\theta)^2\cdot\sigma\theta^2\right) + 64\cdot\sin(\theta)^4\cdot\left[\frac{h}{(Lc + Lp)\cdot mn}\right]^2\cdot\frac{\sigma t(\lambda)^2}{\lambda^2}}{(I + Inc\cdot 7.5)^{-1}\cdot I^2}$$

$$\sigma := \sqrt{\frac{1}{6}\cdot tr\left[\left[\sum_{kk}\sum_{i\theta}\left(I2_{i\theta,kk}\cdot sec>0\right)\cdot\frac{aa\left(\theta_{i\theta}\right)}{LL\left(asin\left(\frac{\lambda 2_{i\theta,kk}}{2\cdot d_{kk}}\right),\lambda 2_{i\theta,kk},I2_{i\theta,kk},Inc_{i\theta,kk}\right)}\right]^{-1}\right]}$$

Calculate time to resolve 10% of yield strain: $\left(\frac{\sigma}{0.02\cdot\%}\right)^2 = 8\cdot hour$

Time assuming source at 100 x the intensity: $\left(\frac{\sigma}{0.02\cdot\%}\right)^2\cdot 0.01 = 4.6\cdot min$

Bibliography

[1] Mikhail Grigorevich Kaganer, *Thermal insulation in cryogenic engineering,* Israel Program for Scientific Translations, Jerusalem (1969).

[2] S.M.A. Islam, M.N. Akramuzzaman, M.A. Awal, and M.N. Islam, "A study of Neutron Shielding Properties of Some Multilayers Containing Polyethelene," *Applied Radiation and Isotopes*, **44**, 8 (1993).

[3] K. Ueki, Y. Namito, "Optimum Arrangement for the Neutron Dose-Rate of an Iron-Polyethelene Shielding System," *Nuclear Science and Engineering*, **96**, 1 (1987).

[4] S.I. Bhuiyan, F.U. Ahmed, A.S. Mollah, and M.A. Rahman, "Studies of the Neutron-Transport and Shielding Properties of Locally Developed Shielding Material - Poly-Boron," /it Health Physics **57** 5 (1989).

[5] Samuel Wilensky, *Fast neutron shielding studies*, Cambridge, M.I.T. Dept. of Nuclear Engineering, (1969)

[6] Samuel M. Selby, editor, *CRC Standard Mathematical Tables*, CRC Press, Cleveland, Ohio.

[7] Werner Schmatz, "Defects in Solids," *Methods of Experimental Physics*, **23** part A, 85 (1986).

[8] John R. Wolberg, *Prediction Analysis*, Van Nostrand, Princeton, NJ, (1967).

[9] B. Buras, "Note on the Integrated Intensity in the Time-if Flight Method for Crystal Structure Investigations," *Nukleonika*, **VIII**, 4 (1963).

[10] A. Taylor and Brenda J. Kegle, *Crystallographic Data on Metal and Alloy Structures*, Dover Publishing Incorporated, New York, (1963)

[11] Max Born, *Dynamical Theory of Crystal Lattices*, Clarendon Press, Oxford (1954).

[12] *International Tables for X-ray Crystallography*, **3**: Physical and Chemical Tables, D. Reidel Publishing Company, Boston (1985)

[13] Varley F. Sears, "Appendix. Neutron Scattering Lengths and Cross Sections," *Methods of Experimental Physics*, **23** part A, 521 (1986).

[14] Peter L. Hagelstein, "Coherent and Semicoherent Neutron Transfer Reactions I: The Interaction Hamiltonian," *Fusion Technology*, **22**, 172 (1992).

[15] David Mildner, Heather Chen, and Greg Downing, "Focused Neutrons: A Point to be Made," *Journal of Neutron Research*, **1**, 1 (1993)

[16] T. Lorentzen, "Residual Stress Measurements at Risø," *Journal of Neutron Research*, **1**, 13 (1993).

[17] Giordano Diambrini Palazzi, "High-Energy Bremddtrahlung and Electron Pair Production in Thin Crystals," *Reviews of Modern Physics*, **40**, 611 (1968).

[18] R. H. Siemssen, M Cosak, and R. Felst, "Reaction Mechanism Study of lp=1 Stripping Process on Nuclei of the 1p shell," *Nuclear Physics*, **69**, 209 (1965).

[19] Stephen W. Lovesley, *Theory of Neutron Scattering from Condensed Matter, Volume 1*, Clarendon Press, Oxford (1984).

[20] G.E. Bacon, *Fifty Years of Neutron Diffraction*, Adam Hilger, Bristol (1987).

[21] G.E. Bacon, *Neutron Diffraction*, Clarendon Press, Oxford (1962).

[22] H. Dachs, *Topics in Current Physics, Volume 6: Neutron Diffraction*, Soringer-Verlag, Berlin (1978).

[23] Y.C. Yanch and X-L. Zhou, "Accelerator-based Epithermal Neutron Beam Design for Neutron Capture Therapy," *Medical Physics*, **19**, 709 (1992).

[24] K.F. Bradley, S.-H. Chen, and P. Thiyagarajan, "Micellar Formation and Correlation in the Cavity of Porous Silica Glass," *Physical Review A*, **42**, 6015 (1990).

[25] J. Wayne Rabalais, "Scattering and Recoiling Spectrometry: An Ion's Eye View of Surface Structure," *Science*, **220**, 521 (1990).

[26] E.N. Bakshi, "Time-Correlated Diffraction," *Meas. Sci. Technology*, **1**, 1123 (1990).

[27] G.B. Mitra and Lily Chakravartti, "A method of Seperation of Double Bragg Scattering from Small-Angle Scattering of X-rays by Metals and Alloys," *Journal of Physics D: Applied Physics*, **25**, 967 (1992).

[28] A.D. Krawitz, P.J. Rudnick, B.D. Butler, and J.B. Cohen, "Neutron Measurements with a Position Sensitive Detector," *Advances in X-Ray Analysis, Volume 29*, Plenum Press, New York (1986).

[29] I.C. Noyan and J.B. Cohen, "Residual Stresses in Materials," *American Scientist*, **79**, 142 (1991).

[30] G. Harding and J. Kosanetzky, "Scattered X-ray Beam Nondestructive Testing," *Nuclear Instruments and Methods in Physics Research*, **A280**, 517 (1989).

[31] Michael T. Hutchings, "Neutron Diffraction Measurements of Residual Stress Fields - the Engineer's Dream Come True?" *Neutron News*, **3**, 14 (1992).

[32] C.C. Wilson and T. Zaleski, "The Performance amd Future Prospects of the Anger Camera PSD for Single Crystal Diffraction at ISIS," *Physica B*, **180** and **181**, 993 (1992).

[33] N. Niimura, K. Aizawa, M. Hirai, and U. Sangawa, "Small-Angle Thermal Neutron Scattering Spectrometer (WIT)," *Physica B*, **180** and **181**, 941 (1992).

[34] E. S. Jansen, W. Schafer, A. Szepesvary, G. Will, R. Reinartz, K.D. Muller, H. Tietze, and U. Steigenberger, "Position-Sensitive Scintillation Detector JULIOS Under Experimental Conditions at ISIS," *Physica B*, **180** and **181**, 917 (1992).

[35] *Energy levels of Light Nucleii* $A = 5 - 10\%$

[36] J.R.D Copley, "A New Time of Flight Spectrometer at NIST," *Physica B*, **180** and **181**, (1992).

[37] P.J. Webster, "Neutron Strain Scanning," *Neutron News*, **2**, 19 (1991)

[38] D.S. Kupperman, S. Majumdar, and J.P. Singh, "Residual Strain in Advanced Composites," *Neutron News*, **3**, 15 (1991).

[39] M. Aslam Lone, "Nuclear Data Needed for Industrial Neutron Sources," *Nuclear Data for Science and Technology*, Springer-Verlag, Berlin, 678 (1991).

[40] John M. Carpenter and William B. Yelon, "Neutron Sources," *Methods of Experimental Physics*, **23** part A, 99 (1986).

[41] Colin G. Windsor, "Experimental Techniqies," *Methods of Experimental Physics*, **23** part A, 197 (1986).

[42] Robert W. Hamm, *A compact Accelerator-Based Neutron Source for Baggage Interrogation*, AccSys Technology, Inc, (1990).

[43] D.A. Garrett, H. Berger, "The Technological Development of Neutron Radiography," *Atomic Energy Review*, **15**, 125 (1977).

[44] A.A. Harms, " Physical Processes and Mathematical Methods in Neutron Radiography," *Atomic Energy Review*, **15** 2, 143 (1977).

[45] M.C. Karadeniz, "Low-Lying Energy Levels of B-10," *Journal of Physics A*, **7**, 2284 (1974).

[46] J.S. Pruitt, C.D. Swartz, and S.S. Hanna, "Energies and Angular Distributions form Be-9(d,n)B-10," *Physical Review*, **92**, 1456 (1953).

[47] T.W. Bonner and C.F. Cook, "Excited States in B-10 and Be-8," *Physical Review*, **96**, 122 (1954).

[48] M.R. Hawkesworth, "Neutron Radiography Equipment and Methods," *Atomic Energy Review*, **15**, 169 (1977).

[49] M.R. Hawkesworth and Colin G. Windsor, "Industrial Applications," *Methods of Experimental Physics*, **23** part C, chapter 25 (1986)